MAGNETIC FILTRATION OF IRON PRECIPITATES

by

© Iain A. Todd

A Thesis Submitted to the
Faculty of Graduate Studies and Research
in Partial Fulfillment of the Requirements for the Degree of
Doctor of Philosophy

Department of Mining and Metallurgical Engineering
McGill University
Montreal, Canada

December 1982

ABSTRACT

A variety of iron precipitates formed in the electrolytic zinc industry were studied to estimate the possibility of magnetic filtration to augment conventional thickening/filtering systems. The precipitates included K,NH_4,Na jarosites, α and β goethite, α hematite and an industrially produced NH_4 jarosite. The wet Frantz Isodynamic Separator was used to generate magnetic susceptibility data. Susceptibilities ranged from $\kappa = 6.9 \times 10^{-5} \rightarrow 15.5 \times 10^{-5}$ emu/cm^{3}Oe. Particle size of the precipitates ranged from 25μm to < 1μm. Magnetic filtration breakthrough curves were produced using a high gradient magnetic filtration technique. The role of fluid viscosity and velocity as well as magnetic field was studied.

All the precipitates proved filterable. A comparison was made of a physical and an empirical model of the breakthrough curves in the sizing of the magnetic filters required to treat thickener overflow at the CEZ Valleyfield plant.

For a volumetric flow of 100m^3/hr electrolyte, containing 15g/L NH_4 jarosite, 2 magnets of 2.6m diameter and 0.35m bed depth are required to lower solids contents to the present operating level of 3g/L.

RESUME

Nous avons étudié plusieurs précipités ferreux qu'on retrouve dans le traitement électrolytique du zinc, afin d'évaluer la possibilité d'augmenter la capacité des systèmes épaississage/filtration conveutionels par filtration magnétique. Parmi les précipités, citons des jarosites de K, NH_4 et Na, de la goethite α et β, de l'hématite α et une jarosite de NH_4 produite industriellement. Des données de susceptibilité magnétique furent obtenues à l'aide d'un séparateur humide isodynamique Frantz, les susceptibilités variant de $\kappa = 6.9 \times 10^{-5}$ à 15.5×10^{-5} emu/cm^3Oe et le diamètre des particules précipitées de 25μm jusqu'à moins de 1μm.

Nous avons, en utilisant une technique de filtration magnétique à haut gradient, obtenu des courbes de charge de la matrice. Le rôle de la viscosité et vélocité du fluide fut aussi étudié. Tous les précipités purent être filtrés.

Nous avons utilisé deux modèles, l'un physique, l'autre empirique, pour dimensionner les filtres magnétiques qui traiteraient la surverse des épaississeurs à l'usine CEZ de Valleyfield. Le modèle empirique prédit que pour un débit de 180m^3/h d'électrolyte, contenant 15g/L de jarosite

de NH_4, 2 aimants de 2.6m de diamètre et de 0.35m d'épaisseur pourront reduire la concentration de solides jusqu' à 3g/L, le niveau actuel.

ACKNOWLEDGEMENTS

The author wishes to express his sincerest gratitude and appreciation to Prof. J.A. Finch for his encouragement, patience and support throughout the course of this research.

Thanks are also due to the staff, fellow students and technicians of the Department of Metallurgical Engineering for their help on numerous occasions.

The author also wishes to acknowledge the assistance of Michel Leroux (McGill) in conducting filtration experiments, Dr. B. Muir (Physics, McGill) in obtaining magnetometer data, Dr. M. Mackinnon (Geology, McGill) for help in microprobe studies and Dr. N. Rowlands (McGill) for help in the electron micrograph examinations.

Finally the loan of a Sala 10-15-20 laboratory magnet from CANMET (Ottawa) and the financial assistance of the Graduate Faculty of McGill is especially acknowledged.

TABLE OF CONTENTS

Page

ABSTRACT i

RESUME ii

ACKNOWLEDGEMENTS iv

TABLE OF CONTENTS v

NOMENCLATURE ix

LIST OF FIGURES xii

LIST OF TABLES xviii

I. INTRODUCTION 1

1.1 Concepts and Examples of Magnetic Filtration 1

1.2 Removal of Iron from Solution 6

1.3 Removal of Iron in the Electrolytic Zinc Industry 9

1.4 Prospects for Magnetic Filtration of Iron Precipitates in the Zinc Industry 20

II. PRECIPITATION OF IRON IN THE ZINC INDUSTRY 22

2.1 General 22

2.2 Ferric Hydroxide 22

2.3 Jarosite 34

2.4 Goethite 41

2.5 Hematite 46

2.6 Magnetite 50

III. MAGNETS AND MAGNETIC CAPTURE MODELS 55

3.1 Magnets 55

Page

3.2 Models 60

  3.2.1 Introduction 60
  3.2.2 Trajectory Models 63
  3.2.3 Build-Up Models 68
  3.2.4 Filtration Breakthrough Models 78

IV. EXPERIMENTAL PROCEDURES 91

4.1 Solids Preparation 91

  4.1.1 Jarosites 91
  4.1.2 Goethites 92
  4.1.3 Hematite 94
  4.1.4 Magnetite 94
  4.1.5 Ferric Hydroxide 95
  4.1.6 CEZ Jarosite 95

4.2 Precipitate and Fluid Analysis 96

  4.2.1 Jarosites 96
  4.2.2 Goethites 97
  4.2.3 Hematite and Magnetite 98

4.3 Parameter Measurement 98

  4.3.1 Particle Density 98
  4.3.2 Precipitate Particle Size 98
  4.3.3 Particle Magnetisation Measurement 99
    4.3.3.1 Theory 99
    4.3.3.2 Measurement of Susceptibility 102
    4.3.3.2 (a) The Frantz Instrument 102
    4.3.3.2 (b) Technique 112
    4.3.3.2 (c) Foner Vibrating Magnetmeter 112
  4.3.4 Wire Magnetisation 113
    4.3.4.1 Theory 113
    4.3.4.2 Procedure 115
  4.3.5 Viscosity Measurements 115

4.4 Magnetic Filtrations 116

4.5 Experimental Design 121

Page

V. RESULTS 123

5.1 Precipitate Analysis 123

- 5.1.1 X-Ray Diffraction 123
- 5.1.2 Differential Thermal Analysis 123
- 5.1.3 Chemical Analysis 130
- 5.1.4 Microprobe Analysis 132

5.2 Electrolyte Analysis 134

5.3 Parameter Measurement 134

- 5.3.1 Particle Density 134
- 5.3.2 Particle Size 134
- 5.3.3 Particle Magnetisation 151
  - 5.3.3.1 Wet Frantz Measurements 151
  - 5.3.3.2 Magnetometer Measurements 151
- 5.3.4 Wire Magnetisation 153
- 5.3.5 Electrolyte Viscosity and Density Measurements 153

5.4 Filtration Experiments 158

5.5 Magnet Sizing 180

- 5.5.1 The Collan Model 180
- 5.5.2 The Nesset Model 190

VI. DISCUSSION 197

6.1 Precipitate Analysis 197

6.2 Particle Magnetisation 198

6.3 Particle Size Analysis 201

6.4 Filtration 202

- 6.4.1 General Comments 202
- 6.4.2 Filter Performance of Precipitates 204
- 6.4.3 Using the Nesset and Collan Models in Magnet Sizing 208

6.5 Metallurgical Applicability ~~213~~ 212

Page
VII. CONCLUSIONS AND FUTURE WORK 217
  7.1 Conclusions 217
  7.2 Claims for Original Research 219
  7.3 Future Work 220
BIBLIOGRAPHY 221
APPENDIX I. S.I. UNIT CONVERSION 229
APPENDIX II. PROCEDURE FOR COLLAN DATA FITTING 232
APPENDIX III. WET FRANTZ MEASUREMENTS 234
APPENDIX IV. EXPERIMENTAL FILTRATION DATA 238
APPENDIX V. FILTRATION REGRESSION ANALYSIS 251

NOMENCLATURE

a	bare wire radius
A	matrix cross sectional area (Akoto)
A	field perturbation term = $2\pi M_w/H_a$
A(F)	free cross-sectional area of matrix
b	particle radius
B	Blasius solution of θ terms
c	concentration of particles
C^*	constant in simplified force balance
C_{abs}	mass concentration of absorbed particles
C_{in}	mass concentration of particles entering filter
C_{out}	mass concentration of particles in effluent
C_s	saturation concentration of absorbed particles
F	mass flow rate of solids
F	volumetric packing fraction
F_0	matrix loading coefficient
F_c	competing forces
F_g	gravitational force
F_r	net radial forces
F_x	magnetic force in x direction
F_θ	net tangential forces
F_m	magnetic force
$F(V_m)$	function describing the cumalative weight fraction of particles with magnetic velocity $< V_m$
f_{max}	maximum build-up to volume ratio
f_b	fractional area of particle shear
f	capture efficiency
g	gravitional constant
H	magnetic field. Oe
H_D	demagnetising field = NM_w
H_a	applied field
I_{50}	current at which 50% of feed to Frantz Isodynamic reports the magnetics chute, amperes
k	kinetic energy coefficient in viscosity measurement
K	" " " " " " " " " "
K	empirical constant in wire magnetisation
K	matrix length/clean matrix absorption length in Collan model
K_d	deposition coefficient
K_f	universal fibre parameter
L	matrix length
ℓ	matrix absorption length
ℓ_0	clean matrix absorption length

m	particle mass g
m	empirical constant in viscosity determination
M_p	particle magnetisation, emu/cm^3
M_s	wire saturation magnetisation, emu/cm^3
M_0	spontaneous magnetisation
M_w	wire magnetisation, emu/cm^3
N	demagnetisation factor
N_0	number of particles leaving separator
N_i	number of particles entering separator
N_L	dimensionless ratio of magnetic to fluid shear forces
n	mass of particles deposited per unit mass of packing
n_T	matrix loading of captured particles per fibre
Q	volumetric flow rate through matrix
r_a	relative particle accumalation radius
R_c	capture radius of wire +a
Re_w	wire Reynolds number
T	throughout parameter in Akoto model
t	real time
t_e	effective filtration time
t_f	total filtration time
t_0	efficient filtration time
t_w	flushing time
U_∞	free stream velocity
v	particle volume
v_w	wire volume
v_0	superficial velocity
V	build-up volume
V_m	magnetic velocity = $4b^2\kappa H_a^2A/9a\eta$
V_L	fluid velocity in wet Frantz
V_a	particle velocity due to gravity in wet Frantz
V_{nm}	velocity of non-magnetic particle
v_s	V_0C_{in}/C_s
y	data filled constant in Collan analysis of filtration
x	distance from filter inlet
α	particle absorption probability
δ	nominal boundary layer thickness
γ_m	mass loading g particles/g wire
γ_v	volume loading cm^3 particles/cm^3 wire
ξ	capture radius for mechanical entrapment
ε	packing fraction in Nesset model
ε	void fraction in Akoto model
ε_0	inter void fraction in Akoto model
λ_0	clean fibre cross-sectional area
η	fluid viscosity (absolute) g/cm-s
Θ	angle from front stagnation point (Nesset model)
κ	particle volume susceptibility, emu/cm^3-0e

κ_p	particle κ emu/cm^3 Oe
κ_m	medium κ emu/cm^3 Oe
κ_∞	susceptibility extrapolated to infinite field strength,
	field dependent susceptibility
ν	fluid viscosity, (Kinematic) cm^2/s
ρ_m	density of matrix packing (Akoto)
ρ_f	fluid density
ρ_p	particle density
ρ_w	wire density
σ_0	spontaneous magnetisation emu/g
τ	filter time
T	elapsed time
χ	mass susceptibility emu/g
Ψ	effluent concentration ratio

LIST OF FIGURES

Figure		Page
1-1	Flow sheet of basic Jarosite Process.	12
1-2	Flow sheet of the E. Z. Process.	14
1-3	Flow sheet of basic Hematite Process.	16
2-1	Eh-ph diagram for the iron-water system at 25° and at atmospheric pressure.	24
2-2	Fe_2O_3-SO_3-H_2O Equilibrium diagrams at 75°C.	26
2-3	Solution species present the Fe^{3+}-H_2O system at 25°C as a function of iron concentration and pH.	27
2-4	Solubility of iron(III)hydroxide and oxides at 25°C.	28
2-5	Predominance-volume diagram for the iron (III)-sulphate water system at 25°C.	30
2-6	Predominance-volume diagram for the iron (III)-sulphate water system at 140°C.	31
2-7	Growth of polymer forms by hydroxyl bridging.	33
2-8	Fe_2O_3-SO_3-H_2O Equilibrium diagrams at 110°C.	36
2-9	Jarosite-stable region in potential-pH diagram of Fe-SO_4-H_2O system at 95°C, $[K] = 10^{-2}M$, $[H_2SO_4{}^{2} + SO_4{}^{2-}] = 1M$.	37
2-10	Structure of alumite $KAl_3(SO_4)_2(OH)_6$.	40
2-11	Portion of the Fe_2O_3-H_2O-SO_3 phase system at 100°C.	43

Figure		Page
2-12	Fe_2O_3-SO_3-H_2O equilibrium diagram at 200 C. Dashed lines indicate effect of 75g/L Zn addition.	48
2-13	Behaviour of (a) magnetic properties, (b) pH and (c) iron, during precipitation of Fe_3O_4 from $FeSO_4$ solution by neutralization and oxidation treatment. Conditions: 100°C, NH_3/S molar ratio 2.2, 0.17MPa O_2.	54
3-1	Iron clad solenoid design of hgms device.	56
3-2	Schematic diagram of cyclic hgms.	57
3-3	Schematic diagram of carousel hgms.	59
3-4	Simplified situation of spherical, paramagnetic particle approaching a cyclindrical, ferromagnetic wire in hgms.	61
3-5	Magnetic force contours for an infinite ferromagnetic cylinder in a uniform field.	62
3-6	Watson's dependence of R_c on V_m/U_∞.	65
3-7	Liu et al maximum relative build up volume (f max) as a function of V_m/U_∞.	72
3-8	Force component acting on a spherical particle at rest on a cylinder wall.	74
3-9	Loci of net radial and tangertial forces in one quadrant about a wire. Hatched areas show negative net force.	75
3-10	Akoto's hypothetical filter model.	80
3-11	Akoto's sample of breakthrough curve.	83
3-12	Diagram of filter parameters for Collan model.	84
3-13	Sample of inversion of breakthrough curve from Collan et al.(21)	86

Figure		Page
3-14	Collan approach to magnet sizing for waste water filtration system (x) y=z (o) y=1.	89
4-1	Magnetisation behaviour as a function of field for (a) diamagnetics, (b) paramagnetics or antiferromagnetics, (c) ferromagnetics or ferrimagnetics.	102
4-2	The dry Frantz force balance on a particle travelling between the isodynamic pole pieces.	104
4-3	The magnetic profile of a paramagnetic material as deduced from Frantz data.	106
4-4	The "wet Frantz" system.	108
4-5	Vector diagram for particles in the chute of the wet Frantz separator.	111
4-6	Fluid and Magnet systems for filtration tests.	118
4-7	The matrix cannister design for filtration tests.	119
5-1	Differential Thermal Analysis for the VM procedure. α-FeOOH identified	127
5-2	Differential Thermal Analysis for the EZ procedure. $\alpha+\beta$ FeOOH identified	128
5-3	Differential Thermal Analysis for the EZ procedure at an increased precipitation rate (1.5x). β-FeOOH identified	129
5-4	Photograph of "mags" product form Davis tube separation of CEZ jarosite precipitation tank sample.	133
5-5	Sedigraph analysis of synthetic K,NH_4Na jarosite and CEZ jarosite precipitates.	137
5-6	Sedigraph analysis of synthetic α and β FeOOH precipitates.	138
5-7	Sedigraph analysis of synthetic α-Fe_2O_3 precipitate.	139

Figure		Page
5-8	Micrograph of CEZ jarosite, x 10,000.	141
5-9	Micrograph of CEZ jarosite, x 50,000.	142
5-10	Micrograph of synthetic NH_4jarosite, x 6,000.	143
5-11	Micrograph of synthetic NH_4 jarosite, x 20,000.	144
5-12	Micrograph of synthetic K jarosite, x 1,000.	145
5-13	Micrograph of synthetic Na jarosite, x 6,000.	146
5-14	Micrograph of synthetic Na jarosite, x 4,000.	147
5-15	Micrograph of synthetic α-FeOOH, x 2,000.	148
5-16	Micrograph of synthetic α-FeOOH, x 20,000.	149
5-17	Micrograph of synthetic α-Fe_2O_3, x 10,000.	150
5-18	Wire magnetisation curves for stainless steel wool of diameter 60μm.	155
5-19	Breakthrough curves for synthetic K jarosite, runs (3) H_a=4.2kOe, U_∞=2.3cm/s. (4) H_a=4.2kOe, U_∞=1.2cm/s.	161
5-20	Breakthrough curves for synthetic K jarosite, runs (5) H_a=4.2kOe, U_∞=o.9cm/s. (6) H_a=9.1kOe, U_∞=0.9cm/s. (7) H_a=9.1kOe, U_∞=2.3cm/s.	162
5-21	Breakthrough curves for synthetic Na jarosite, runs (8),(9) H_a=4.2kOe, U_∞=0.9cm/s., (10) H_a=9.1kOe, U_∞=2.3cm/s.	164
5-22	Breakthrough curve comparison of run 9 with the delayed magnet energizing of run 30. H_a=4.2kOe, U_∞0.9cm/s.	165
5-23	Photograph of samples of effluent with time of run 30.	166
5-24	Breakthrough curves for synthetic NH_4 jarosite runs (11) H_a=9.1kOe, U_∞=0.9cm/s, (12)(13) H_a=4.2kOe, U_∞=0.9cm/s.	168

Figure **Page**

5-25 Breakthrough curves for synthetic α-FeOOH runs 14,15,16 and α-Fe_2O_3, run 17. (14),(15) H_a=4.2kOe, U_∞=0.9cm/s. (16) H_a=9.1kOe, U_∞=2.3cm/s. (17) H_a=9.1kOe, U_∞=0.9cm/s. 169

5-26 Breakthrough curve for "clean" CEZ jarosite, run 20. H_a=9.1kOe, U_∞=0.9cm/s. 171

5-27 Breakthrough curve for hydrated ferric oxide, run 21. H_a=21.0kOe, U_∞=0.9cm/s. 172

5-28 Breakthrough curve for synthetic NH_4 jarosite, electrolyte as fluid carrier, run 22. H_a=9.1kOe, U_∞=0.9cm/s. 174

5-29 Breakthrough curve for synthetic α-FeOOH in electrolyte run 23 and α-Fe_2O_3 in electrolyte, run 24. H_a=9.1kOe and U_∞=0.9cm/s. 175

5-30 Breakthrough curve for clean CEZ jarosite in electrolyte, runs 25, 26 (at 25°C) and run 27 (at 75°C). (25) H_a=4.2kOe, U_∞=0.9cm/s. (26),(27) H_a=9.1kOe, U_∞=0.9cm/s. 176

5-31 Breakthrough curves for CEZ jarosite thickener overflow, runs 28 (at 25°C) and run 29 (at 75°C). H_a=21kOe, U_∞=0.9cm/s. 178

5-32 Magnet sizing curves for synthetic K jarosite (run 4) at processing rates of (a) 1.2cm/s. (b) 2.3cm/s. 183

5-33 Magnet sizing for synthetic NH_4 jarosite, runs 11,12,13, applied field of (a) 4.2kOe and (b) 9.1kOe. 184

5-34 Magnet sizing for CEZ jarosite in electrolyte at 75°C, run 27. Curve (a) C_{in}=150g/l solids, t_w=600s, (b) C_{in}=150g/L, t_w=120s. (c) C_{in}=15g/L, t_w=600s. 188

5-35 Magnet sizing for CEZ jarosite overflow sample, run 29. C_{in}=3g/L (a) t_w=600s, (b) t_w=120s, (c) C_{in}=15g/L, t_w=600s. 191

Figure | Page

5-36 Breakthrough curves for CEZ jarosite, run 27 (a) Collan data fit (b) Nesset fit, b=1μm (c) Nesset, b=2μm. 193

6-1 Comparison of K,NH_4,Na jarosite breakthrough curves. H_a=4.2kOe, U_∞=0.9cm/s, in H_2O. 205

6-2 Comparison of FeOOH, Fe_2O_3 breakthrough curves. H_a=9.1kOe, U_∞=0.9cm/s, in H_2O. 206

6-3 Effect of field on breakthrough curves of NH_4 jarosite in H_2O. (a) H_a=4.2kOe, U_∞=0.9cm/s. (b) H_a=9,1kOe, U_∞=0.9cm/s. 207

6-4 Effect of viscosity on breakthrough curves of CEZ jarosite, H_a=9.1kOe, U_∞=0.9cm/s. (a) Electrolyte at 25°C. (b) Electrolyte at 75°C. (c) H_2O at 25°C. 209

6-5 Magnet sizing for CEZ Valleyfield jarosite overflow, C_{in}=15g/L solids, C_{max}=3g/L solids. 215

6-6 A proposed flowsheet for the augmentation of a conventional filtering system found in the zinc industry. 216

LIST OF TABLES

Table		Page
1-1	Composition of Iron Precipitates Found in Zinc Industry.	17
2-1	Composition of Akita and Datteln Hematite Precipitates.	51
4-1	Field Settings and Flow Rates Available for Filtration Test.	117
5-1	Experimental and Theoretical Diffraction Patterns for Jarosites.	124
5-2	Experimental and Theoretical Diffraction Patterns for (a)Fe_3O_4 and α-Fe_2O_3 (b) α and β FeOOH.	125-6
5-3	Chemical Analysis of Jarosites	131
5-4	Chemical Analysis of Electrolytes	135
5-5	Pycnometer Density Results for Precipitates	136
5-6	Sedigraph K_{50} Values for Precipitates	140
5-7	Magnetic Susceptibility Values for Jarosites and Goethites.	152
5-8	Magnetic Susceptibility and Magnetisation Values for Hematite.	154
5-9	Magnetisation Data for Stainless Steel Wires.	156
5-10	Viscosity and Density Measurements for CEZ Electrolytes.	157
5-11	Filtration Run Index.	159-60
5-12	Analysis of Backflush Effluent	179

Table		Page
5-13	Weight Distribution and Zinc Assay for Ferrite Separation.	181
5-14	Values of L,A and t_f for Magnet Sizing in Fig. 5-32.	185
5-15	Values of L,A and t_f for Magnet Sizing in Fig. 5-33.	186
5-16	Values of L,A and t_f for Magnet Sizing in Fig. 5-34.	189
5-17	Values of L,A and t_f for Magnet Sizing in Fig. 5-35.	192
5-18	Parameter Values for Magnet Sizing using the Nesset model (a) C_{in}=15g/L solids (b) C_{in}=3g/L solids.	195
5-19	Calculated Magnet Numbers Required from Nesset and Collan Models Based on Unit Size of 2.6m Diameter 0.5m Depth.	196
6-1	Comparison of Susceptibility and Magnetisation Values for Hematite.	200

I. INTRODUCTION

1.1. Concepts and Examples of Magnetic Filtration

The potential for physical separation of minerals by exploitation of the differences in their magnetic susceptibilities has been used since the beginning of the century. (1) High gradient magnetic separation (hgms) represents the latest in innovative technologies for the concentration of ore deposits. Examples of applications are in the kaolin industry (2,3) in the desulphurization of coal (4,5) and in the concentration of iron ores. (6) Similarly a considerable effort has been made to apply hgms to many other areas of ore benfeciation. The potential for upgrading of wolframite (7), molybdenite and taconitic iron ores has been demonstrated. (6)

Beneficiation of ores is not the only area of study in which hgms has been applied to solid separations. Particular interest has been shown in the treatment of leach residues (8) primarily for the possible upgrading of residues containing precious metals. A somewhat more exotic application of hgms is in the treatment of blood (9), where red blood platelets have been separated from the rest of the plasma. This versatility of the hgms technique in solid/solid separations has ensured that further applications in mineral beneficiation systems are inevitable.

The above processes deal exclusively with the solid/solid separation of a magnetic fraction from a mixed magnetic/non magnetic solids feed. Since the development of modern high gradient magnetic separators (10) their use as filters in removing solids from suspensions has received considerable attention. The majority of this work has been concerned with the removal of material from the waste-waters of several industries. In the treatment of municipal waters normally non magnetic material is rendered magnetic by the addition or "seeding" of the water with small quantities of magnetite. This non-magnetic material in the form of colloids, (11) bacteria (11) or viruses(17) is adsorbed onto the surface of the magnetite seed and is removed on passage through the magnet. The removal of non magnetic heavy metal ions from solution has always been of considerable interest in areas where the environment may be sensitive to their uncontrolled disposal. Nippon Electric (13) has developed a process whereby ferrous sulfate is added to contaminated solutions and is then coprecipitated as a ferromagnetic heavy metal ferrite ($M_xFe_3O_4$). The resulting slurry is then magnetically filtered and the clean effluent is recycled. In the treatment of steel mill waste waters whose sources may vary from rolling mill cooling waters, (14) to the gas scrubbers of oxygen convertors (15), successful filtration of a variety of solids has been achieved magnetically. In the former the solids to be removed are almost 100% ferromagnetic; in the latter only 10% of the material is magnetic. Here the addition of a flocculant allows the non magnetics to cluster around the ferromagnetic material and consequently be magnetically captured. A considerable economic advantage has been proven in using magnetic separation over conventional sand filters for this particular application. Again within the steel industry a study of further filtering for the removal of ferromagnetic fines from cold rolling mill lubricants has been made. (16) Although removal of large particles (> 1 mm) by permanent magnets placed in the oil sump has been standard practice, the removal of the very fine ferromagnetic particles (< 1 μm) has never been achieved. The considerable contamination of oil emulsions by iron fines presents the undesirable problem of roll abrasion and wear as well as the potential for chemical breakdown of lubricant. High gradient magnetic separation of these fines to levels of < 1 ppm Fe ensures long lubricant life as well as considerably increased roll protection.

Other developments in magnetic filtration now include the removal of corrosion products in both thermal and nuclear power plant waters.(18,19) Due to the high temperature of the system and the predominance of iron in their construction iron oxides are formed. These are converted to magnetite or some other form of ferritic spinel. Included in this spinel may be any other dissolved metal of a bi-valent type and of similar atomic radius. The ferromagnetic nature of this material again allows for promising filtering performance.

The examples of magnetic filtration so far discussed are those which have either already been adopted as industrial processes or at the very least show considerable promise. Many other noteworthy applications have been proposed and continue to be studied. These include the recovery of ion exchange resins;(19) precipitation and extraction of magnetite in acid mine drainage waters;(19) treatment of ferric hydroxide sludges by the addition of magnetic seeds;(20) and finally the collection of oil slicks by adsorption of oleophillic magnetic media.(21)

All of the filtering systems so far considered, deal essentially with the treatment of exclusively ferromagnetic material, (naturally present or added as seed) which is usually of fine particle size(< 100 mesh). This material may be easily filtered using either conventional magnetic separators or hgms devices operating at low fields.

Investigations of whether paramagnetic materials can be removed from such a variety of systems has not been as well documented. The problems concerning paramagnetic material are quite clear when considering them for treatment in magnetic filters. Their magnetic susceptibilities are of several orders of magnitude lower then ferromagnetics and consequently the cost of the production of strong field gradients for their capture must be taken into account. One example of filtering paramagnetics is given by Watson. (22) He has shown that in iron-containing waste water from a coal mine, dissolved ferrous iron in the acidic water on mixing with the local river water is oxidised and precipitated as hydrated ferric oxide. This undesirable precipitate was successfully filtered from the river water by using a high gradient magnetic separator. An economic comparison of this filtration and a proposed conventional settling lagoon system, showed that installation, operating and maintenance costs would be half of that projected for the lagoon operation.

Other studies of filtration of weakly magnetic materials include an innovative application in the nuclear power industry. (23) Paramagnetic radioactive compounds produced in the reactor chamber must be removed from associated cooling fluids prior to safe disposal. High gradient magnetic separators, because they can be completely enclosed and isolated, easily operated and maintained, allow operating personnel to be well screened from any radioactive sources.

The recovery of precipitated hydroxides from leach liquors (an alternative metal recovery process where electrowinning is not suitable), has been proposed (24) as a system which may benefit from magnetic filtration of the precipitates rather than the application of conventional flotation techniques.

1.2 Removal of Iron from Solution

The removal of iron from solution has been a considerable problem for many years in the metallurgical industry. Essentially the concern is in two areas. Firstly, the removal of dissolved iron from large volumes of waste or cooling waters associated with any ferrous industry; secondly, the inherent problem of iron removal during the primary production of non-ferrous metals. In this second case the iron is an integral part of the original ore and must be removed either during ore beneficiation or selectively rejected during the extractive process. Within ferrous industries removal of dissolved iron in water is achieved by precipitating the iron as hydroxide followed by thickening and filtering. A novel technique developed by Miura and Williams (20) allows seeding of this gelatinous hydroxide with magnetite and following flocculation, the removal from suspension of the magnetic flocs by rotating magnetic discs.

Within the hydrometallurgical industry iron removal from solution has always been and remains a considerable problem in the production of non-ferrous metals. The most common hydrometallurgical processes all contain an iron rejection stage, usually in the form of selective precipitation. Ammononiacal pressure leaching of copper or nickel concentrates, which usually involves a slight oxygen over-pressure, allows hydrolysis and oxidation of the associated dissolved iron in the form of hydrated ferric oxide. The precipitate is then rejected in the leach residue. (25) The primary metal, in the case of copper, is then electrowon from solution, or in the case of nickel by pressure hydrogen reduction. Pressure sulphuric acid leaching associated with copper and zinc ores requires the rejection of ferrous iron from solution. Again, with an oxygen overpressure and careful pH control, iron hydrolysis is achieved. Ferric hydroxide and basic ferric sulfate are then rejected with the leach residue. (26,27) Atmospheric leaching with ~~sulphuric or nitric acid of~~ copper concentrates again leads to the rejection of iron from solution as hydroxide. However, it has been proposed that an improvement in iron rejection may be achieved if the iron is precipitated as hydronium jarosite. (28) Lastly, roast- leach electrowin processes commonly associated with the hydrometallurgical production of zinc, have produced a variety of methods in the rejection of iron from leach liquors prior to electrowinning. These methods may be applied to almost any electrolyte or aqueous solution for iron rejection and will be discussed later in further detail.

At this point it is worth noting some less conventional methods to remove iron from acid solutions containing non-ferrous metals. Solvent extraction has been adapted to a number of processes for removing ferric iron. (29,30,31) Their common feature is the production of an extremely pure iron solution phase without the problem of residue disposal associated with the above precipitation routes. Indeed

Thorsen and Grislangas (32) have proposed a solvent extraction system for iron removal in the hydrometallurgical zinc industry. This would not only avoid the problem of iron residue disposal but also offer the prospect of a saleable iron product. Craigen et al (33) however, noted that at the extraction of pH of 2-4 required for solvent extraction there is a limited ferric iron solubility. This problem is heightened if extraction is from a sulfate media or in particular if high initial iron concentrations are present.

1.3 Iron Removal in the Electrolytic Zinc Industry

An example of one of the more important areas of iron removal from solution can be found in the electrolytic zinc industry. Here, the ability to keep iron levels in the electrolyte low while maintaining a high recovery of zinc has been of considerable technological and economic importance. The extractive process is a typical example of the roast-leach-electrowin type. Zinc calcine product from the roasting of sulphide concentrates is leached in dilute sulphuric acid (return electrolyte). This solution is then purified and sent to electrolysis. The calcine contains zinc in the form of oxide, ferrite, sulphate, sulphide and silicate. Weak acid leaching readily dissolves ~~the oxide and~~ sulphates but not the ferrite ($ZnFe_2O_4$) or unroasted sulphides. The latter two phases can contain as much as 15-20% of the recoverable zinc and require further treatment in strong hot acid. When the ferrite is dissolved, the unwanted iron also goes into solution. First generation hydrometallurgical plants deliberately limited calcine leaching to the zinc oxide phase, rejecting unleached ferrites and sulphides in the leach residue. This practice allowed low levels of iron to be maintained in the leach liquor, at the expense of zinc recovery. Any iron present was then oxidised to the ferric state and precipitated as gelatinous ferric hydroxide, after solution neutralisation. Although, by it nature, this material is difficult to filter and interferes with thickening, filtering and washing, the hydroxide did allow the scavenging of small amounts of deleterious impurities such as As, Sb and Ga. Higher concentrations of iron in solution become difficult to treat in this manner, as the volume of this unmanageable ferric iron precipitate increases and seriously impairs conventional solid/liquid separation processes. Consequently, within these plants, zinc recovery was held to 85-90% while electrolyte levels rarely rose above 1-2g/L.Fe, prior to iron hydrolysis. Leach residues (22%Zn, 32%Fe) in the form of zinc ferrites and sulphides were stockpiled for some thirty years awaiting the development of a suitable leaching technology. Some of these stockpiles contained up to quarter of a million tons of unrecovered zinc.

The introduction of the jarosite process (34,35) Fig.(1-1) has allowed a second generation of electrolytic zinc plants to be developed, specifically allowing both high zinc recoveries and the ability to reject large quantities of iron. The residues from "neutral acid leaching" are reacted in a second hot strong acid leach (spent electrolyte) where the zinc ferrites and sulphides are dissolved. The iron content of this solution maybe as high as 40g/L Fe. The solution is then neutralised to pH 1-2 with unreacted calcine and the iron precipitated close to 100°C as basic iron sulfates in the form $MFe_3(SO_4)_2(OH)_6$ where M is a monovalent cation of the form NH_4,K,Na or H_3O. This form of sulphate is termed jarosite and due to a comparatively high crystalline nature, is relatively easily thickened and filtered from electrolyte solutions. This system now allows 96-98% recovery of zinc while allowing < 1g/L.Fe in the return solution to the

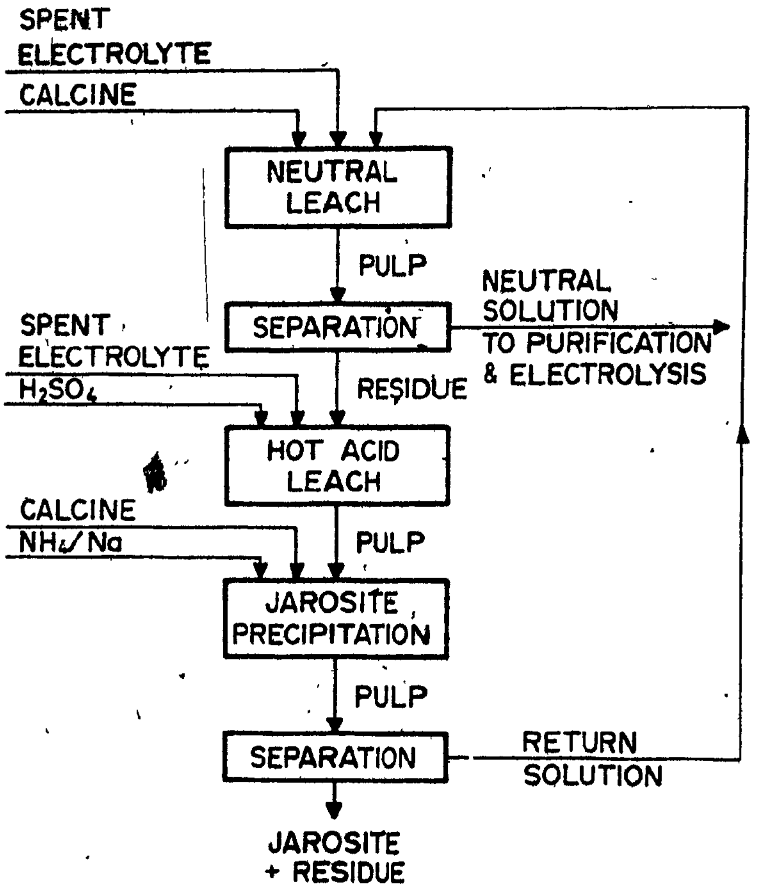

1-1 Flow sheet of basic Jarosite Process.

neutral acid leach and ultimately this level in the feed to final electrolyte purification. Industrially the jarosites produced are usually $NH_4Fe_3(SO_4)_2(OH)_6$ and $NaFe_3(SO_4)_2(OH)_6$, the alkali monovalent cation being added as either a gas, a hydroxide or in the case of sodium as sulfate. Plant practice varies worldwide according to the species and availability of the precipitating reagent used. In all cases, however, great care is taken in the control of the precipitation step (particularly of pH) in order that the required degree of crystallinity and ultimately particle size is achieved for efficient thickening, filtration and finally simple disposal of the jarosite residues.

Together with the jarosite process, two other systems have been developed for iron removal in the zinc industry. These are the goethite and hematite processes. Both techniques allow maximum zinc recovery after secondary leaching stages, while rejecting iron as an easily separated precipitate. In the Goethite process, ferric iron bearing solutions can be treated in two ways. In the original Vieille Montagne Process (36) the ferric solution is reduced to the ferrous state, then oxidised at 90°C together with solution neutralisation to pH 2-3.5. Iron

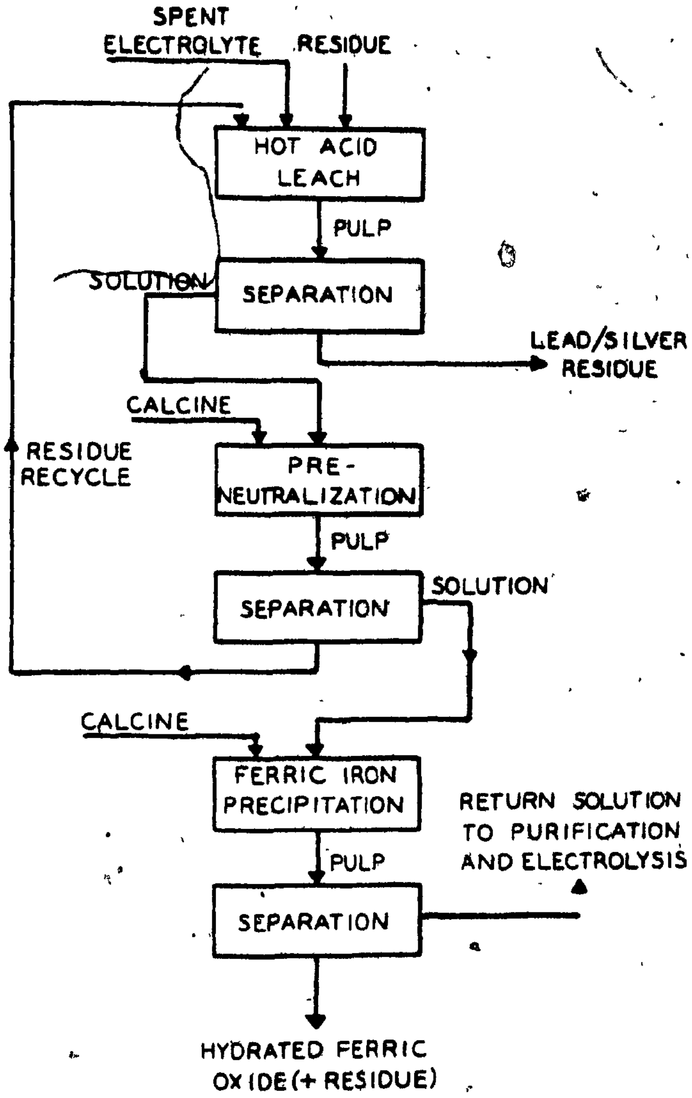

1-2 Flow sheet of the E.Z. Process.

is then precipitated as goethite ($FeOOH$). In the Electrolytic Electrolytic Zinc process (37), Fig. (1-2) the ferric solution is added together with a neutralising agent to a precipitation tank at 90°C. The rate of solution addition is equivalent to the rate of goethite precipitation, allowing dissolved ferric iron levels to be kept below 1g/L, while pH is maintained at around 2.5. Goethite precipitated in this fashion tends not to be of a single phase but rather as a mixture of α/β $FeOOH$ together with some Fe_2O_3 and other amorphous phases. The relatively high crystallinity of all these phases gives excellent filterability of the precipitate and the process itself limits dissolved ferric iron levels to 1g/L.

The hematite process (Fig. 1-3) initially developed by Akita Zinc Co. of Japan (38) and now proposed for a new zinc plant in Datteln West Germany, involves the treatment again of an initial neutral leach residue. In this case undissolved ferrite is treated with spent electrolyte and SO_2 in low pressure autoclaves at 95-100°C. After ferrite dissolution at which iron is reduced to the ferrous state, the solution is neutralised with lime to give a marketable gypsum product and to remove sulfate derived from the consumed SO_2. The iron is finally precipitated under 1.82×10^6 Pa

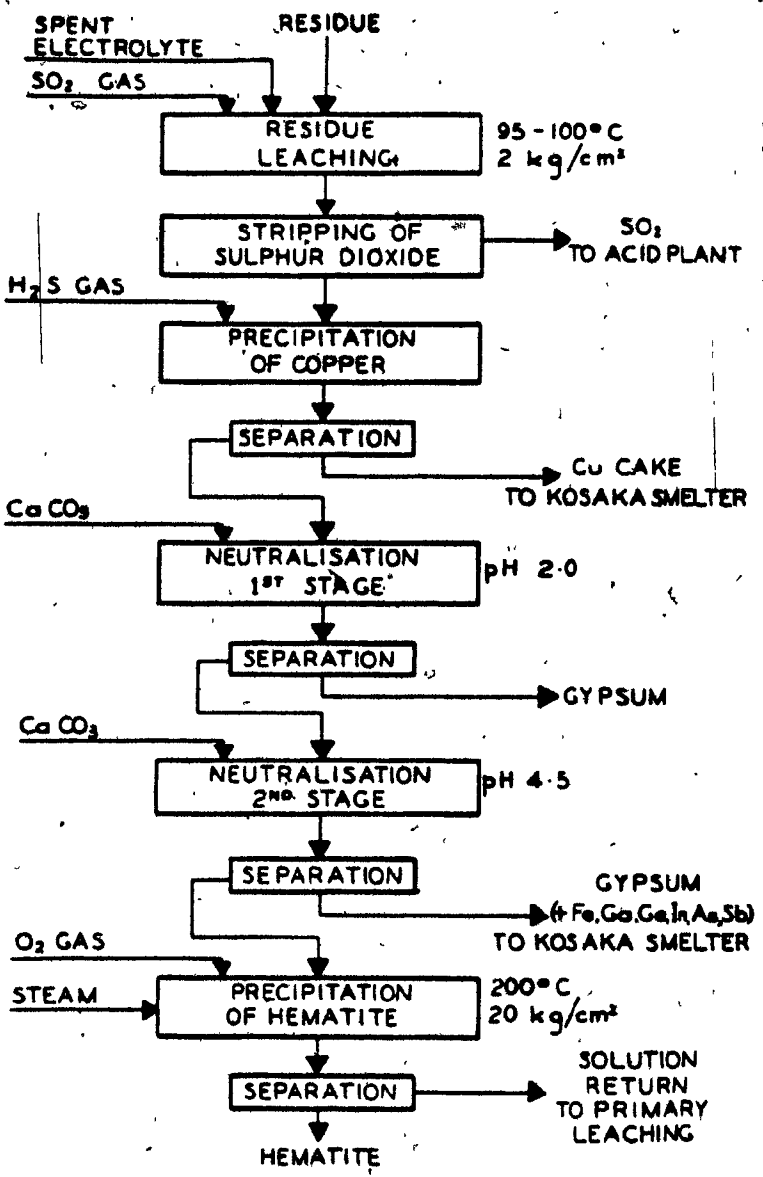

1-3 Flow sheet of basic Hematite Process.

TABLE 1-1

Composition of Iron Precipitates Found in the Zinc Industry

	Jarosite	Goethite	Hematite
Composition %			
Fe	25-28	40-45	58-60
Zn	4-6	5-8	0.5-1.0
Total Sulphur	10-12	2.5-5	3.0

O_2 pressure at 180-200°C as α-Fe_2O_3. Sulphuric acid generated during the hydrolysis does not hinder precipitation at these high temperatures. The precipitate is again of an easily filterable crystalline form.

Within the electrolytic zinc industry the choice of which hydrolysis/precipitation route to take for treatment of large amounts of dissolved iron is dependant on many factors. Table (1-1) shows the basic properties of each of the precipitation routes. The disadvantages of the jarosite process are apparent in that it produces a relatively high volume of solids, there is a high zinc to iron ratio and sulphur levels are high in the final discarded solids. This has resulted in considerable attention being paid to the Goethite and Hematite processes over recent years. The almost universal acceptance of the jarosite process was very much associated with the relatively simple chemistry involved and the ability to integrate the process into the then existing electrolytic zinc plants.

The problem of precipitate disposal has always been one of the major concerns of the zinc industry. Considerable land is required if dumping is contemplated and the potential for environmental problems due to the breakdown of the precipitate (39) must always be considered. New zinc plants have tended to incorporate either the goethite or hematite processes, allowing a reduction in the volume of precipitate to be disposed. This is particularly true of the Datteln plant where land is at a premium. The concept of precipitate treatment for recovery of iron has also influenced the decision of which precipitate route to take. The hematite process was initially designed to offer a perfect blast furnace feed for the iron and steel industry. However high sulphur levels (3% S) in the precipitate would have to be lowered by roasting if this treatment were contemplated. The use of jarosite and goethite residues as blast furnace feed has also been investigated (40) with some degree of success.

Such further treatment of these discarded residues serves a twofold purpose. Firstly, a marketable product may offset some of the original processing costs; secondly, any reduction in the space required for the storage of these residues would be of considerable economic advantage. This second factor is magnified somewhat if one considers the projected likelihood of increased zinc production from lower grade ores i.e. those ores containing higher iron and sulphur. The corresponding increase in the volume of iron precipitates produced, not only increases the problem of precipitate disposal but also affects the large thickening, filtering and washing systems associated with precipitate/ electrolyte separation.

1.4 Prospects for Magnetic Filtration of Iron Precipitates in the Zinc Industry

Of all the systems requiring removal of iron from solution, the electrolytic zinc industry provides the best example of a process where solid/liquid separation is an integral part of the extractive system. It also provides an example of an industry which has developed a variety of techniques for removing iron from solution in various forms. Magnetic filtration may represent a technology that could be applied to this industry in order, at the very least, to augment the very large thickening and filtering capacity required. This may be particularly true if an increase in present capacity is contemplated or if a rise in precipitate volumes occurs from the treatment of lower grade ores.

The basic success and advantages of magnetic filtration have already been well demonstrated. Whether it offers any prospects in the zinc industry, however, depends on the magnetic properties of the precipitate and electrolyte system. Naturally occuring crystalline samples of potassium jarosite (41) and FeOOH (42) indicate that these materials are weakly magnetic antiferromagnetics. Magnetic capture of a naturally precipitated iron hydroxide has already been documented. (43) The magnetic filtration performance of precipitates formed in high density electrolyte solutions is unknown.

Mathematical models of filter performance derived to predict recovery and filter efficiency have in the past been an aid not only in determining the feasibility of a particular solid/solid or solid/liquid separation but also in predicting the role of some of the more important operating parameters. The present study is concerned with determining whether precipitate filtration is feasible using the already developed magnetic filters available. The hydrometallurgical zinc industry has been selected for the study but it is considered that the work will be applicable to other iron removal problems.

II. PRECIPITATION OF IRON FROM SOLUTION IN THE ZINC INDUSTRY

2.1. General

The chemistry of iron precipitation from solution and the identity of the solid phases produced has only recently become clear. This is in large part due to the hydrometallurgical zinc industry's development of several iron precipitation processes and the associated basic chemical studies that have accompanied them. The studies have shown that the precipitation kinetics are quite complex and that considerable control of precipitation processes is required in order to produce the desired crystalline precipitate. The precipitates include

- Ferric Hydroxide
- Jarosites
- Goethite
- Hematite
- Magnetite

2.2 Ferric Hydroxide

The original production of zinc electrolyte (4) relied on the simple dissolution of zinc calcine (ZnO) in dilute sulphuric acid. This process is complicated by the simultaneous dissolution of impurities in the calcine such as As, Sb, Cd, Co, Ni, Sn, Cu as well as Fe. All of these are detrimental to the electrowinning of a pure zinc product. The precipitation of iron as hydroxide allowed not only iron removal from the zinc solution but also removal of these other impurities (in particular, As, Ge, Sb). It was considered that these elements were removed as either basic salts or absorbed onto the ferric hydroxide colloids. The ferric hydroxide, impossible to settle or filter in its colloidal state, was coagulated by raising the pH to at least pH 5.0. The mixture of unreacted calcine and hydroxide precipitate was thickened and the electrolyte sent for purification and electrolysis.

Fig. (2-1) (45) shows that the +2 and +3 oxidation states for iron are those that apply at the low pH within the zinc industry. Due to the high solubility of ferrous iron, ferric iron hydrolysis has always been considered in iron rejection systems. The basic equation is:

$$Fe_2(SO_4)_3 + (n+3)(H_2O) \rightarrow Fe_2O_3n(H_2O) + 3H_2SO_4 \qquad (2\text{-}1)$$

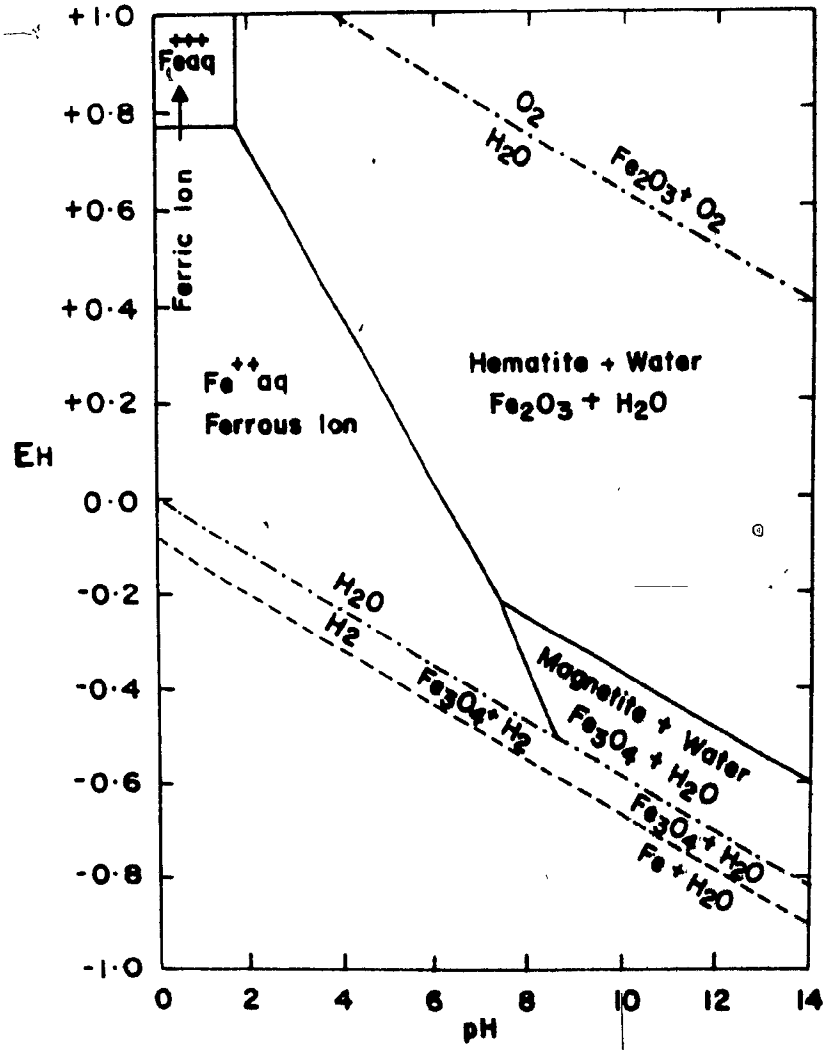

2-1 Eh-ph diagram for the iron-water system at 25^0 and at atmospheric pressure.

At the low acidities present during neutral acid leaching, ferric hydrolysis will take place (eqn. 2-1). Posnjak. and Merwin (46) studied the $Fe_2O_3 - SO_3 - H_2O$ system and the 75°C isotherm for the H_2O corner of the ternary diagram (Fig. 2-2). At low acidities the diagram predicts that as acidity in the solution decreases the precipitation of mainly $Fe_2O_3.H_2O$ rather than basic iron sulphate occurs. More recently, thermodynamic data relating to iron precipitation from sulphuric acid solutions has been reviewed by MacAndrew et al.. (47) These workers show that basic iron sulphate should not be a major hydrolysis product at low acidities. As shown in Fig. (2-3) $Fe(OH)_3$ should precipitate out as pH rises at 25°C. Freshly precipitated $Fe(OH)_3$ is slowly transformed to FeOOH and $Fe_2O_3nH_2O$ in an acid solution, these latter two precipitates having a lower solubility than that of $Fe(OH)_3$, as indicated in Fig. (2-4).(46) Thus a mixture of $Fe(OH)_3$, FeOOH and $Fe_2O_3nH_2O$ is likely to be produced as a result of ferric iron hydrolysis. Any ferrous sulphate present should be oxidised to ferric prior to hydrolysis:

$$4FeSO_4 + 2H_2SO_4 + O_2 \rightarrow 2Fe_2(SO_4)_3 + 2H_2O \qquad (2-2)$$

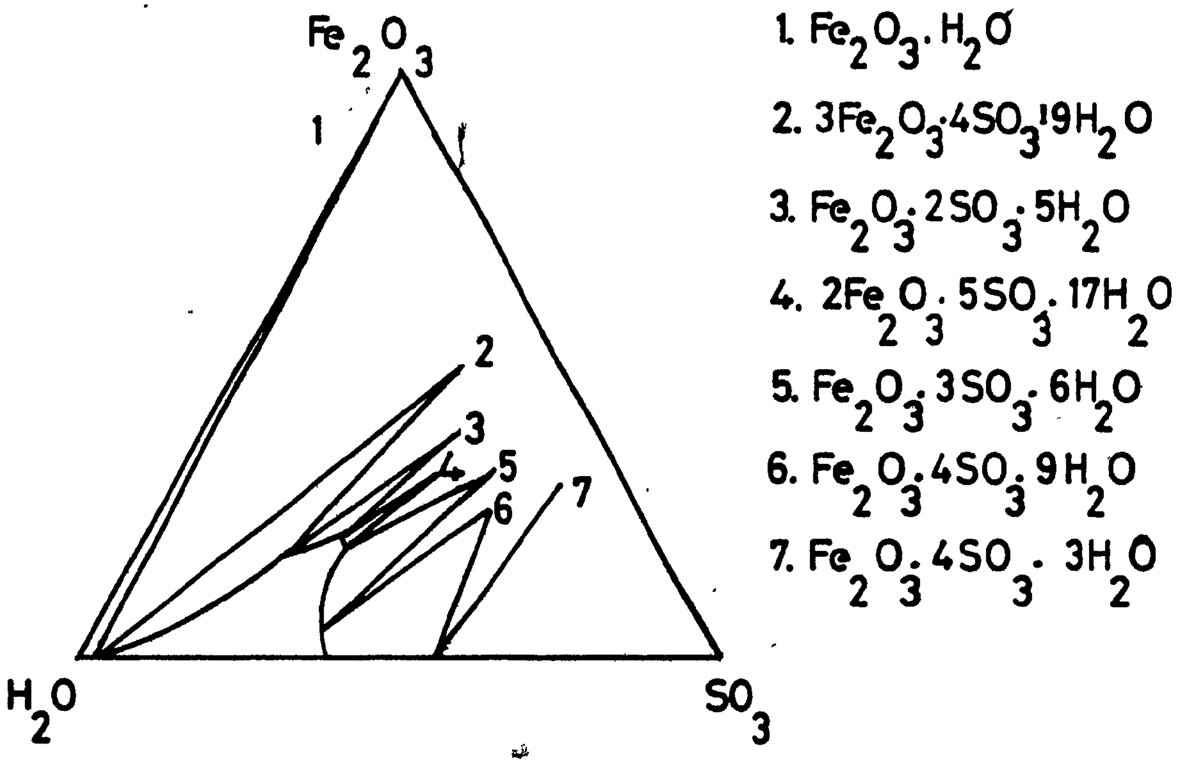

2-2 Fe_2O_3-SO_3-H_2O Equilibrium diagram at 75°C.

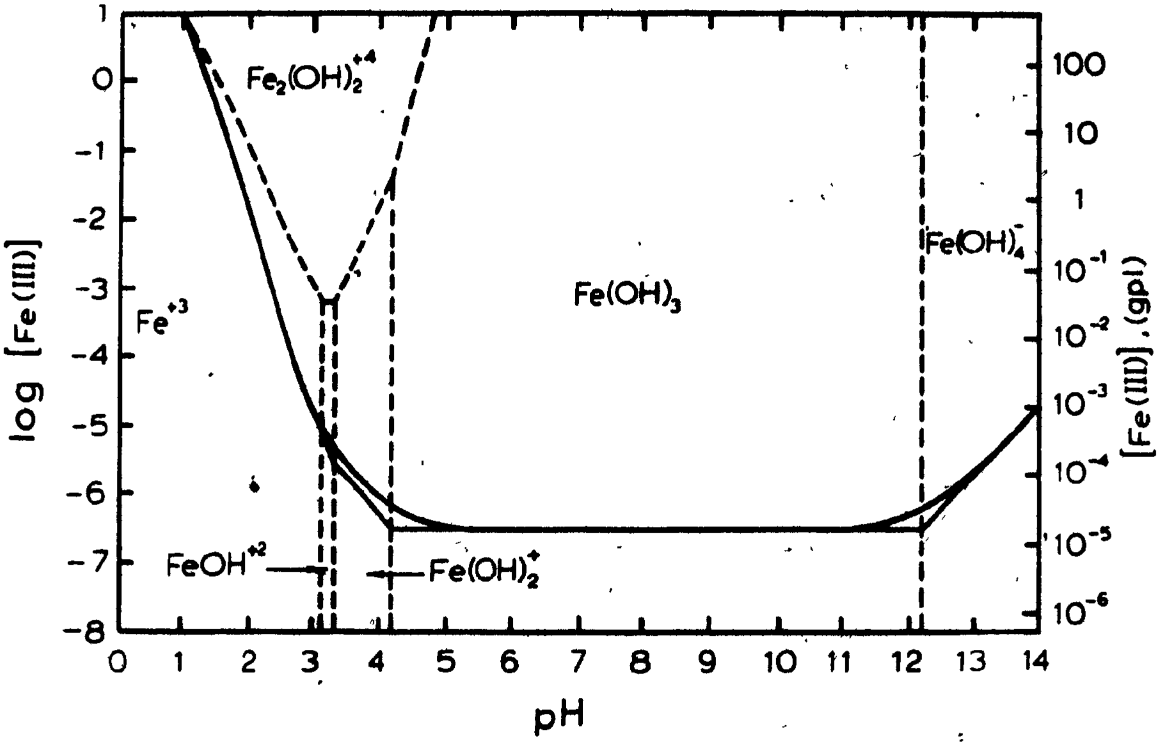

2-3 Solution species present, $Fe^{3+}-H_2O$ system at 25°C as a function of iron concentration and pH.

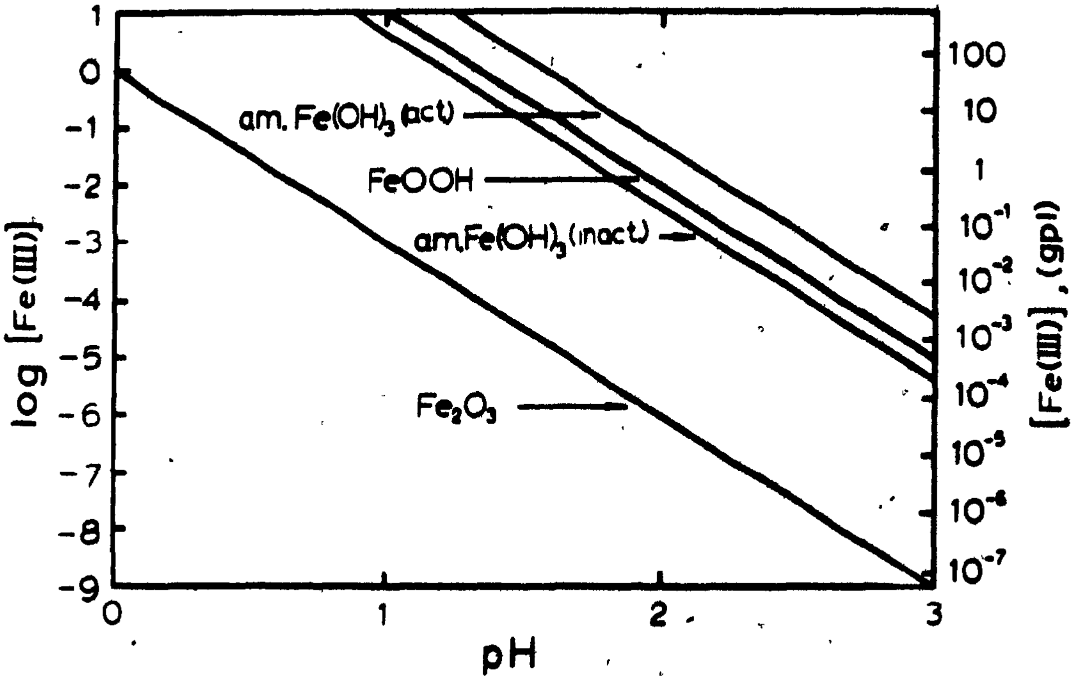

2-4 Solubility of iron(III) hydroxide and oxides at 25°C.

Previous studies $^{(48,49)}$ have suggested that under conditions applicable to the zinc industry (100°C and atmospheric pressure) this reaction will procede slowly, but with elevated temperatures and acidities an increase in the rate constant of the reaction will take place.

This concept of hydrolysis and precipitation of ferric hydroxide is somewhat oversimplified. There has been considerable effort to understand the precipitation processes of the $Fe^{3+} - SO_4 - H_2O$ system. Several studies $^{(47,50,51)}$ have concluded that the presence and production of sulphate, bisulphate and hydroxyl complexes play a large part in determining the form of the precipitate produced, even though these species may not precipitate themselves. The predominance area diagrams by MacAndrew et al $^{(47)}$ (Fig. 2-5,6) for sulphate, bisulphate and hydroxyl solution species for 25°C and 140°C have shown how elevated temperatures increase the area of stability of the sulphate-bisulphate complex region, but for the precipitation conditions prevalent in the zinc industry, hydrated ferric ion and the dimer $Fe_2(OH)_2^{4+}$, (considered as one of the most important hydroxyl species complexes formed during hydrolysis) $^{(52,53)}$, are the phases which appear to be most important.

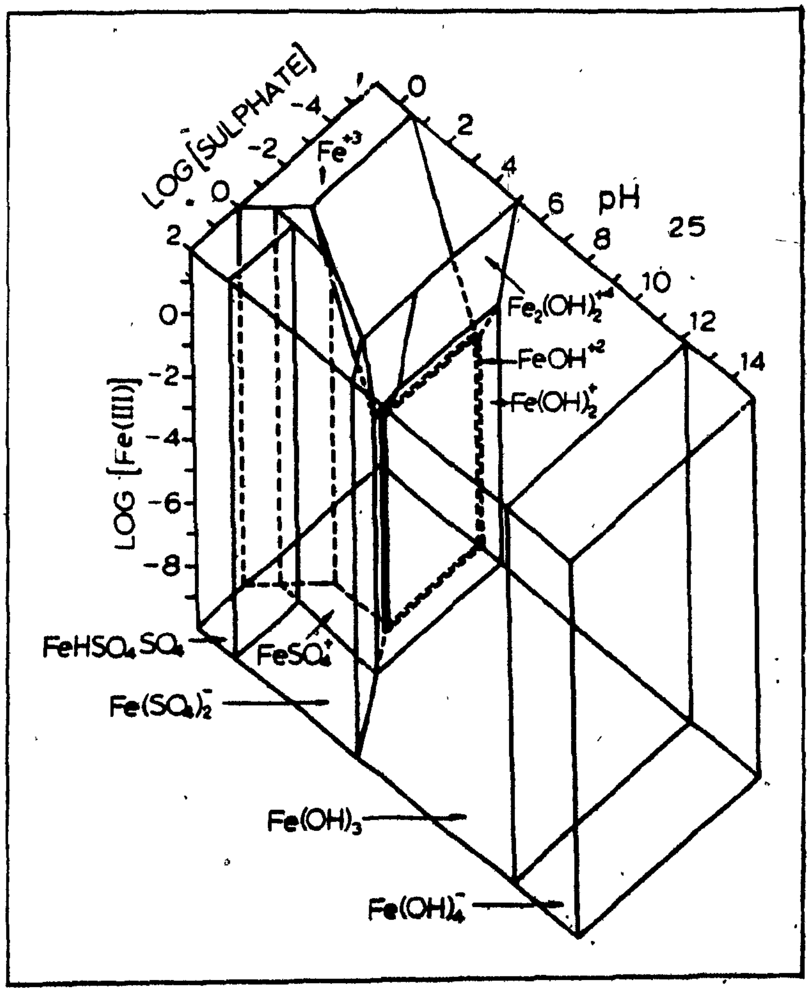

2-5 Predominance-volume diagram for the iron (III)-sulphate water system at 25°C.

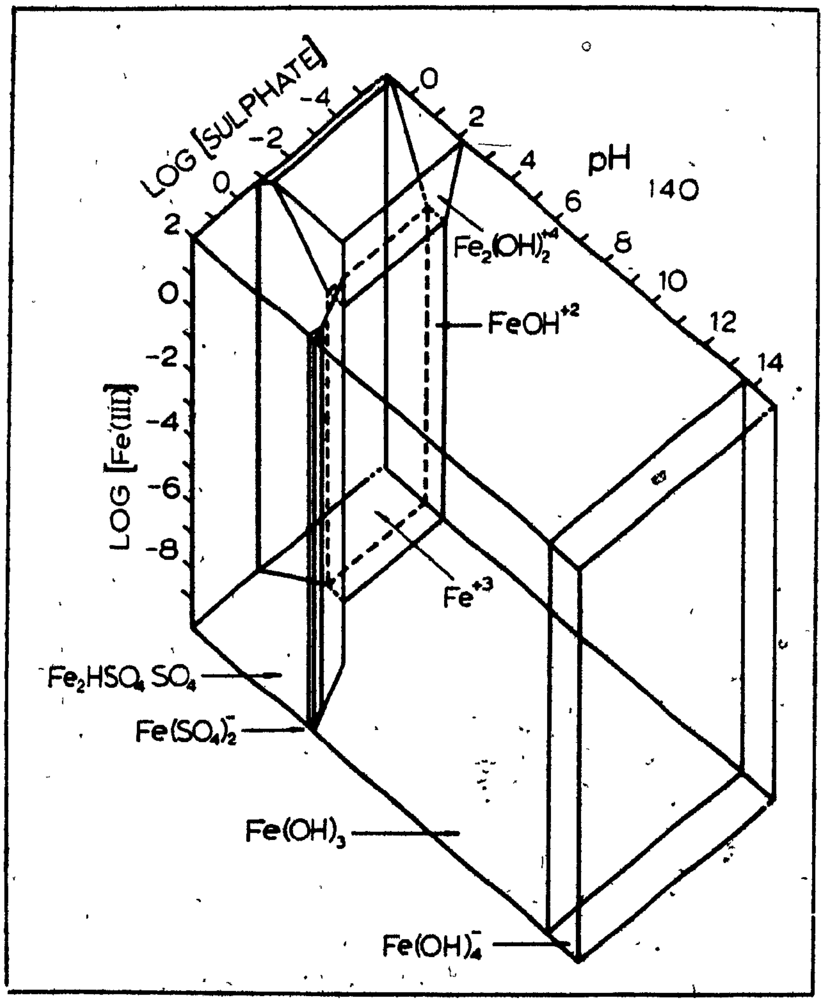

2-6 Predominance-volume diagram for the iron (III)-sulphate water system at 140°C.

The formation of actual solids from solution is dependent on the initiation and growth of small iron polymers from the initial hydroxyl or sulphate bisulphate complexes. As an example the dimer $(Fe_2(OH)_2)^{4+}$ and its reaction with the surrounding environment is given as (39)

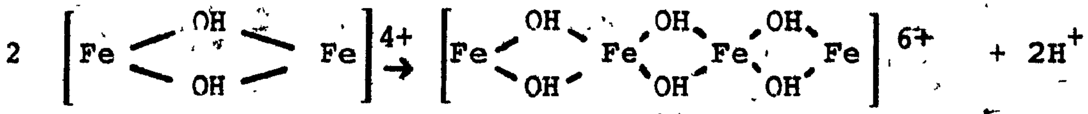

The formation of crystalline compounds occurs by further growth of these polymer forms. In the production of ferric hydroxide continued solution neutralisation allows polymer cross linking to take place using hydroxyl bridges (Fig. 2-7). This simple polymer coagulation is the common process of iron hydroxide gel formation and largely accounts for the poor filterability it exhibits. The formation of this hydroxide gel is also aided by the presence of the excess base added for neutralisation. This tends to promote the hydroxyl bridging rather than a more stable crystalline phase.

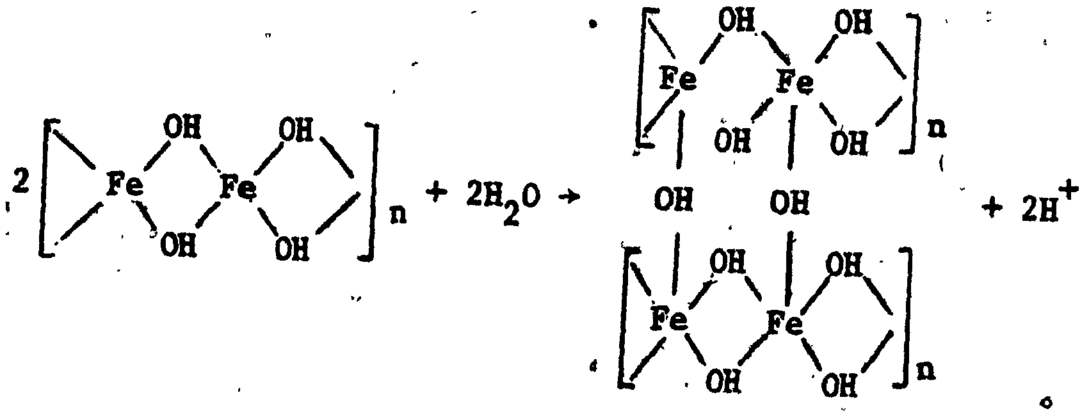

2-7 Growth of polymer forms by hydroxyl bridging.

2.3 Jarosite

The introduction of the jarosite process to the zinc industry (34,35) has led to a virtual revolution in iron precipitation technology. The ability to precipitate iron from acid solutions as crystalline compounds similar in form and structure to the naturally found carphosiderite $(H_3O) Fe_3(SO_4)_2(OH)_6$ or jarosite $K\ Fe_3\ (SO_4)_2(OH)_6$, allowed increased recovery of zinc as well as the production of a leach residue considerably enriched with valuable elements such as lead and silver.(54) The conditions under which these compounds form are essentially those of moderately high temperature and acidity (pH 1.5) allowing the formation and precipitation of basic iron sulphate complexes which react during hydrolysis with added reagents to form the desired jarosite species. A variety of jarosite type compounds have been formed and identified. (55) The general reaction mechanism may be described by the equations below using NH_4^+ as the added cation:

$$3Fe_2(SO_4)_3 + 6\ H_2O = 6\ Fe(OH)SO_4 + 3H_2SO_4 \qquad (2-3)$$

$$4Fe(OH)SO_4 + 4H_2O = 2Fe_2(OH)_4SO_4 + 2H_2SO_4 \qquad (2-4)$$

$$2Fe(OH)SO_4 + 2Fe_2(OH)_4SO_4 + 2NH_4OH =$$
$$(NH_4)_2Fe_6(SO_4)_4(OH)_{12} \qquad (2\text{-}5)$$

The studies of Posnjak and Merwin (46) of the Fe_2O_3-SO_4-H_2O system provide information on the identity of the stable compounds at elevated temperatures and acidities (Fig. 2-8). The isotherm given by Posnjak and Merwin for 110°C indicates that at the acidity and iron concentration levels pertinent to zinc processing, jarosite (as carphosiderite) is in equilibrium with the ferric solutions present. Decreasing iron and acidity tends to promote the formation of hydrated iron oxides. Further studies by MacAndrew,(47) Brown (56) and Umetsu et al (57) have provided Eh-pH diagrams for the Fe - SO_4 - H_2O system at 95°C (Fig. 2-9). Jarosite in the form shown here, ($KFe_3(SO_4)_2(OH)_3$), is stable at the lower pH range and under oxidising conditions. Above a pH of 3.3, the jarosite will slowly decompose to hematite.

Promotion of a jarosite phase takes place naturally with the addition of alkali ion due to the decrease in iron solubility at a given pH. Hydronium jarosite $H_3OFe_3(SO_4)_2(OH)_6$ can form in the absence of

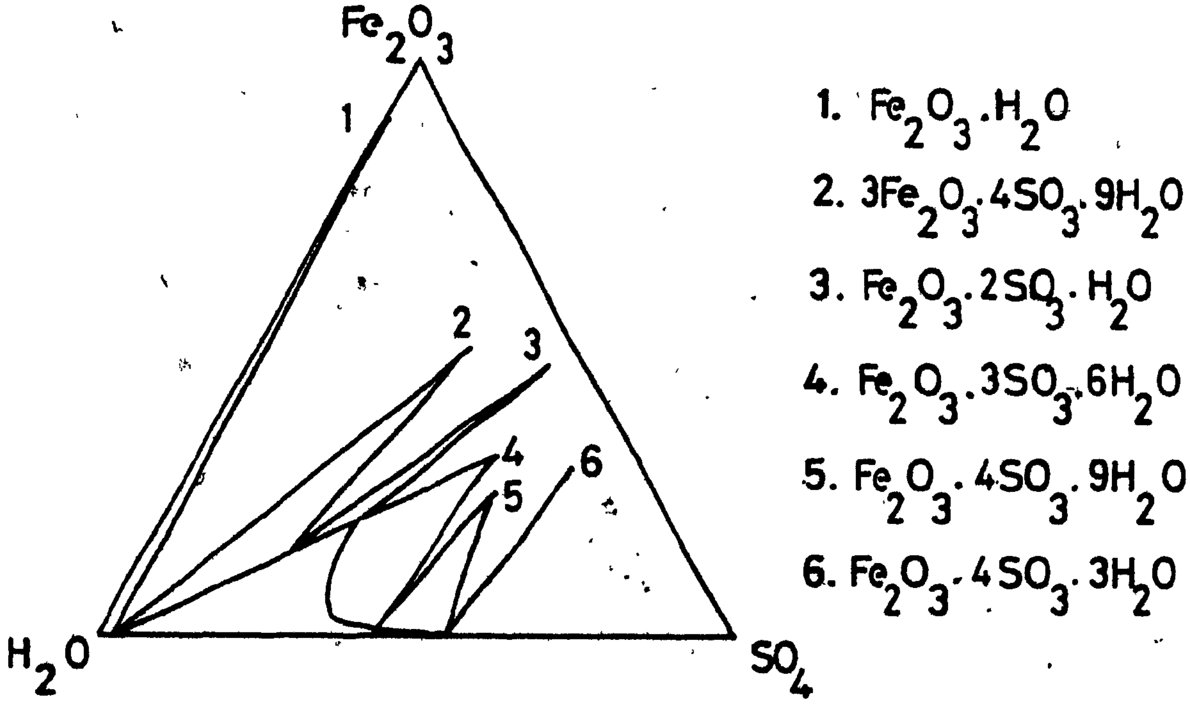

2-8 Fe_2O_3-SO_3-H_2O Equilibrium diagrams at 110°C.

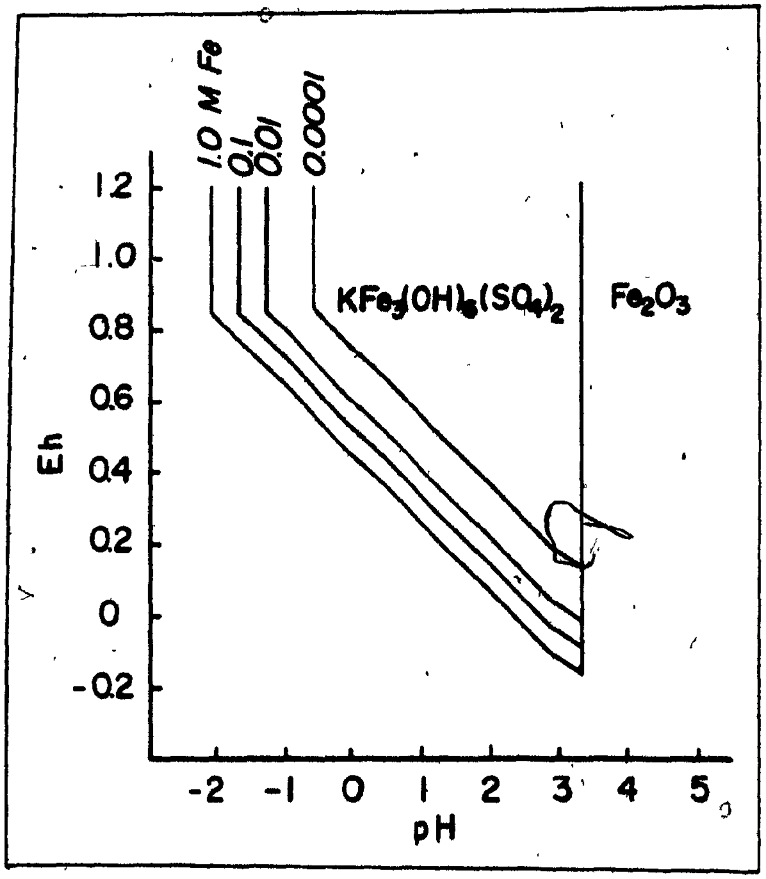

2-9 Jarosite-stable region in potential-pH diagram of Fe-SO_4-H_2O system at 95°C, [K] = 10^{-2}M, [H_2SO_4 + SO_4^{2-}] = 1M.

alkali but more often the H_3O^+ ion is found substituted into the alkali jarosite phase as well. The extent of this iron substitution is apparently dependent on the reaction temperature.(58) Dutrizac and Kaiman (55) have documented the non stochiometric nature of the added alkali in the formation of synthetic jarosite compounds and attributed this to the solution of the hydronium ion within the normal jarosite phase.

Conditions for efficient jarosite precipitation have now been well documented. Elevated temperatures and a control of pH (49) below pH2 allow increased iron removal while restricting the precipitation of unwanted iron phases. Alkali ion addition can be kept to stoichiometric levels and the presence of $ZnSO_4$ has little effect on the thermodynamics of the precipitating system. (59) Seeding of the electrolyte considerably improves the precipitation process. This appears to be due to a reduction in the initial induction period, which is apparently required before precipitation takes place. (54) This induction period is probably related more to the time required for the formation of the correct ion species prior to actual solid precipitation.(39)

Unlike ferric hydroxide, jarosites are a true crystalline phase having the same structure as alunite ($KAl_3(SO_4)_2(OH)_6$). This structure is described by Rossman et al. (41) Fig. 2-10 shows a slightly distorted octahedral polyhedra with each polyhedron having four bridging hydroxides in a plane with sulfate groups at each apex. Three of the sulphate groups are co-ordinated to metal ions which are joined together by the sulphate groups and the network of dihydroxy bridges. The octohedra combine to form sheets which are separated by uncoordinated oxygens and the alkali cations.

Impurity ions found in the electrolyte solutions of the zinc industry may also precipitate out to a limited extent as substitutions for sulphate, in the case of As and Sb, or for hydroxyl ion in the case of fluoride, both of which are advantageous to the process in decreasing the amount of impurities in the electrolyte prior to electrolysis. Substitutional zinc losses appear to be minimal providing lead jarosite formation is held to a minimum. (39) Most zinc losses take place during final filtering and washing operations.

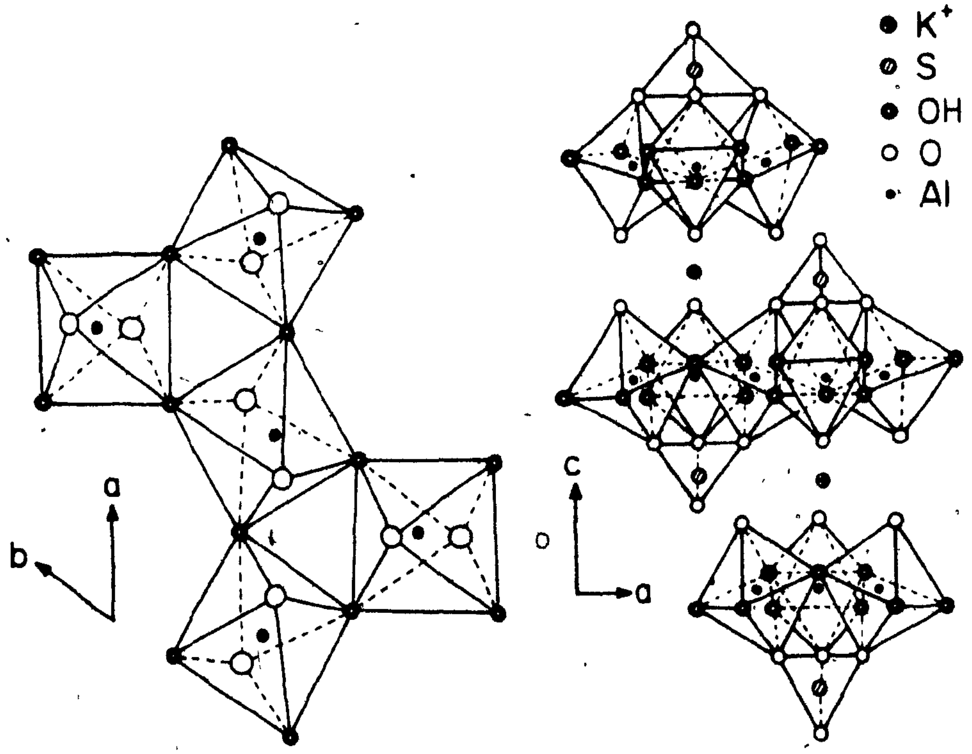

2-10 Structure of alunite $KAl_3(SO_4)_2(OH)_6$

2.4 Goethite

The goethite process was originally developed simultaneously by the Société de la Vieille Montagne (VM) (36) at Balen Belgium and the Electrolyte Zinc Company of Australia, (EZ) (37) as an alternative to the jarosite process. Although the jarosite and goethite processes display similar economics (60) goethite precipitation was felt to be advantageous in that the need for reagent addition was eliminated while the production of a stable residue was not inhibited. The particularly strict chemical control required in the goethite process probably accounts for the reluctance to use this precipitation route. (61)

In the VM process, following the normal neutral and hot acid leaching stages, dissolved ferric iron in the electrolyte is reduced to the ferrous state by the addition of unroasted zinc sulphide:

$$Fe_2(SO_4)_3 + ZnS \rightarrow ZnSO_4 + FeSO_4 + S^o\downarrow \qquad (2\text{-}6)$$

The sulphur produced and unreacted sulphide is returned to the roaster, while the solution is neutralised to pH 2.5 and maintained at a temperature of around 90°C. At this point air is injected into solution and the ferrous

8

iron is oxidised to the ferric state. As this takes place hydrolysis occurs and iron is precipitated as goethite, (FeOOH). Acid produced from hydrolysis is neutralised with added calcine, maintaining the solution at the required pH. The overall reaction may be expressed as:

$$4FeSO_4 + 4ZnO + O_2 + 2H_2O = 4FeOOH + 4ZnSO_4 \qquad (2\text{-}7)$$

In the EZ process, although similar to that of the VM procedure, no reduction of the ferric iron, found in solution after leaching, takes place. Here ferric iron solution, at elevated temperature (90°C) to promote hydrolysis, is added with neutralizing agent (calcine) to a precipitation tank containing a solution of dissolved ferric iron at < 1g/L Fe^{3+}. On addition of the leach solution to the precipitation tank, iron hydrolysis and precipitation takes place, while dissolved ferric iron levels are maintained at < 1g/L Fe^{3+} by controlling pH levels with calcine addition at around pH3.

The isotherm produced by Walter-Levv and Quemeneur (62) for the $Fe_2O_3 - H_2O-SO_3$ system at 100°C (Fig. 2-11) gives some indication of the solubility of the various iron

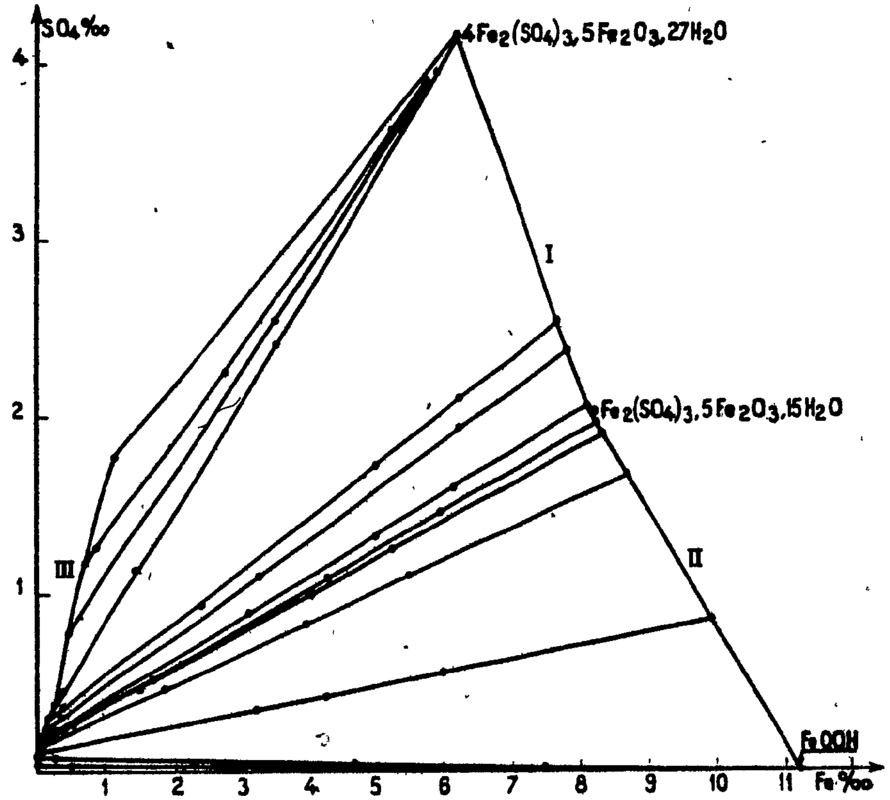

2-11 Portion of the Fe_2O_3-H_2O-SO_3 phase system at 100°C.

compounds in equilibrium with ferric sulphate solutions. For goethite precipitation to take place or alternatively to avoid the precipitation of basic ferric sulphate, ferric iron levels have to be kept below approximately 0.1%Fe^{3+}.(47) The provisions made in the VM and EZ processes to avoid high ferric iron levels during hydrolysis and precipitation are basic to the production of goethite.

Identification of the precipitated phases in both processes has been determined by Davey and Scott.(63,64) Three phases α- FeOOH, β-FeOOH and α-Fe_2O_3 appear to precipitate, depending on the precipitation conditions. Although α-Fe_2O_3 is a more thermodynamically stable compound, Langmuir (65) has shown that for the transformation:

$$2FeOOH \rightarrow Fe_2O_3 + H_2O \qquad (2\text{-}8)$$

The free energy ΔG^o for the reaction is a function of the size of the initial particulates formed. Goethite stability is increased by keeping the particle size small.

During the precipitation goethite and hematite share the same initial iron polymer of the form:

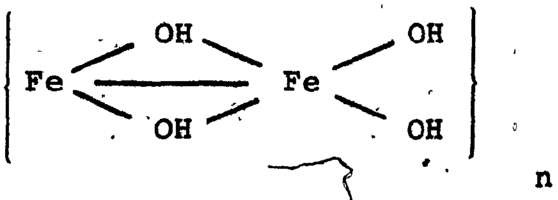

Providing a large excess of base is not present during solution neutralisation, this polymer chain may oxalate such that:

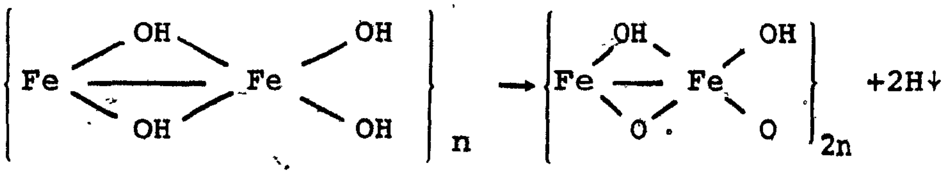

This polymer form is the precursor of either goethite or hematite. These polymers have been identified as small solids (66,67,68) in the form of rods which ultimately come together to form small particles $\approx 1\mu m$.(69) Two factors appear to play an important role in determining which particular variety of FeOOH or Fe_2O_3 is produced. Elevated temperatures appear to favour the formation of α-Fe_2O_3 (70) while the identity of the complexing anion of the initial hydroxyl polymer determines the phase of FeOOH formed. General trends show that Cl^- and F^- anions favour the production of β-FeOOH (63,71) while SO_4, Br, NO_3 favour the formation of β-FeOOH. Explanations as to the importance of the anions and the exact mechanism involved inducing the respective goethite phases are as yet not clear. Dissolved anions in the goethite structure which are not removed by simple water washing may make up 6% of the total weight of the precipitate in the case of the chloride ion or 15% in the case of the sulphate ion.(64) It would seem that their presence contributes significantly to the goethite phase formed.

2.5 Hematite

The hematite process (38) is the last of the new iron precipitation procedures used industrially in electrolytic zinc plants. The process was developed by the Dowa Mining Co. after original studies by the Electrolytic Zinc Co. of Australia (72) and Sherrit Gordon.(73) It was first used by the Akita Zinc Co. of Japan and is now proposed for the Datteln Zinc Plant in West Germany. The process consists of treating primary leach residue (unleached zinc ferrite), in such a way that the iron in solution remains in the ferrous state prior to iron hydrolysis and precipitation as hematite. This is achieved by dissolving the solids in a mixture of spent electrolyte, make up acid and added SO_2. Under these conditions ferric iron is reduced to the ferrous state:

$$2Fe^{3+} + SO_2 + 2H_2O \rightarrow 2Fe^{2+} + SO_4^{2-} + 4H^+ \qquad (2\text{-}9)$$

The solution is now treated first for copper removal (by precipitation with hydrogen sulphide) and then neutralized in two stages by lime addition to pH4.5. The gypsum produced is considered to be a marketable product. After neutralisation the solution is heated to 200°C under approximately 1.8 x 10^6 Pa. O_2 pressure. Iron is precipitated as hematite after oxidation of ferrous sulphate and subsequent hydrolysis:

$$2FeSO_4 + 0.5O_2 + H_2SO_4 \rightarrow Fe_2(SO_4)_3 + H_2O \qquad (2\text{-}10)$$

$$Fe_2(SO_4)_3 + 3H_2O \rightarrow Fe_2O_3 + 3H_2SO_4 \qquad (2\text{-}11)$$

or

$$2Fe\ SO_4 + 0.5O_2 + 2H_2O \rightarrow Fe_2O_3 + 2H_2SO_4 \qquad (2\text{-}12)$$

An optimum reaction time of three hours allows iron levels in the solution to reach about 3g/l. Fe^{3+} while acid produced during hydrolysis is returned to the primary leaching circuit after filtration of the precipitate.

Original studies by Posnjac and Merwin (46) and later by Umetsu et al (57) for the Fe_2O_3 - H_2O -SO_3 system at 200°C (Fig. 2-12) show clearly that hematite precipitation is favoured when acidity levels are low, whereas at increased acid levels mixtures of Fe_2O_3 and

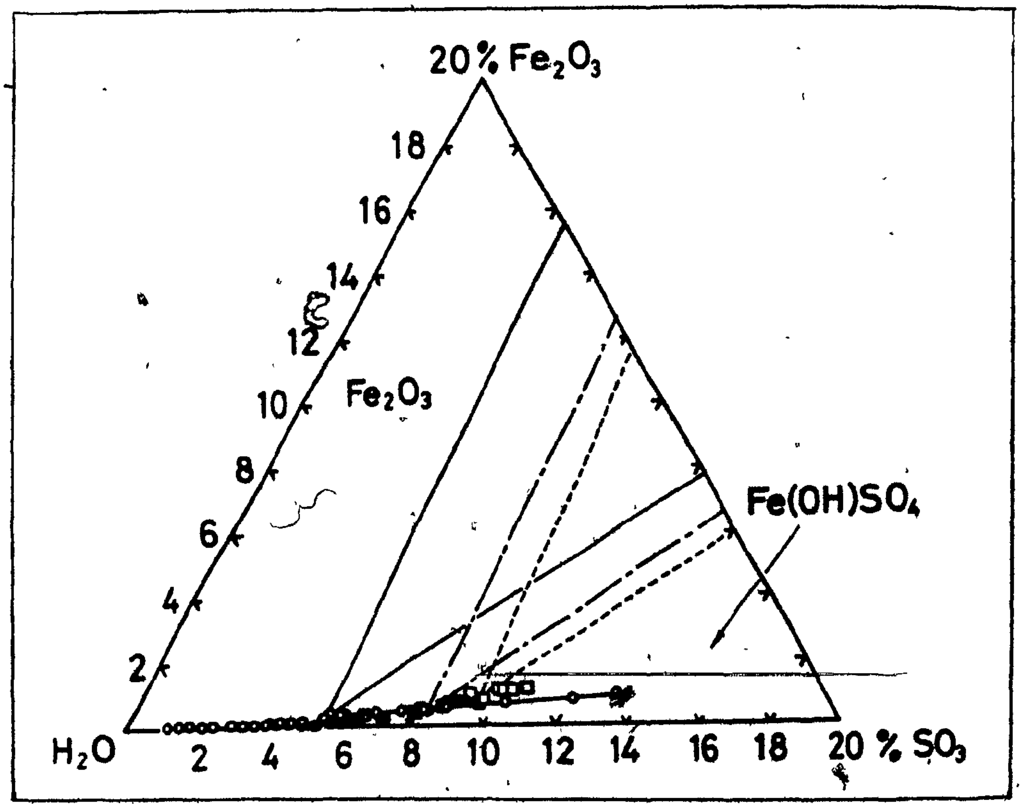

2-12 Fe_2O_3-SO_3-H_2O equilibrium diagram at 200°C. Dashed lines indicate effect of 75g/L Zn addition.

basic sulphates are likely. Basic sulphates are undesirable as they increase the sulphur levels in the precipitated product, which was originally considered (29) to be a marketable blast furnace feed. In the presence of $ZnSO_4$ there is a considerable increase in the range of hematite stability at these elevated temperatures. (57) Fig. (2-12) shows that with 75g/L Zn present, Fe_2O_3 is stable up to acid concentrations of about 85g/L. Umetsu et al have also established how elevated temperature improves iron rejection from solution, with a considerable decrease in iron solubility taking place between 150°C - 200°C. The precipitation of iron as hematite from zinc sulphate solution requires close chemical control. Although thermodynamically, hematite formation is favored upon the oxidation of ferrous iron solutions (Fig. 2-1) it is apparent that several other factors have to be taken into account in order to obtain a satisfactory precipitate.

The filtering quality of the precipitate produced industrially is reported as being excellent and this is in great part due to the relatively crystalline nature of the hematite produced. As discussed previously the precursor to the hematite crystal appears to be a polymer chain based on the dimer $Fe_2(OH)_2^{4+}$ which during solution neutralisation or at elevated temperatures is allowed to oxolate to form large polymers, which in the case of hematite formation are probably highly crystalline. The single crystallites produced tend to be larger than 1μm and do not agglomerate as do those found with goethite formation.

Improvements in calcine quality and the control of the leaching and neutralizing stages of the hematite process has allowed the impurity levels in the hematite precipitate to be decreased considerably. Pilot plant hematite residues at the Datteln operation are compared to those found at the original Akita plant, Table (2-1). Considerable improvement can be seen in reducing the sulphur content of the residue while iron levels approach the theoretical for hematite.

2.6 Magnetite

The removal of iron from solution by precipitation of magnetite has not been developed industrially. However the chemistry for magnetite production is relatively well understood due to the interest stemming from the removal or iron from waste waters (13,74) and in the production of ferrites for the electrical industry. (75)

TABLE 2-1

Compositions of Akita and Datteln Hematite Precipitates

	Akita	Datteln
Fe %	58	63.5
Zn %	0.5	0.8
S %	3.0	1.5

The ferromagnetic nature of the precipitate immediately makes it of interest in applications where magnetic filtration may be considered as an alternative to conventional solid/liquid separation.

The chemistry of magnetite precipitation may again be predicted from the Eh-ph diagram of the iron water system. Magnetite appears to be stable in ferrous iron solution under slightly reducing moderately alkaline conditions. From the original treatise by Mellor, (76) Kunda and Hitesman (77) delineated three sets of chemical conditions for the precipitation of magnetite. All involve the oxidation of ferrous sulphate solutions in the presence of a strong neutralizing agent. The method considered to be most successful and appropriate to applications in the zinc industry involves the addition of ammonia into ferrous sulphate solutions under 1.72×10^5 Pa. O_2 pressure. The reactions taking place are assumed to be:

$$3FeSO_4 + 6NH_3 + 6H_2O \rightarrow 3Fe(OH)_2 + 3(NH_4)SO_4 \qquad (2\text{-}13)$$

$$2Fe(OH)_2 + 0.5O_2 + H_2O \rightarrow 2Fe(OH)_3 \qquad (2\text{-}14)$$

$$Fe(OH)_2 + 2Fe\ (OH)_3 \rightarrow Fe_3O_4 + 4H_2O \qquad (2\text{-}15)$$

The mechanism of magnetite formation is reported (77) as being the oxidation of the ferrous hydroxide to the ferric state and the subsequent reaction of the two hydroxides to form magnetite. Properties of the precipitate and the behaviour of the solution during precipitation are shown in Fig. (2-13). Precipitation times are considerably shorter than those found in other iron precipitation routes while rejection from solution is almost complete.

A serious drawback to the application of this process to the zinc industry is the tendency to co-precipitation of divalent metal ions, present in the solution as impurities, by the formation of ferrites:

$$XM^{2+} + Fe^{2+}_{3-x} + 6(OH)^- \rightarrow M_xFe_{3-x}(OH)_6 \qquad (2\text{-}16)$$

$$M_xFe_{3-x}(OH)_6 + O_2 \rightarrow M_xFe_{3-x}O_4 \qquad (2\text{-}17)$$

Kunda and Hitesman indicate that zinc losses in the precipitate were such that 99% of 0.05M Zn present in the original solution would be precipitated with the magnetite. This is clearly an intolerable loss and consequently interest in this iron precipitation technique has been more associated with waste water treatment rather than hydrometallurgical processes.

NEUTRALIZATION-OXIDATION OF $FeSO_4$ SOLUTION

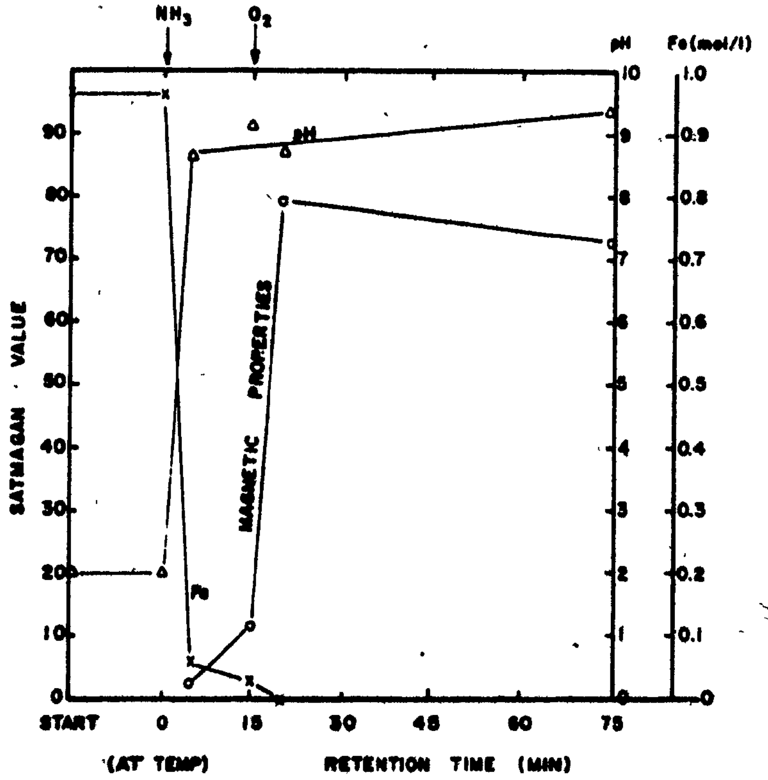

2-13 Behaviour of (a) magnetic properties, (b) pH and (c) iron, during precipitation of Fe_3O_4 from $FeSO_4$ solution by neutralization and oxidation treatment. Conditions: 100°C, NH_3/S molar ratio 2.2, 0.17MPa O_2.

III. MAGNETS AND MAGNETIC CAPTURE MODELS

3.1. Magnets

Although a variey of magnetic separators/filters have been adopted within the mineral processing industry, the present work is concerned with the Kolm-Marston device developed at the Massachusettes Institute of Technology.(78)

The basic separator consists of an iron clad solenoid, the working volume of which is filled with a filamentary matrix consisting of either stainless steel wool or expanded metal lath (Fig. 3-1). The solenoid is surrounded by an iron frame to allow not only an extension of the uniform field in the solenoid bore, but also a condense route for flux return. The ferromagnetic and filamentary nature of the matrix allows the production of very high magnetic gradients around the wires by perturbation of the uniform magnetic field. Together with the production of high background fields, these high gradients allow for the capture of small (< 1μm) weakly magnetic particles which are passed through the separator. Initial devices were of a batch design (Fig. 3-2). Used as a separator, a slurry of mixed solids is passed through the magnet and the magnetic

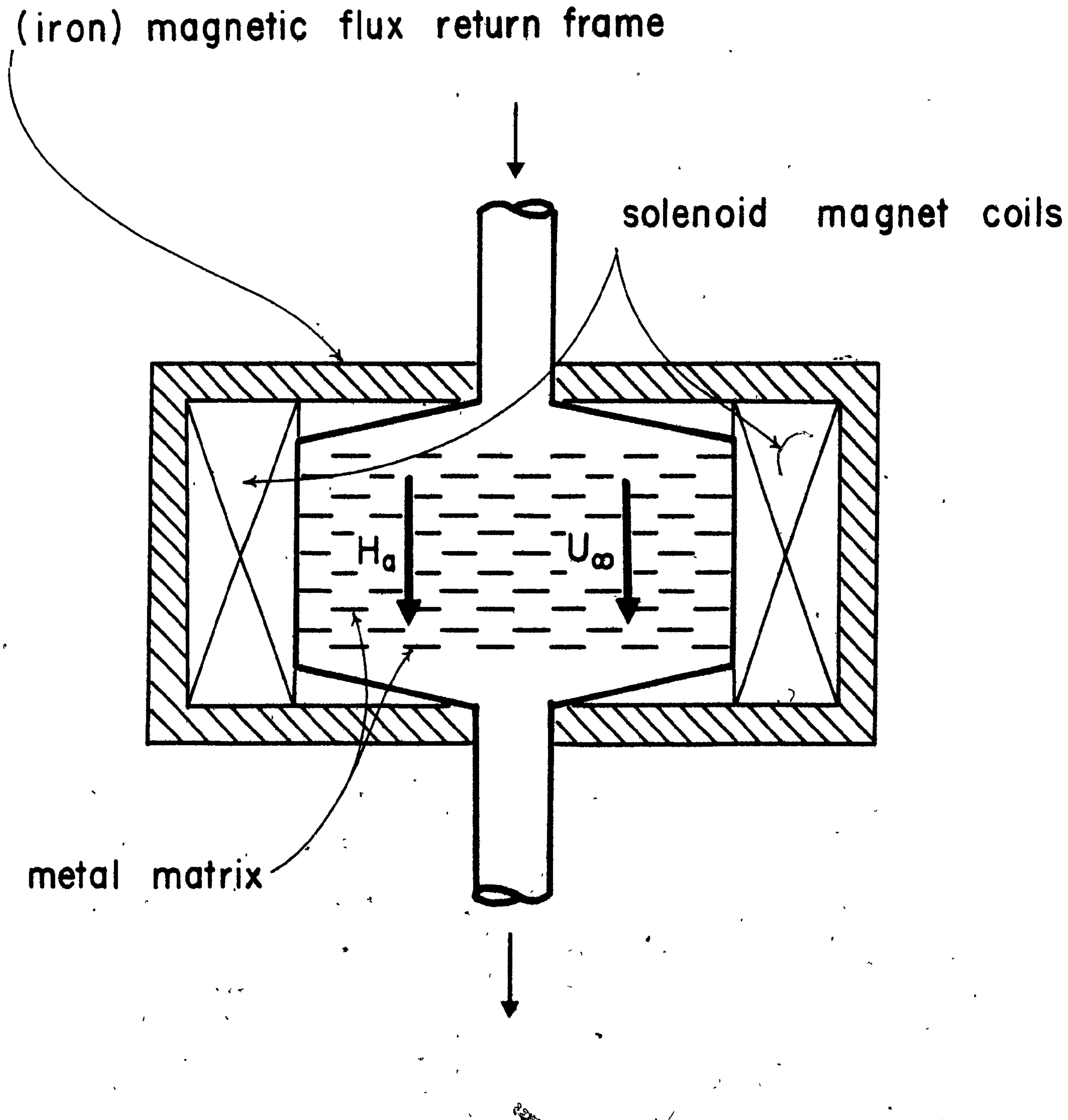

3-1 Iron clad solenoid design of hgms device.

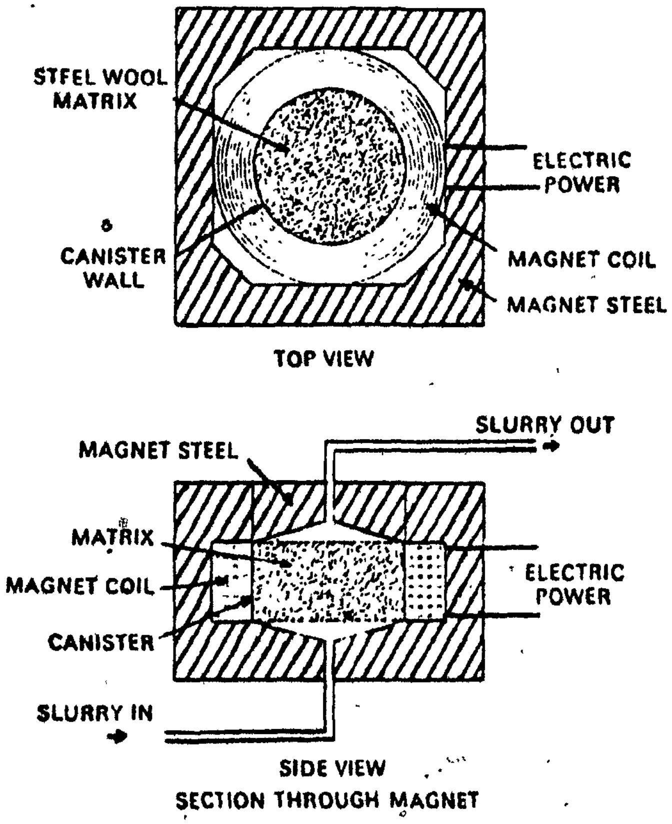

3-2 Schematic diagram of cyclic hgms.

portion of the solids is captured on the matrix. The trapped particles are then removed by switching off the magnet and flushing the matrix with wash water. The device therefore works in a cyclic manner of alternate feeding of slurry and removal of captured magnetics. As a filter, the slurry is fed to the matrix and the effluent monitored for solids content. Once the matrix approaches a fully loaded condition, solids will appear in the slurry effluent as "breakthrough" takes place. Again the magnet is switched off and captured material flushed from the matrix in a highly concentrated form. Batch devices are well suited to feeds where the fraction of magnetic material is small as this allows large volumes of slurry to be fed to the magnet before the matrix is loaded and flushing is required. In many mineral processing situations this is not the case and continuous hgms devices are required. A schematic representation of these separators is shown in Fig. (3-3). By ingenious design the matrix is mounted on a carousel and allowed to pass contінously through the magnetic field. The elongated solenoid still allows the production of a uniform magnetic field parallel to the slurry flow. Applications of this magnet to the iron ore industry and other high volume systems have been described. (79,80)

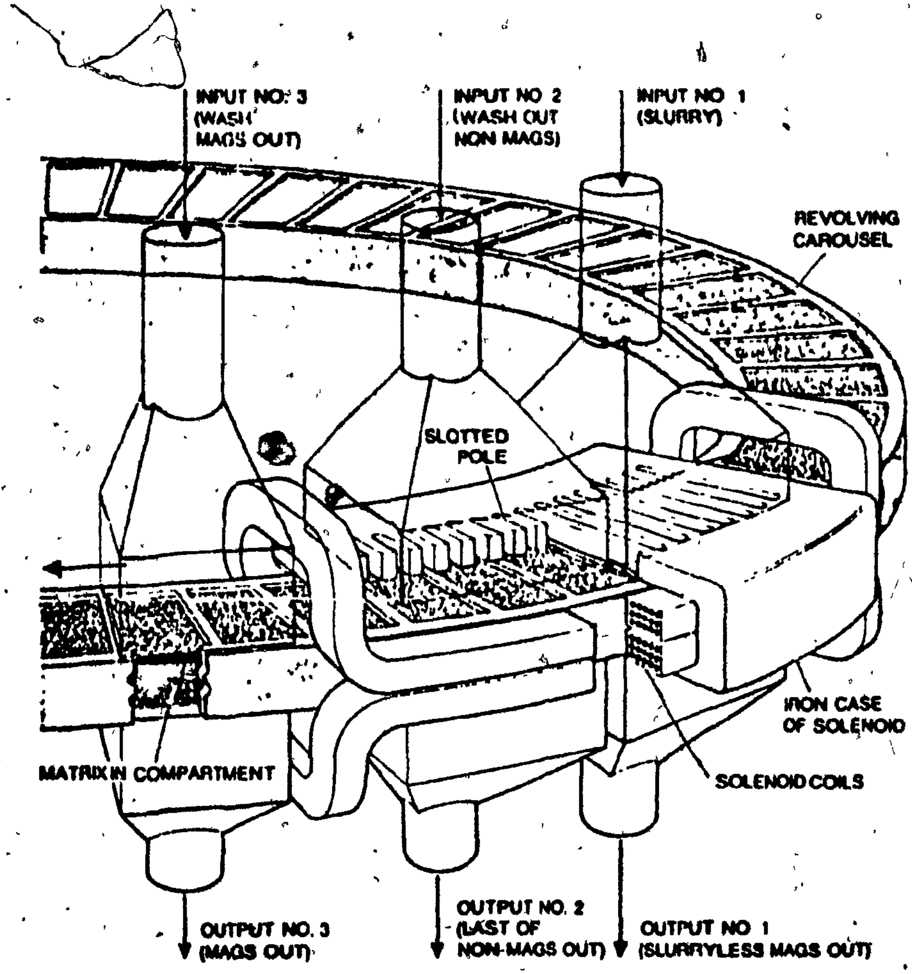

3-3 Schematic diagram of carousel hgms.

3.2. Models

3.2.1. Introduction

Accompanying the considerable effort in equipment design has been an extensive development of mathematical models. The techniques involved are a balancing of the well defined forces involved in the capture process i.e. magnetic, hydrodynamic and gravity forces. A simple idealized situation describing the separation process is presented in Fig. (3-4). A fluid moving at constant velocity contains a spherical paramagnetic particle. The particle approaches a cylindrical ferromagnetic wire with its axis at 90° to the flow. Application of a uniform magnetic field, applied perpendicular to the wire, magnetizes the wire. A field gradient is produced near the wire and consequently a magnetic force on the particle is developed. Providing the magnetic force on the particle is large enough to overcome the competing hydrodynamic drag and gravity forces, the particle will adhere to the wire. Magnetic force contours (Fig. 3-5) for an infinitely long ferromagnetic field, indicate the region of the wire over which attractive forces act on a small paramagnetic particle. The material build up can only take place on the top and

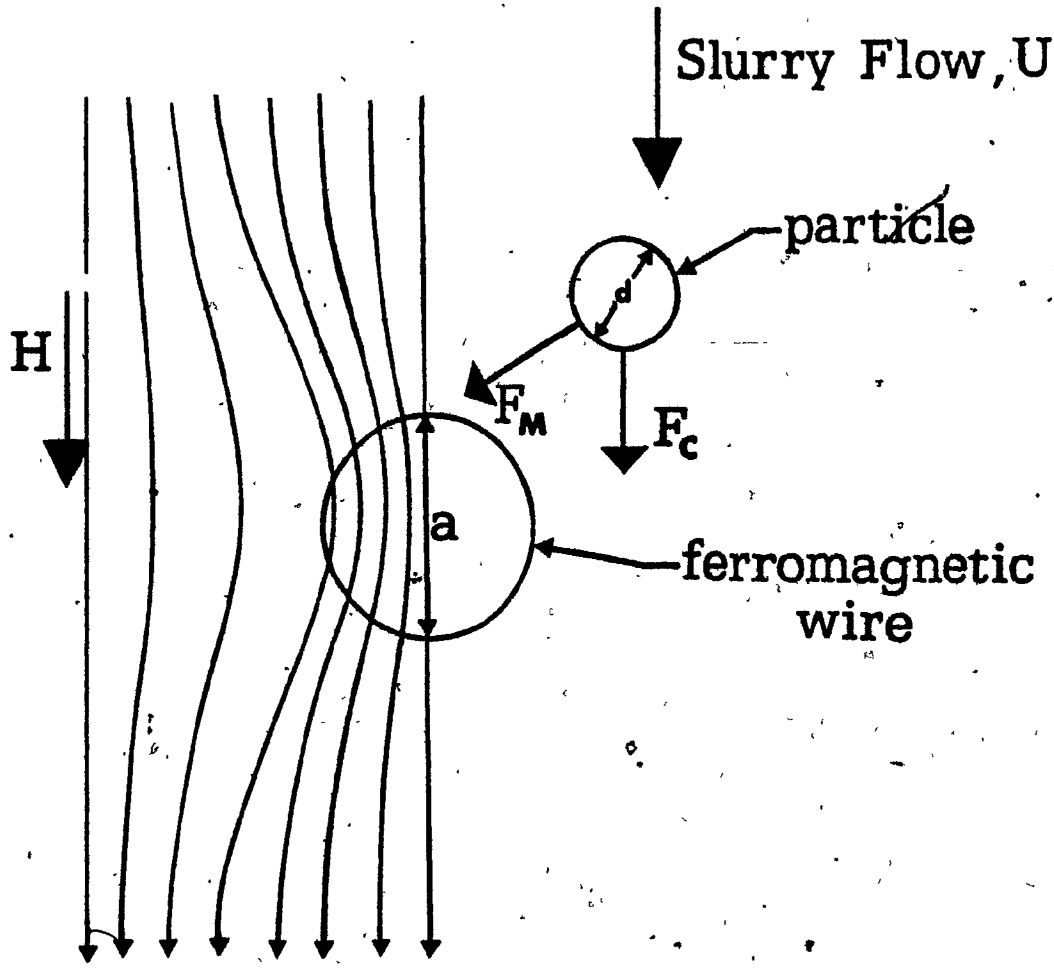

3-4 Simplified situation of spherical, paramagnetic particle approaching a cyclindrical, ferromagnetic wire in hgms.

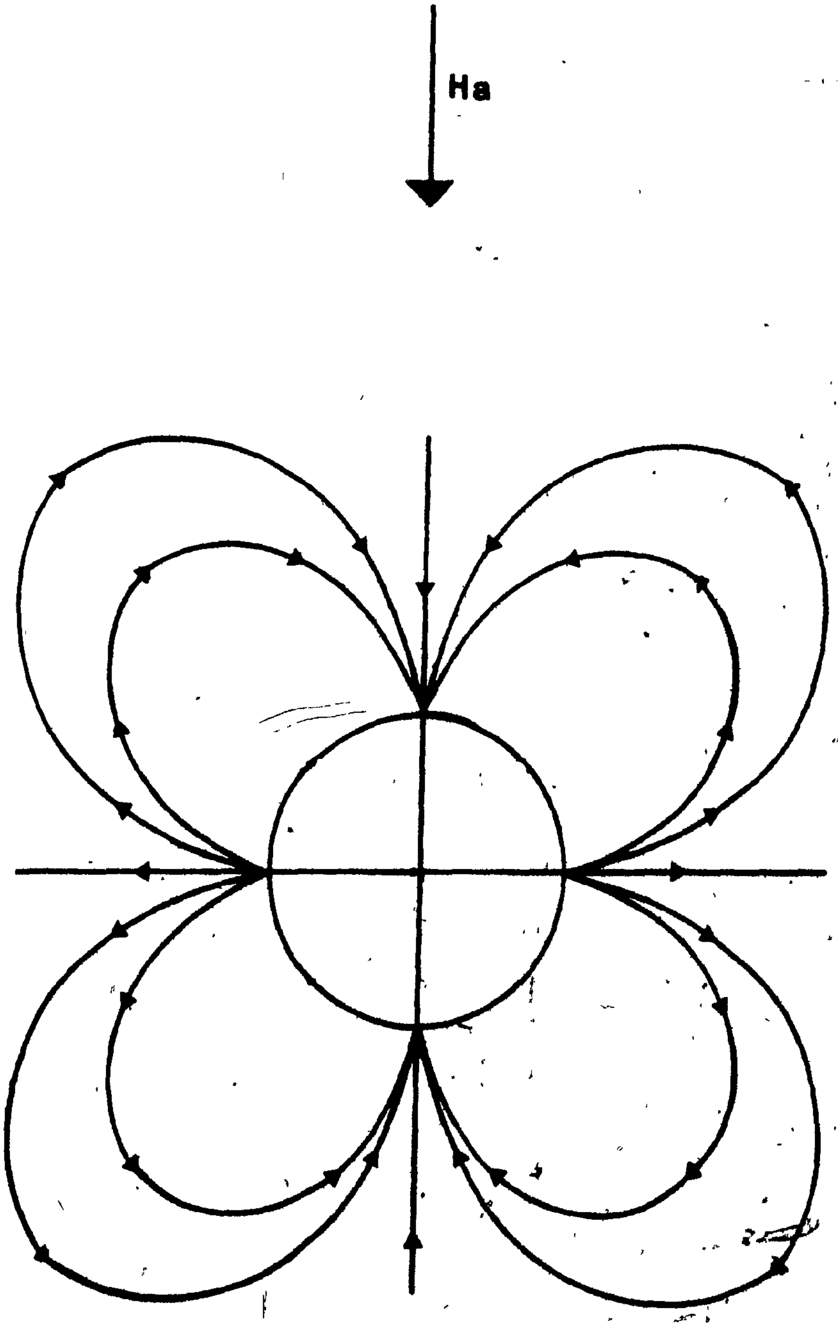

3-5 Magnetic force contours for an infinite ferromagnetic cylinder in a uniform field.

bottom of the wire.

Several approaches have been taken in describing the physics of the capture process. These may be broadly divided into the two areas of trajectory models and build up models. Trajectory models describe the motion of the magnetized particles under the influence of a magnetic force. The models predict a capture radius (R_c) which is the limiting radius or area about the wire from which all particles are captured. Build-up models, which assume particle capture on the magnetized wire has already taken place, attempt to predict the ultimate build up profile and mass of material on the wire. This approach allows simple predictions to be made of the total amount of material recoverable on the matrix. Attempts have also been made to describe the overall filtering performance of hgms systems by utilizing not only the above physical concepts but also by utilizing a "black box" approach. By applying the sorption theory of conventional filtering systems, predictions concerning magnetic filtering performance may be made.

3.2.2. Trajectory Models

Initial modelling studies centered on the trajectory model approach. In his original work Watson, (81) by considering magnetic and fluid drag effects only, found that trajectories of paramagnetic particles around highly magnetised ferromagnetic wires were dependent on the magnetic to fluid ratio $\frac{V_m}{U_\infty}$. The magnetic velocity V_m can be defined as the terminal velocity a spherical particle would achieve in a stationary fluid under a constant magnetic force and U_∞ the fluid velocity measured at an infinite distance from the wire. Assuming Stokesian drag, Watson derived:

$$V_m = \frac{8\pi b^2 \kappa H_a M_w}{9a\eta} \quad \text{(cgs units)} \qquad (3\text{-}1)$$

Where b is the particle radius, κ the volume susceptibility, H_a the applied background field, M_w the wire magnetisation, η the dynamic viscosity, and a the radius of the wire. To ensure magnetic capture the condition is $U_\infty < V_m$. The concept of a limiting particle trajectory is used in defining R_c the dimensionless capture radius. All particles passing within a capture cross-section $2R_c a$, will be attracted towards and ultimately captured by the wire. The dependence of R_c on the ratio $\frac{V_m}{U_\infty}$ as deduced by Watson (81) is shown in Fig. (3-6).

An extension of this single wire study can be made to apply to the entire matrix length. Assuming an element

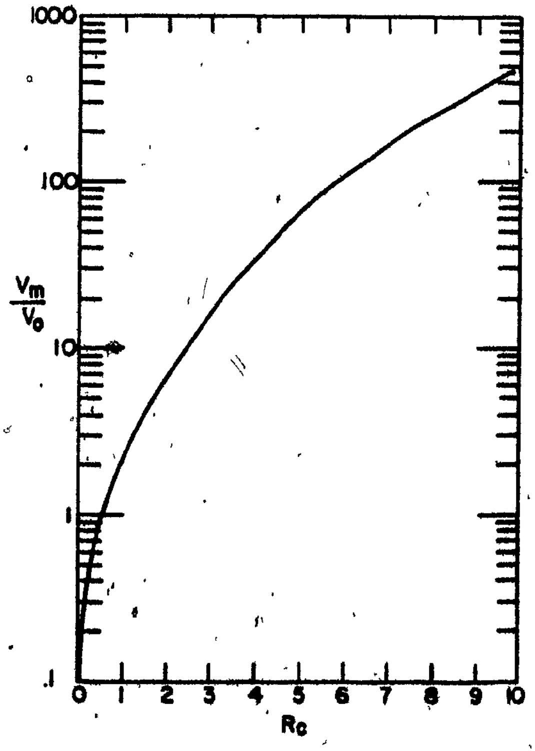

3-6 Watson's dependence of R_c on V_m/U_∞.

thickness ∂x of the matrix, a volumetric packing fraction F and matrix length L, then the ratio of particles leaving the separator to those entering may be expressed as:

$$\frac{N_0}{N_i} = \exp\left(-\frac{4}{3}\frac{FR_cL}{3\pi a}\right) \tag{3-2}$$

Luborsky and Drummond (82) considered a more realistic system where the effects of particle build up on the wire are taken into account. Assuming that 1/3 of ribbon-like fibres (the actual morphology of stainless steel wool) to be correctly oriented for fine particle capture, they deduced that:

$$\frac{N_0}{N_i} = \exp\left(-\frac{fFL}{3S}(R_c+\xi)\right) \tag{3-3}$$

Where S is the diameter of the major wire axis and f and ξ are data fitted parameters. The parameter f was termed the capture efficiency and ξ a capture radius for mechanical entrainment of particles.

Further development of this has been made by Clarkson, Kelland and King. (83) By applying a boundary layer condition on the solution for potential flow and elliptical fiber shapes, viscous and inertial fluid body forces are thus accounted for at low to moderate Reynolds numbers. The model also allows for non magnetically saturated wires together with gravitational and near field magnetic effects. Expressed in terms of recovery they gave:

$$\%R = 100 \left\{ 1 - \exp \frac{(-2K_f F R_c L)}{\pi a'b'} \right\} \qquad (3-4)$$

K_f allows for random fibre-fibre interactions and is analogous to the f factor of Luborsky and Drummond. The cross sectional area of this fibre is defined as $\pi a'b'$, where a',b' are the minor and major axes of the ribbon-like fibres. Experimental testing of the equation by Clarkson et al (84) found that a good correlation exists between the predicted recoveries and those measured for $K_f \simeq 0.05$. Their assumption of potential flow appeared to be correct only for particle sizes > 5μm and that below this size the shielding effects of the boundary layer on particles from the otherwise large drag forces of potential flow become increasingly significant and should be included in the equation.

Simons, Lawson and Treat (85) assuming potential flow, included inertial effects, gravity and a near field magnetic force term in their study of the dynamics of particles approaching a cylindrical wire. They established a series of boundary conditions under which it was possible to neglect these effects in calculating R_c and concluded that the relationship developed between R_c and $\frac{V_m}{\mu_\infty}$ by Watson was adequate for most practical cases.

Recent studies on the trajectory approach (87,88,89,90) have been more concerned with the prediction of whether particle build-up takes place on top of the wire or whether back capture can take place. Although these models have tended to predict considerable back capture for single wire studies, (91,92) it appears that for closely packed matrices this effect is not important in predicting the total amount of material captured. (91)

3.2.3 Build-up Models

The ability of trajectory models to provide information as to the initial capture cross-section for a specified set of conditions has been demonstrated by the models of Watson (81) and Luborsky et al. (82) Build-up models predict the profile of the accumulating material.

This is of concern in the trajectory models as the profile will influence the fluid flow. The second function of the build-up model is to determine the loading capacity of a wire and consequently the total mass recovery potential of the hgms device. The initial work of Luborsky and Drummond in determining the effect of the build-up profiles on particle trajectories was based on arbitrarily chosen build-up shapes. (82) Later work (93) considered the stability of these profiles by balancing the fluid drag and magnetic forces in the boundary layer existing over the build-up profile. The fluid forces were simplified by considering an average boundary layer and Stokesian drag on a sphere. The critical angles where the components of tangential force on the particles are exactly balanced can be calculated for each successive layer of particles, while the loci of these angles describe the ultimate build-up profile. The model tends to describe a fan-shaped build-up. Further work by Watson (90,94,95) supports the model of Luborsky and Drummond. Although still allowing R_c to be dependent on $\frac{V_m}{U_\infty}$, Watson applied a boundary layer adjustment and calculated the probability of retention in each surface element above the wire. This produced a build-up profile similar to that of Luborsky and Drummond. An effective R_c can be calculated which decreases as particle build-up takes place on the wire such that for volume of build-up V and wire volume V_w:

$$R_{c(eff)} = \frac{R_{c\ initial}}{\left(1 + \frac{4V}{V_w}\right)} \qquad (3\text{-}5)$$

Photographic evidence of fan shaped build-up has been established by Friedlander et al (96) and Hollingworth. (91) They support the assumptions of Luborsky and Watson.

The model of Liu et al (97) again similar in construction to that of Luborsky et al, found that a build-up volume maximum was reached prior to large reductions in R_c. Two cases were defined for particle-wire size ratios (i) $\frac{b}{a} = 1$ (ii) $\frac{b}{a} \ll 1$ where b is the particle radius and a the wire radius. For the larger particles (case i) Stokesian drag is assumed and the relationship between maximum relative build-up volume $f_{(max)}$ and $\frac{V_m}{U_\infty}$ is such that:

$$f_{(max)} \propto \left|\frac{V_m}{U_\infty}\right| \qquad (3\text{-}6)$$

For case (ii) an averaged boundary layer is applied to the system such that,

$$f_{(max)} \propto \left\{\frac{V_m}{U_\infty}\right\}^{0.8} \quad \text{and} \quad \left\{\frac{\delta}{b}\right\}^{0.8} \qquad (3\text{-}7)$$

where δ is the boundary layer thickness. An overall filter model was then developed for the condition b/a close to unity. They concluded that capture radii variations with build-up volume could be neglected since the capability of the wire matrix to capture particles remained high and practically unchanged up to build-up saturation. A function $F(V_m)$ can be described for the cumulative weight fraction of feed with magnetic velocity less than V_m by considering the magnetic velocity distribution of the feed stream. Thus 1-F (V_m minimum) corresponds to the fraction captured when subjected to the condition that all particles with V_m greater than V_m minimum are retained in the filter. This V_m minimum is specified by Fig. (3-7), the equilibrium wire loading. By integrating numerically (1-F(V_m minimum)) for increments of feed, the total weight fraction recovered by the separator is determined.

The model of Nesset and Finch (98) employs a force balance approach for particles that have arrived at the

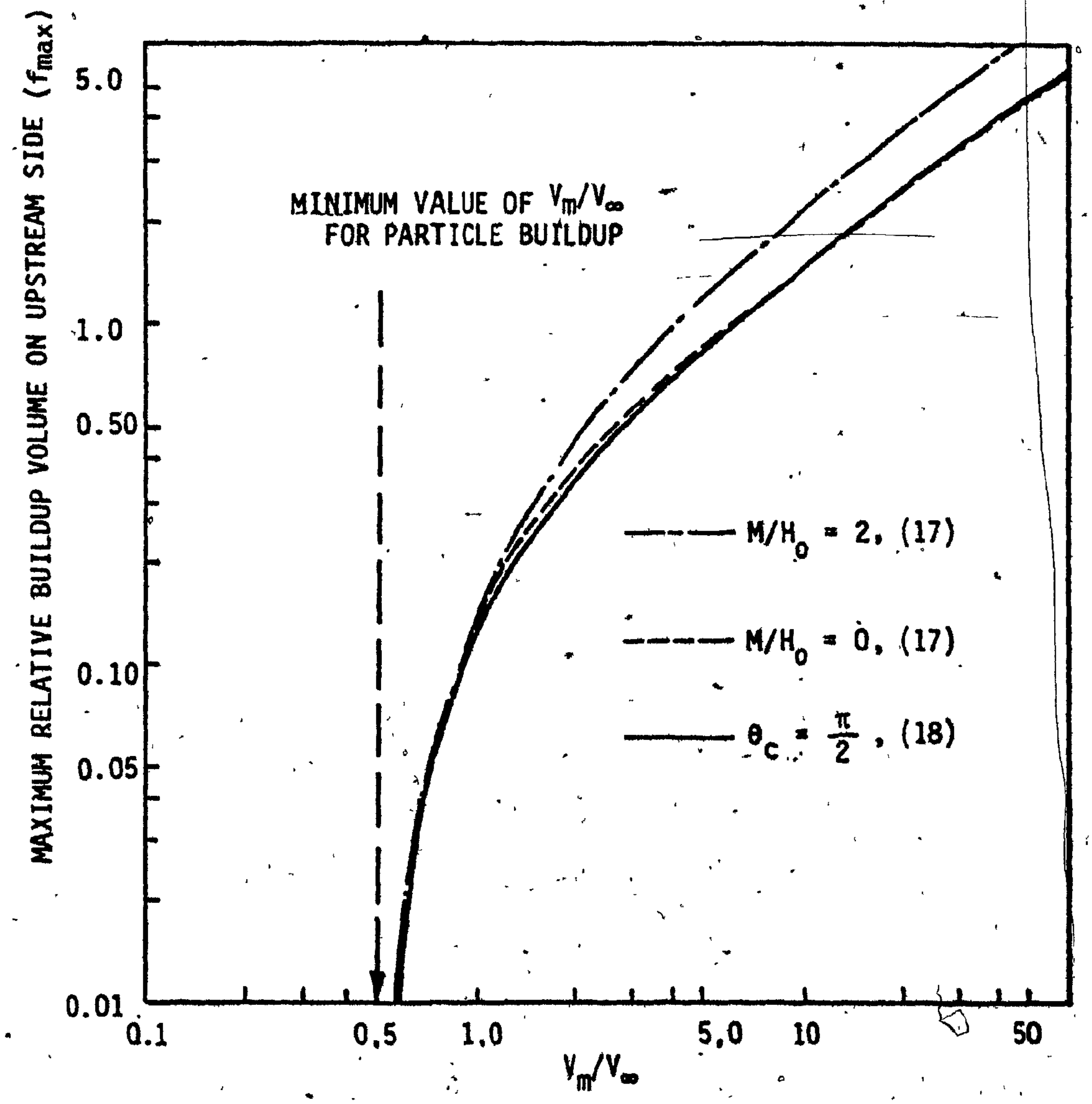

3-7 Liu et al maximum relative build up volume (f max) as a function of V_m/U_∞.

wire surface. By employing a layer by layer calculation, build-up profiles can be determined and recovery equations deduced. In defining fluid drag on captured particles a different approach to the traditional Stokesian drag was taken. The Blasius (99) solution was employed to describe the fluid drag on particles resting on the bottom of the developed boundary layer. The model also incorporates field perturbation terms for non saturated matrix wires as well as magnetic susceptibility functions for non paramagnetic materials.

Fig. (3-8) indicates the forces acting on a stationary particle arrived at the wire surface. The net radial force is comprised of magnetic and gravity terms, while the net tangential force is the sum of magnetic, gravity and fluid terms. A loci of critical angles Θ_c can be determined which define the region of particle attraction around the wire (Fig. 3-9). The predicted build-up shapes are in good agreement with the photographic evidence of Friedlander et al. (96) The build-up radius is determined from the force balance:

$$0 = -4/3\pi b^3 H_a^2 \kappa A \, \frac{a^2}{r^3} \sin 2\Theta \qquad \text{magnetic term}$$

$$+ \frac{2\pi b^2 \rho_f U_\infty^{3/2} \nu^{1/2}}{r^{1/2}} \{B\} \, f_b \qquad \text{fluid term} \qquad (3\text{-}8)$$

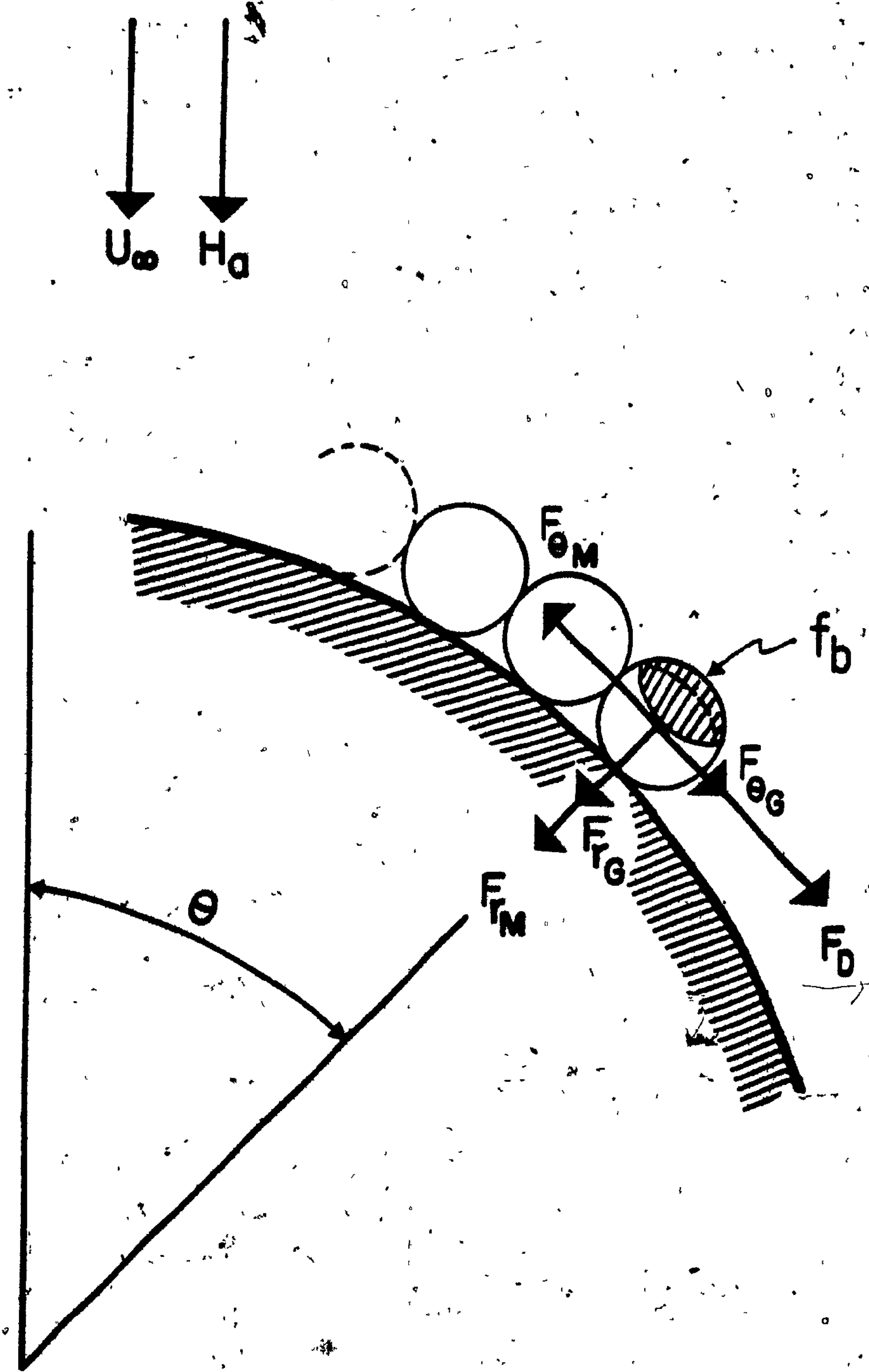

3-8 Force component acting on a spherical (101) particle at rest on a cylinder wall.

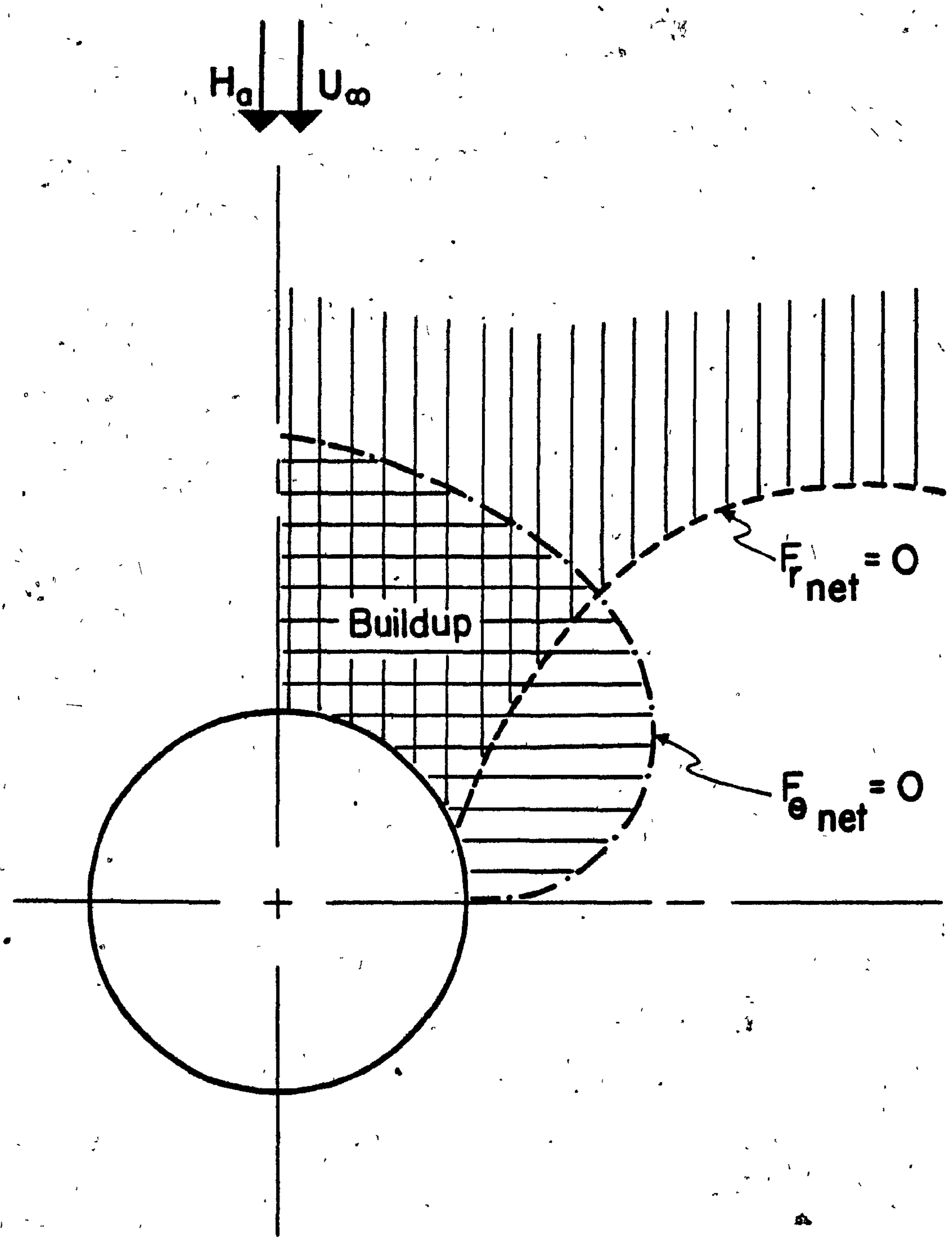

3-9 Loci of net radial and tangertial forces (101) in one quadrant about a wire. Hatched areas show negative net force.

where r is the particle accumulation radius, Θ is the angle from the front stagnation point on the wire ρ_f the fluid density, ν the fluid viscosity, B the Blasius term and f_b is the fractional area of shear on a particle. The term f_b was estimated at $\pi/8$ (121) and B was calculated to be 4.24. (100) The above equations can be reduced to a dimensionless form for describing relative build-up radius (r/a) or r_a. The equations are solved at $\Theta = 45^0$ a close approximation of the maximum angle of build-up:

$$r_a^2 = \left\{ \frac{2bH_a^2 \kappa A}{P_f U_\infty \nu^{\frac{1}{2}} a^{\frac{1}{2}}} \frac{1}{C} \right\}^{4/5} \tag{3-9}$$

$$= \left\{ \frac{N_L}{C} \right\}^{4/5} \tag{3-10}$$

where $C = 3/2 \; \{B\} \; f_b = 2.5$

N_L is called the "Loading Number", and represents the ratio of fluid shear forces to magnetic forces in equilibrium at a fully loaded build-up radius r_a. Having assumed a total build-up profile to be that of a 90^0 segment of radius r_a and introducing a packing density term ε, equations estimating volumetric and mass loading on the matrix can be derived.

The volume of captured material per unit volume of wire, γ_v is :

$$\gamma_v = \frac{\varepsilon}{4} \left(r_a^{\ 2} - 1 \right)$$

$$\gamma_v = \frac{\varepsilon}{4} \left[\left(\frac{N_L}{2.5} \right)^{4/5} - 1 \right] \qquad (3\text{-}11)$$

and γ_m, the mass of retained material per unit mass of wire is expressed as:

$$\gamma_m = \frac{\varepsilon}{4} \left[\left(\frac{N_L}{2.5} \right)^{4/5} - 1 \right] \frac{\rho_p}{\rho_w} \qquad (3\text{-}12)$$

Where ρ_p is the particle density and ρ_w is the wire density. A simple recovery equation permits the actual matrix loading to be compared with the full load where actual loading tends to be about 75% of the full;(101)

$$R\% = (0.75 \ \frac{\gamma_m}{L}) \ 100 \qquad (3\text{-}13)$$

L is the mass of magnetics in the feed. The dimensionless group N_L can be broken down into more recognizable dimensionless groups i.e.:

$$N_L = \left(\frac{9}{\sqrt{2}}\right)\left(\frac{a}{b}\right)\left(\frac{1}{Re_w}\right)^{0.5}\left(\frac{V_m}{U_\infty}\right)$$

Testing both Watson's $\frac{V_m}{U_\infty}$ ratio and N_L for predicting loading behaviour has shown that N_L appears to be more reliable. (100) Information concerning expected magnet operating parameters and separator performance can also be directly predicted from this dimensionless group.

Information on the behaviour of a matrix as a filter may also be determined from the model. By incrementally increasing feed weights to the matrix; recovery of material may be monitored as a function of time. Recoveries will decrease as feed weight increases until saturation of the matrix occurs. Filtering breakthrough curves can consequently be predicted as functions of uncaptured material versus time.

3.2.4 Filtration Breakthrough Models

A departure from these fundamental models of the capture process has been made by Akoto (102) and Collan et al (103,104,105) in order to describe the breakthrough characteristics of the magnetic separator when considered as a filter. These analyses are generally based on the sorption theory of fixed bed systems. Fig. (3-10) describes the general situation for an elemental segment of matrix ΔZ and area A. Akoto derives two equations for particle capture:

$$\frac{\partial c}{\partial t} + \frac{(1-\varepsilon_0)}{\varepsilon_0} \rho_m \frac{\partial n}{\partial t} + \frac{V_0}{\varepsilon_0} \frac{\partial c}{\partial z} = 0 \qquad (3\text{-}14)$$

$$\frac{\partial n}{\partial t} = K_d c \quad (1-n/n_T) \qquad (3\text{-}15)$$

Where c is the concentration of particles in the carrier fluid, ε_0 the initial void fraction of the matrix, ρ_m the density of matrix packing, n the mass of particles deposited per unit mass of packing, V_0 the superficial velocity of fluid through the matrix and n_T is the matrix loading of captured particles per fibre. Eqn. (3-14) is the conservation of material equation while Eqn. (3-15) is the rate equation where K_d is defined as a deposition coefficient:

$$K_d = \frac{2V_0\lambda_0}{\pi a \rho_m \varepsilon_0} \qquad (3\text{-}16)$$

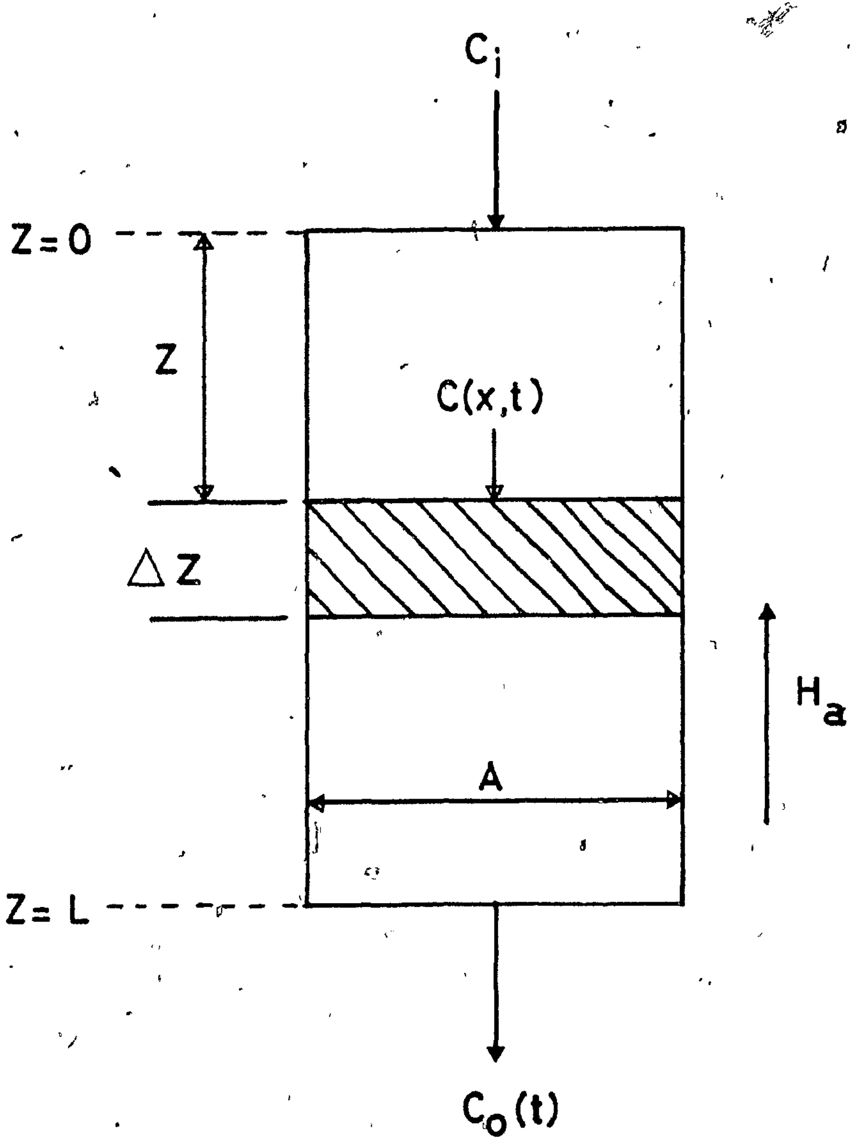

3-10 Akoto's hypothetical filter model.

Here λ_0 is the clean fibre capture cross-sectional area and a the fibre radius. In order to predict the form of actual breakthrough curves the conservation and rate equations are analytically solved, with appropriate conditions to yield two dimensionless quantities, ψ, the effluent concentration ratio and a throughput parameter T:

$$\psi(N,NT) = \frac{1}{1+e^{-N(T-1)}-e^{-NT}} \qquad (3\text{-}17)$$

Where N is a function of the deposition rate:

$$N = \frac{2\lambda_0(1-\varepsilon_0)L}{\pi a\varepsilon_0} \qquad (3\text{-}18)$$

and,

$$T = \frac{FT}{F_0}$$

Where F is the mass flow rate of solids, T is the elapsed time since the initial arrival of the fluid front at the bed exit and $F_0 = \rho_m n_T A(1-\varepsilon_0)$, the matrix loading coefficient.

Eqn. (3-17) can now be used to draw theoretical breakthrough curves Fig. (3-11) for various fixed bed lengths. as well as estimate the mass of captured material represented by the area bounded by each curve.

As a "black-box" approach to breakthrough curve prediction, the model is limited as a number of parameter estimates are required while the linear relationship imposed on the initial rate expressions may restrict the general applicability of the model.

Collan et al in a series of papers (103,104,105) have provided another empirical approach to simulating filter behaviour and have described a simple method. of magnet sizing for filtration systems. The analysis is dependent on describing an absorption length function ℓ such that $\ell=\ell(C_{abs})$ where C_{abs} is the mass concentration of the absorbed particles in the filter. Two sets of differential equations are defined in the description of the filtration process. (104)

$$\partial C_{abs}(x,\tau)\,\partial T = -V_0 \partial c(x,\tau)\,\partial x \qquad (3\text{-}19)$$

$$\partial C(x,\tau)\,\partial x = -\alpha(x,\tau)\,C(x,\tau) \qquad (3\text{-}20)$$

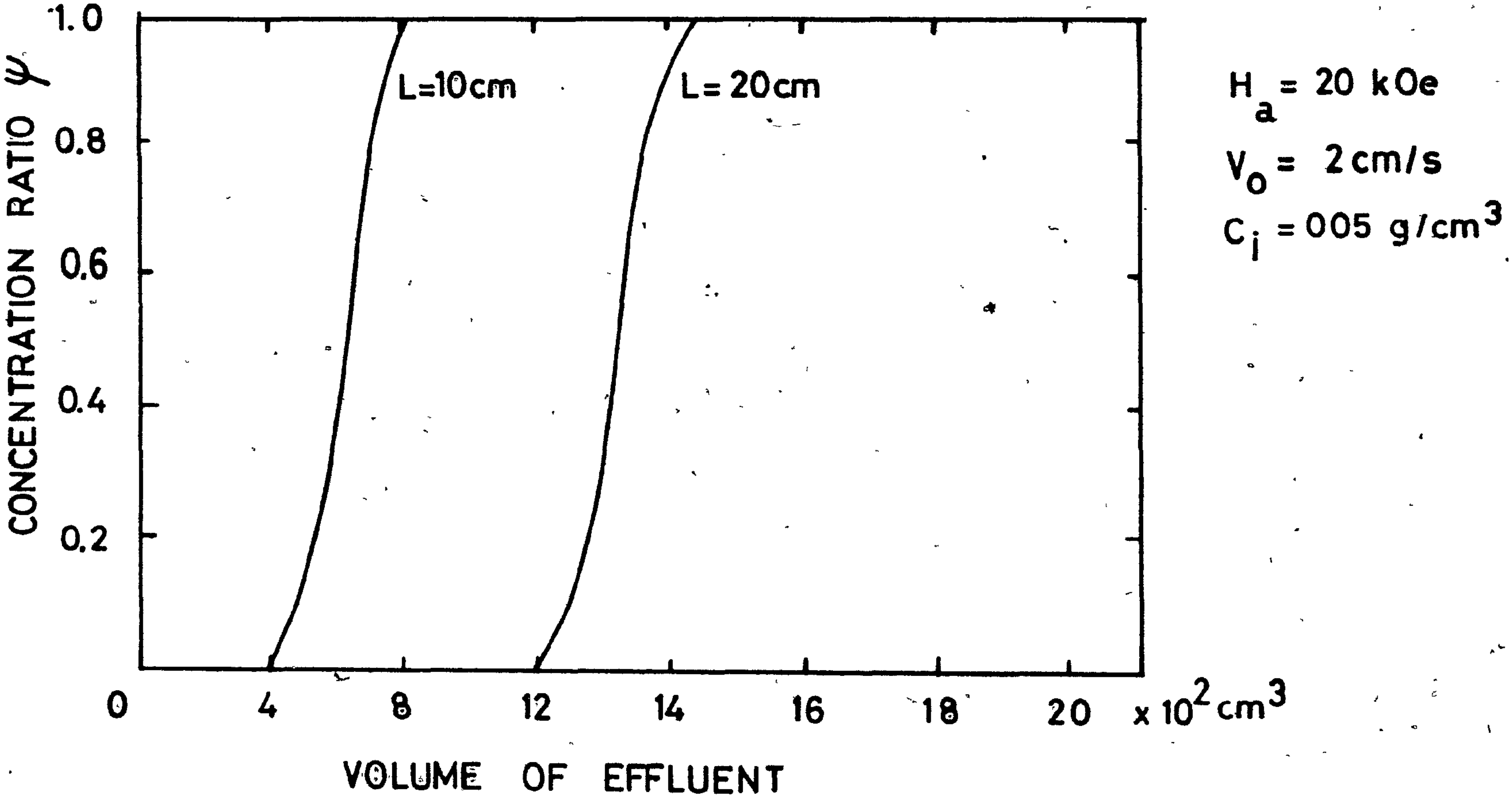

3-11 Akoto's sample of breakthrough curve.

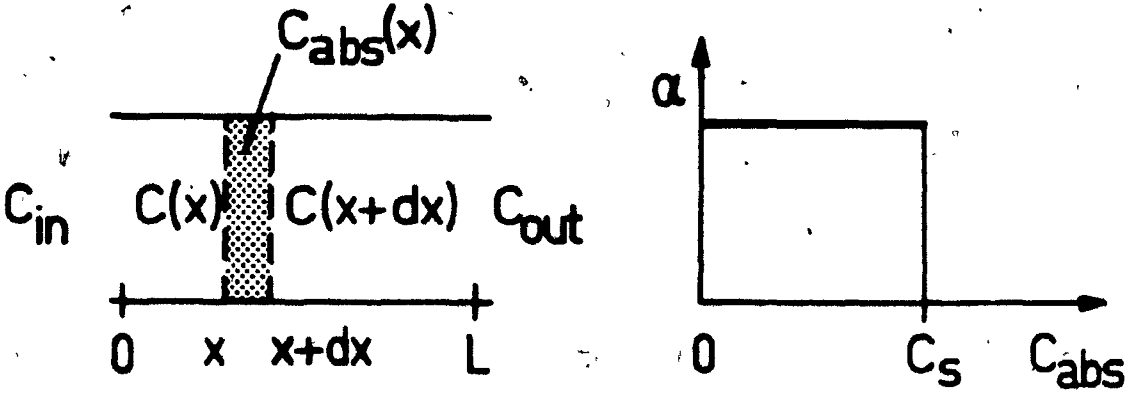

3-12 Diagram of filter parameters for the Collan model.

Where x is the distance along the filter from the inlet, C the concentration of solids in the slurry, $\tau = t - xA/V_0A(F)$, the filter time. The function A(F) describes the free cross-sectional area of the filter, A the filter area and v_0 the linear flow velocity. The expression $\alpha(x,\tau)$ is the absorption probability/unit length and is consequently the inverse of the characteristic absorption length ℓ.

A simple expression is assumed in order to describe the absorption length function ℓ:

$$\ell = \ell_0/(1 - \frac{C_{abs}}{C_s})^Y$$

Where ℓ_0 is the absorption length of a clean matrix and C_s is the saturation concentration or a maximum value of C_{abs}. The constant y is a data fitted parameter and experimentally it has been found that $1<y<2$. By inverting the procedure that allows modelling of the breakthrough curve, the filtration characteristics of a matrix may be obtained. Fig. (3-13) shows the form these curves take in describing the absorption length ℓ of a matrix of depth L as a function of the throughput velocity, all other parameters being constant. A considerably simplified approach to the analysis can be made by

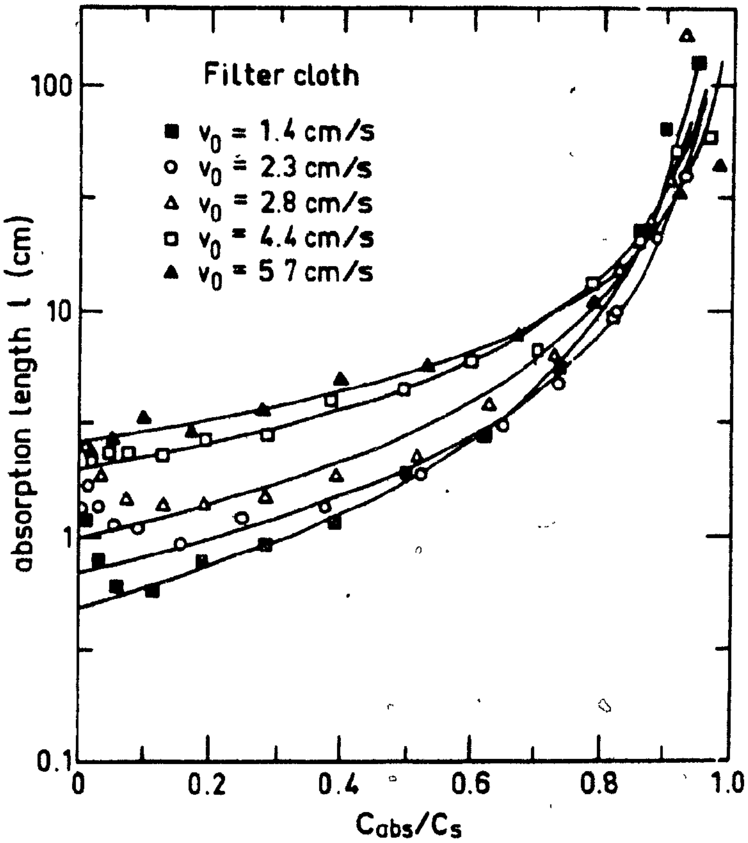

3-13 Sample of inversion of breakthrough curve from Collan et al.(21)

assuming y=1 in equation (3-21). The equations defining the filtration process can now be analytically (106) solved to give a generalized solution to the mathematical description of the breakthrough curves such that:

$$C_{out} = \frac{C_{in}}{e^{-K(t/t_0-1)}+1} \qquad (3\text{-}21)$$

$$C_{abs,\ out}(t) = \frac{C_s(1-e^{-V_s t/\ell_0})}{e^{-K\{t/t_0-1\}}+1} \qquad (3\text{-}22)$$

Where C_{out} is the output concentration of solids in the effluent, C_{in} the input concentration, $K \simeq L/\ell_0$ and $t_0 \simeq \frac{LC_s}{v_0 C_{in}}$. From experimentally determined breakthrough curves values for ℓ_0, t_0 and K may be determined by plotting a revised form of Eqn. (3-21):

$$\ln \left\{\frac{C_{in}}{C_{out}}\right\} - 1 = -\frac{Kt}{t_0} + K$$

Filter dimensions for an industrial process can be simply estimated from the equation:

$$A = \frac{Q}{V_0}\left(1+\frac{t_w}{t_f}\right) \qquad (3\text{-}23)$$

Where A is the filter area, Q the volumetric flow rate and v_0 the linear processing rate. The parameter t_f is the filtration time required before effluent solids concentrations reach a predetermined level, and t_w is the time required for magnet flushing. The function t_f can be described by equation (3-21) such that:

$$t_f = t_0 \left[1 - \frac{1}{K'} \log \left(C_{in}/C_{max} - 1\right)\right] \qquad (3\text{-}24)$$

Where C_{max} is the maximum output concentration allowable. From experimentally determined breakthrough curves and employment of equations (2-21,23,24) magnet sizes for an industrial process may be calculated. This analysis is limited however, to the assumption that absorption length is described as in equation (3-21) with y=1. The importance of whether y=1 or not can be tested by analysis of the data of Collan.$^{(105)}$ Fig. (3-14) denotes the sizing curves for (a) y=2 as experimentally determined by Collan and (b) y=1, for two processing flow rates. As magnet length encreases, the importance of the value of y considerably diminishes and at commercial magnet sizes this difference would be considered negligible. It would appear that for an initial sizing calculation the assumption y=1, which greatly simplifies the data fitting

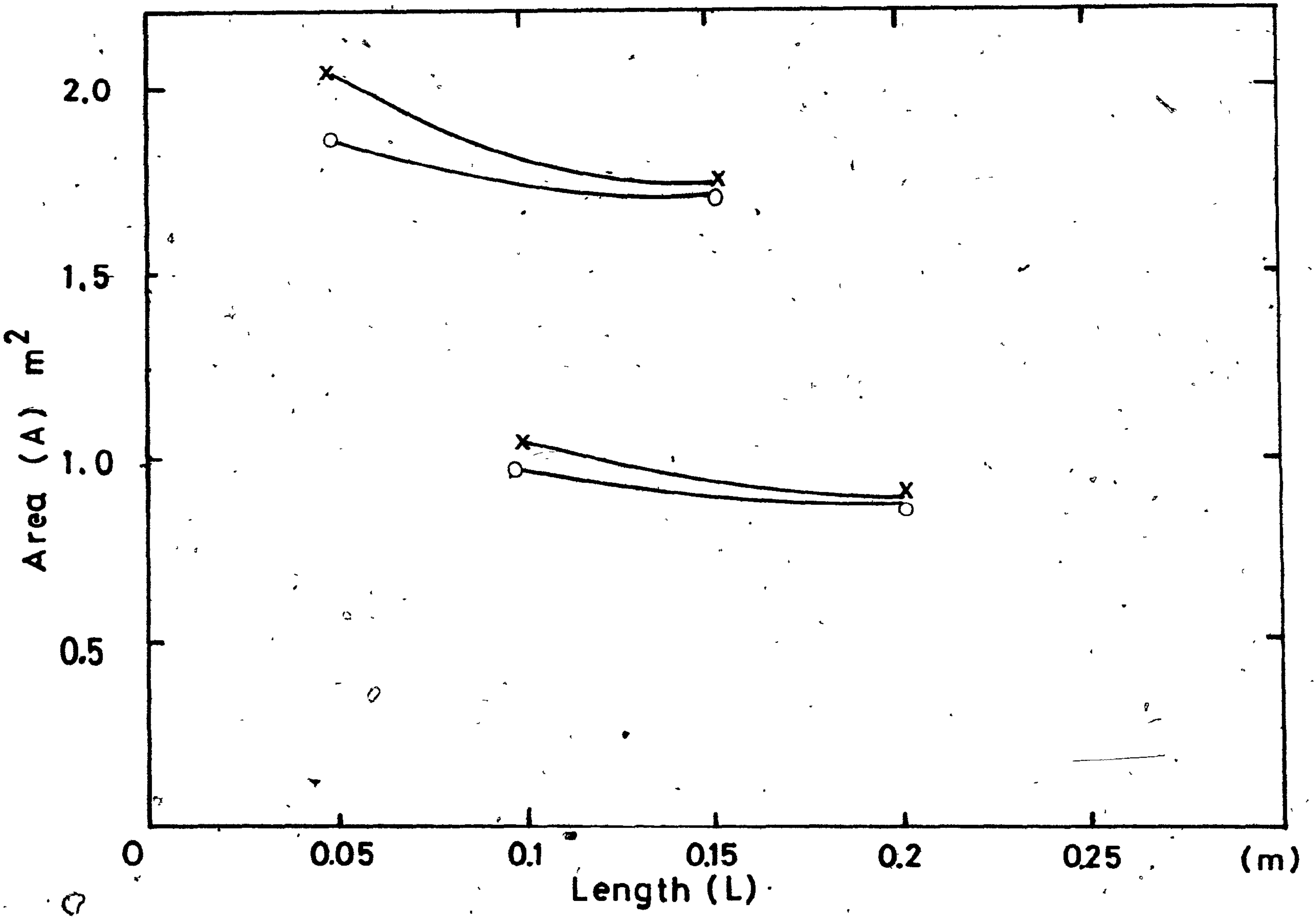

3-14 Collan approach to magnet sizing for waste water filtration system (x) y=z (o) y=1.

required, can be confidently employed.

The ability to predict industrial filter size from laboratory test results is obviously of considerable value. Whether this may eventually be more accurately achieved from fundamental models (e.g. Watson, Nesset and Finch), rather than the "black-box" approach of the above filtration models, has yet to be determined.

IV. EXPERIMENTAL PROCEDURE

4.1 Solids Preparation

In order to study the properties of the iron precipitates found in the zinc industry, each of the solid Fe compounds were synthetically produced following established chemical procedures.(44,55,60,63,77) In all cases, reagent grade chemicals were used.

4.1.1. Jarosites

Potassium, sodium and ammonium jarosites were prepared by heating separate solutions containing 15g/L Fe^{3+} as sulphate together with above stoichiometric additions of the appropriate alkali ion. An addition of 0.01M H_2SO_4 to all solutions prevented the hydrolysis of iron and premature precipitation as hydroxide. Sodium and ammonium ions were added as sulphate, while potassium ion was added as nitrate. The latter practice as well as the above stoichiometric alkali ion addition is felt to produce a product which is rich in alkali ion while limiting the co-precipitation of hydronium jarosite phases.(55) All precipitations took place in a 4L stainless steel reaction vessel. The solutions were heated in air to a temperature of 95°C and a pH of 1.5-2 was maintained during the reaction time of 5 hours. The solutions were vigorously stirred during the entire length of the reaction. After precipitation has been completed excess liquid was decanted and the precipitate filtered, washed and dried at 110°C. The dry product was then stored in a dessicator prior to analysis.

4.1.2 Goethites

In order to reproduce the VM and EZ industrial procedures and produce separate phases of both α and β FeOOH, the precipitation techniques of Davey and Scott (63) were followed. To reproduce the VM process a solution of 30g/L Fe^{++} as sulphate was oxidised by controlled addition of a 3% w/v H_2O_2 solution at a reaction temperature of 85°C and under vigorous stirring. The oxidant was metered into the reaction vessel at 30ml/hr by means of a peristaltic pump. This rate of addition allows a total reaction time of approximately 1hr/100mls of ferrous iron solution originally present. The pH of the mixed solution was maintained at 3.5 ± 0.2 by small additions of MgO powder. After precipitation was completed, the slurry was decanted, filtered and the precipitate dried. In reproducing the EZ process, the precipitation vessel was initially charged with a synthetic leach liquor (usually H_2O only) containing much less than 1g/L ferric iron. A solution containing 30g/L Fe^{3+} was then added by means of a dual channel peristaltic pump, at an initial rate of 2ml/minute. The pump was also used to discharge slurry at the same rate. This ensured the basic condition for goethite precipitation in that dissolved ferric iron levels in the precipitation vessel did not rise above 1g/L Fe^{3+}. During precipitation, solutions in the vessel were maintained at $80^{\circ}C$ and a pH of 3 ± 0.2, again by means of small additions of MgO powder. Reaction times were usually of several hours, depending on the volume of ferric iron solution added to the precipitation tank. The precipitation rate was increased by a factor of 1.5 to determine the change, if any, in precipitate properties. Ferric iron as both sulphate and chloride were tested in the same manner. Again after precipitation was complete the slurry was decanted, filtered and the precipitates dried for analysis.

4.1.3. Hematite

The production of a hematite precipitate was achieved by following the essential details of the Akita Zinc process.(60) Ferrous sulphate solution containing 30g/L Fe^{2+} was charged to a 2 litre titanium clad autoclave. The solution was then neutralised to pH 4.5 by a small lime addition. Hematite precipitation was allowed to take place by heating the solution to 200°C under $1.82 \times 10^7 Pa.O_2$ pressure together with vigorous stirring. A reaction time of 3 hours was sufficient to precipitate >90% of the iron as hematite. At the end of the precipitation the slurry was filtered, washed and dried.

4.1.4. Magnetite

A magnetite precipitate was produced by following the preferred procedure of Kunda and Hitesman.(77) A ferrous sulphate solution containing 30g/L Fe^{2+} was first neutralised with a solution of ammonium hydroxide of sufficient molarity to ensure a stoichiometric level (equation 2-13) for magnetite precipitation. The mixed solution was then charged to a 2 litre titanium clad autoclave and heated to 80°C under $1.72 \times 10^6 Pa.O_2$

pressure. A 15 minute reaction time was employed to precipitate >95% of the iron as magnetite. The final slurry was filtered, washed and dried for analysis.

4.1.5 Ferric Hydroxide

Ferric hydroxide slurries were prepared by allowing the simple hydrolysis of ferric sulphate solutions to take place. A 15g/L Fe^{3+} solution was neutralised with slow addition of a 1M NaOH solution until precipitation was complete. Due to the unstable nature of ferric hydroxide precipitates, the filtering and drying procedures were ignored and the slurry fed directly to the magnetic separator.

4.1.6 Canadian Electrolytic Zinc Jarosite (CEZ)

In order to compare the above "synthetically" produced precipitates to one that was formed industrially, quantities of an ammonium jarosite were collected from the CEZ Valleyfield Plant. The samples were collected in electrolyte, directly from the final jarosite precipitation tank and from the jarosite thickener overflow.

The collected jarosite slurry from the final precipitation tank was filtered from the electrolyte for analysis. Initial inspection of the filtered solids revealed two distinct phases. These consisted of a yellow jarosite phase and unreacted ferrite phases used for solution neutralisation. Ferrite phases were separated from the jarosite by reslurrying the solids and passing them through a Davis tube magnetic separator. The separated solids were then dried and kept for analysis.

4.2 Precipitate and Fluid Analysis

The ability to accurately identify the various iron phases produced from such a variety of chemical processes was achieved by utilizing a combination of analytical techniques.

4.2.1 Jarosites

(a) Synthetic jarosites

All synthetically produced jarosite type compounds were initially identified from X-ray diffraction patterns obtained using a Debye Scherrer camera, 114·6mm diameter and a Cr lamp. The patterns produced were compared to those found by Dutrizac and Kaiman (55) for the three jarosite phases of interest in the present study. Chemical analysis by atomic absorption using a Pye-Unicam SP190 spectrometer allowed determination of potassium, sodium and iron levels in the precipitates. Ammonium ion concentrations were determined by analysis of the total nitrogen content of the ammonium jarosite phase. (107)

(b) CEZ jarosite/electrolyte

The solid phases collected were initially identified using the X-ray diffraction techniques described above. The ferrite phase was then mounted in resin and polished for analysis using electron microprobe techniques.

Samples of electrolyte were analysed for dissolved zinc and iron contents by atomic absorption analysis.

4.2.2 Goethites

Identification of the goethite phase was achieved by a combination of X-ray diffraction and Differential Thermal Analysis. Diffraction patterns were obtained under the same conditions as those achieved for the jarosites. Identification of the precipitates was made by comparison to the standard references (108,109) for α and β FeOOH. Differential Thermal Analysis patterns of the precipitates were produced using a Fisher 260F DTA machine. These patterns were then compared to the general goethite patterns produced by Mackenzie,(110) and Davey and Scott.(63)

4.2.3 Hematite and Magnetite

Identification of hematite and magnetite phases was made using X-ray diffraction techniques as for jarosites and goethites. Diffraction patterns were compared to those of the ASTMS Powder Diffraction Index.(108)

4.3 Parameter Measurement

In order to implement mathematical models for describing the magnetic filtering process the measurement of several physical and magnetic parameters is required. Information concerning both the properties of the precipitates and the magnetic filter are required.

4.3.1 Particle Density

Density values for all precipitates were obtained using a Quantachrome Null Pyncometer. Experimentally determined densities were compared to theoretical or previously reported values. (55,11)

4.3.2 Precipitate Particle Size

The size distribution of each of the different materials was determined using an X-ray sedimentometer, the Micromeritics sedigraph 5000D. The device employs a finely collimated X-ray beam to measure the change with time of particle concentration in a sample cell. Analysis times are reduced by allowing the cell to descend relative to the X-ray beam. The size distribution is read from an x-y plotter which gives cumulative weight% finer than versus the equivalent Stokesian diameter. Particle sizes from 50 - 0.2μm can be determined. A 0.2% Calgonite in water solution and 15-20 minutes of stirring ensured complete dispersion of the particles prior to measurement. (The equivalent Stokesian diameters represent the size of a sphere which would settle at the same rate as the particle under observation.)

Scanning electron micrographs of all solids were made to investigate the morphology of the individual precipitate particles, as well as to confirm the general findings of the sedigraph tests.

4.3.3 Particle Magnetisation Measurements

4.3.3.1 Theory

Particle magnetisation measurements are a basic requirement in predicting the magnetic performance of a material. Considering the force F_x acting along a given direction on a particle placed in a magnetic field, then:

$$F_x = VM_p \frac{\partial H}{\partial x} \qquad (4\text{-}1)$$

Where V is the volume of the particle, M_p the particle magnetisation and $\frac{\partial H}{\partial x}$ the field gradient over the particle. Particle magnetisation M_p may be defined as:

$$M_p = \kappa H \qquad (4\text{-}2)$$

Where κ is the particle volume susceptibility and H the field strength. Equation 4-1 can now be rewritten:

$$F_x = V(\kappa_p - \kappa_m) H \frac{\partial H}{\partial X}$$

Where κ_m is the magnetic susceptibility of the medium. For air and water $\kappa_m \approx 0$ and is usually ignored.

The way in which particle magnetisation varies with field strength is a useful way to identify various types of magnetic materials. Fig. (4-1a,b,c) shows two linear responses as (a) magnetisation decreases with field strength and (b) magnetisation increases with field strength. Response (a) is termed diamagnetic

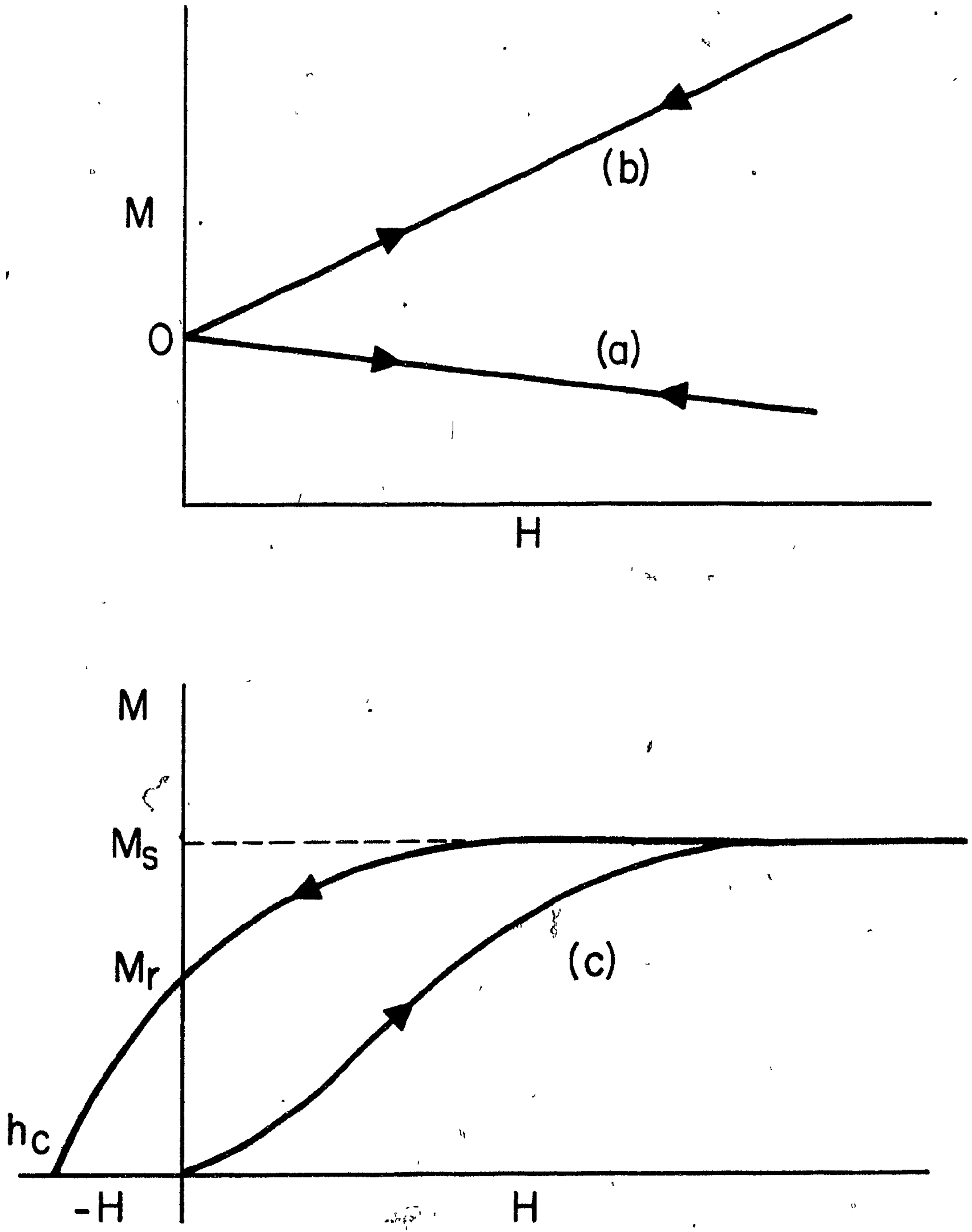

4-1 Magnetisation behaviour as a function of field for (a) diamagnetics, (b) paramagnetics or antiferromagnetics, (c) ferromagnetics or ferrimagnetics.

and susceptibility values are usually very small $< -10^{-6}$ emu/cm^{3}Oe. Response (b) is typical of either paramagnetic or antiferromagnetic materials. The value of the susceptibility is of the order of 10^{-5} emu/cm^{3}Oe. Curve (c) is typical of ferromagnetics or ferrimagnetic materials in that the response is non linear. The magnetisation rises rapidly with field strength to a saturation value M_s. The saturation magnetisation is reached with $H \approx 0$ and the material is said to have spontaneous magnetisation. The value of this magnetisation for ferromagnetics is the order of 10^3 emu/cm^3 at a field of only 1 Oe. Some compounds show a combination of both spontaneous magnetisation followed by a magnetisation increasing linearly with field strength. This effect of field dependent susceptibility may be due to ferromagnetic contamination of the paramagnetic or antiferromagnetic material, or it may be a true property of the material as in the case of α-Fe_2O_3.(112)

4.3.3.2 Measurement of Susceptibility

4.3.3.2(a) The Frantz Instrument

The Frantz Isodynamic separator, although better known for precise laboratory mineral separations, may be adapted for susceptibility determinations. The separations are made in a tray placed between the poles of a powerful electromagnet. A competition between gravity (F_g) and magnetic (F_m) forces exists on a particle travelling down the tray. (Fig. 4-2) The design of the pole pieces allows a constant force across the tray to be maintained on any paramagnetic particle by maintaining a constant value of $\frac{H\partial H}{\partial x}$. The two forces are defined as:

$$F_m = \kappa . v . H\frac{\partial H}{\partial x} \tag{4-3}$$

$$F_g = V . p . g . \sin\theta \tag{4-4}$$

and by equating 4-3,4 an expression for susceptibility is obtained such that:

$$\kappa = \frac{\rho g \sin\theta}{\frac{H\partial H}{\partial x}} \tag{4-5}$$

where θ is the side slope as defined by Hess. (113) By callibration against materials of known susceptibility

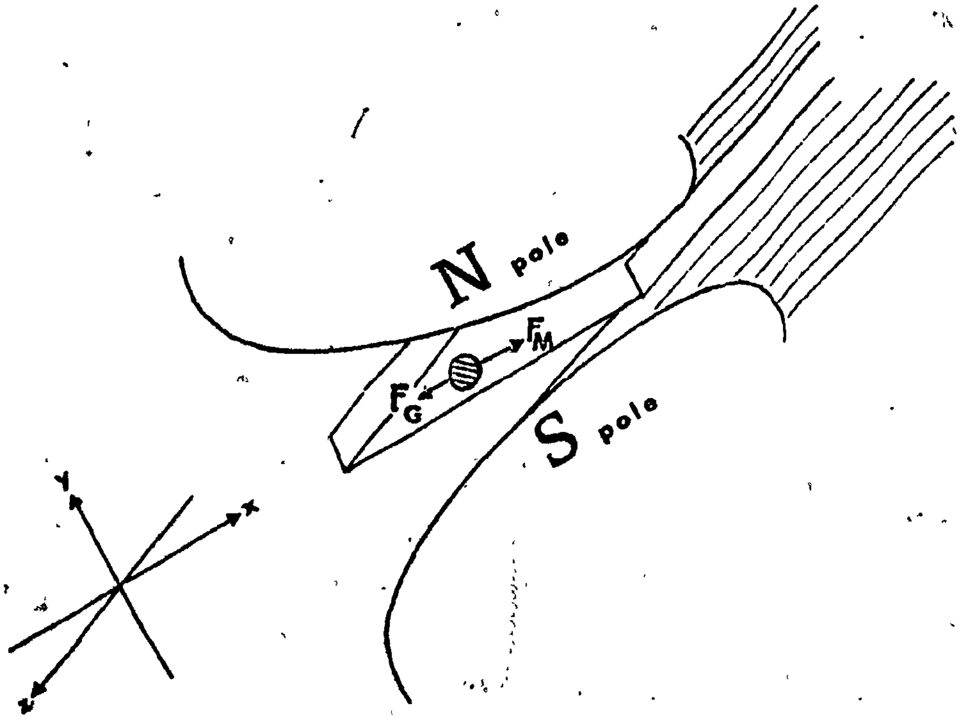

4-2 The dry Frantz force balance on a particle travelling between the isodynamic pole pieces.

McAndrew (116) deduced that:

$$\kappa = \frac{\rho.\sin\Theta.2.0\text{x}10^{-5}}{I_{50}^{2}} \qquad (4\text{-}6)$$

or in units of mass: $$\chi = \frac{\sin\Theta.2.0\text{x}10^{-5}}{I_{50}^{2}} \qquad (4\text{-}7)$$

Which is referred to also as the Hess equation. I_{50} is the current at which 50% of a single phase reports to the magnetics side of the tray. To obtain this value, the "magnetic profile" of the material is produced by passing the material through the separator and re-treating the non-mags fraction at higher currents. The side setting angle θ remains constant. The process is repeated until all the material reports as magnetics. Fig. (4-3) denotes the general shape of the profile and the point at which the I_{50} is read.

A more generalised form of equation (4-6) can be made to include a field dependent susceptibility of the form:

$$M_p = M_o + \kappa_\infty H$$

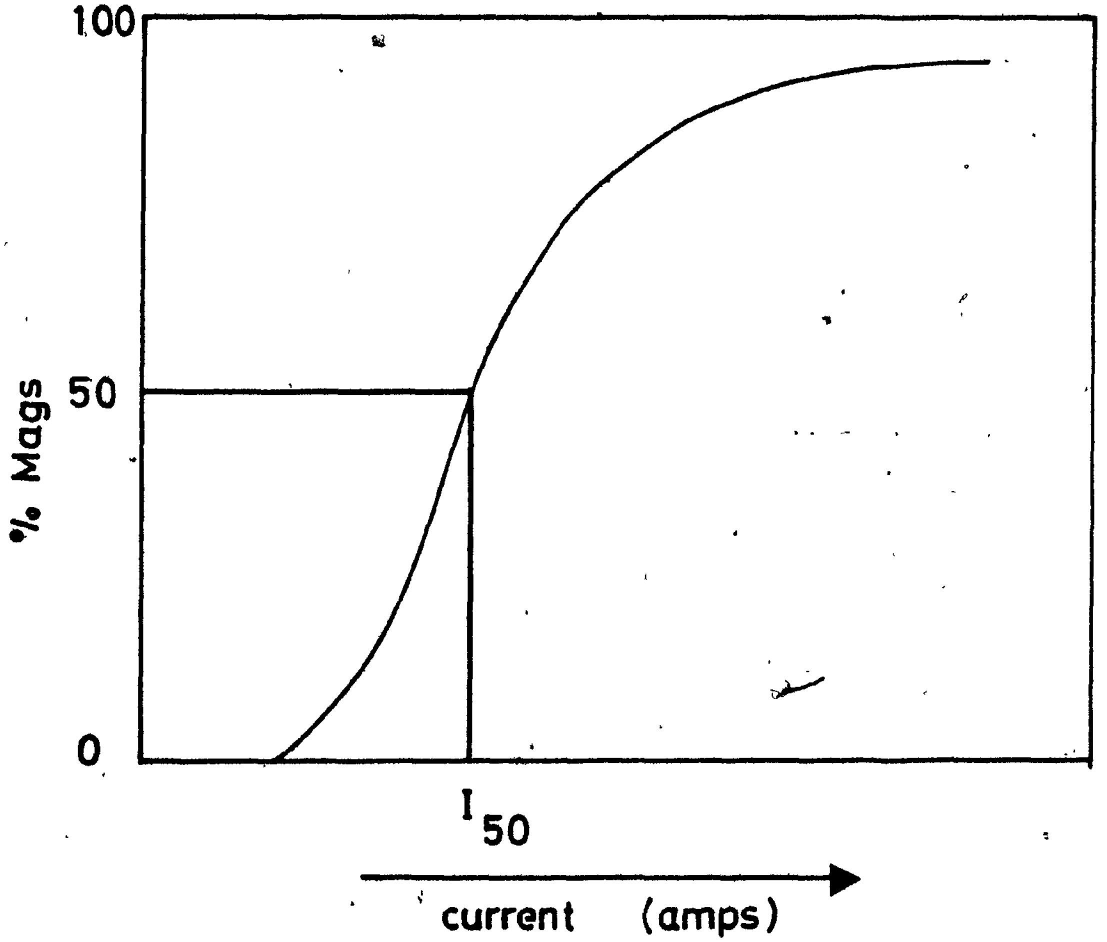

4-3 The magnetic profile of a paramagnetic material as deduced from Frantz data.

Where M_0 is the spontaneous magnetisation and κ_∞ the susceptibility measured at infinite field strength. These parameters are constants. Nesset and Finch (112) derived:

$$\sin\Theta = (4.65 \pm 0.14)\ \sigma_0\ I_{50} + (48.7 \pm 3.0)\ \times 10^3\ \chi_\infty\ I_{50} \qquad (4-8)$$

For measurements of spontaneous magnetisation σ_0 measured in units of mass susceptibility χ_∞ at infinite field strength. At the conditions of $\sigma_0=0$, $\chi_\infty=\chi$, equation (4-8) reverts to equation (4-7), the Hess equation.

The major limiting factor of the "Dry" Frantz magnetic separator is one of particle size. Particle sizes <25μm are very difficult to treat. Precipitate particles are very fine and for this reason a prototype "Wet" Frantz separator (115) was used for particle susceptibility determinations. The device allows the separation of materials while suspended in a liquid, and particle sizes much less than 25μm were reported to be easily treated in this system. (116) A second advantage is the ability to determine the effect of fluid susceptibility on the measurement of suspended solids. Fig. (4-4) denotes the general flow sheet of the

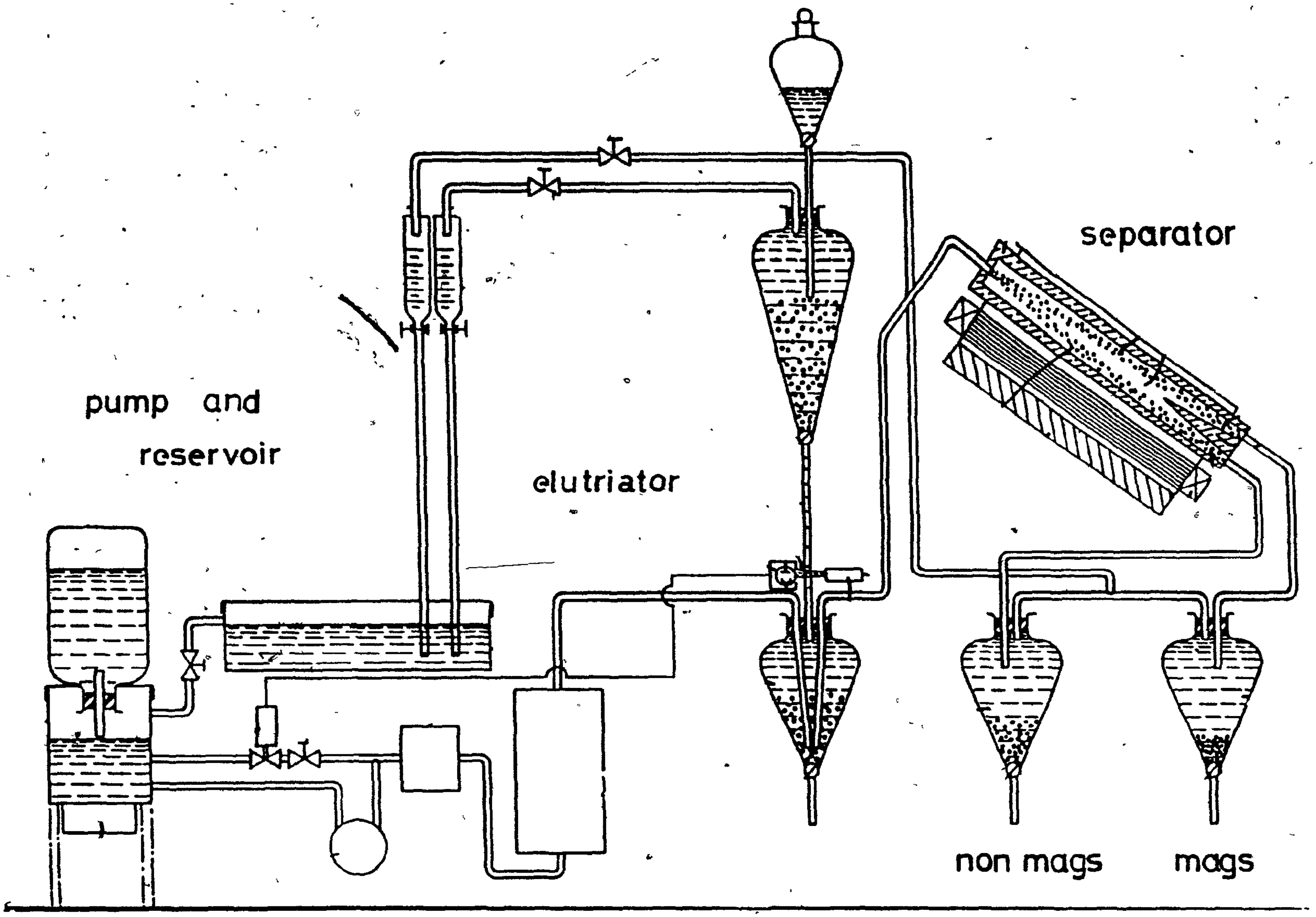

4-4 The "wet Frantz" system.

system. The basic problem of the technique lies in the treatment of different size particles of the same material which consequently have different settling rates. This problem is solved by separating particles into fractions having equal settling rates by elutriation and feeding the fractions directly from the elutriator, ina s liquid carrier, through the magnetic field of a Frantz Isodynamic separator. By adjusting the velocity of flow through the separator in proportion to the settling rate of the particles, the residence time of the particles in the magnetic field is proportional to the increased time required for settling.

The velocity vector diagram for two particles settling at the same rate, one which is magnetic, the other non magnetic is shown in Fig(4-5). The non magnetic particle sinks in a vertical direction with velocity V_G while it moves in an axial direction at the fluid velocity V_L. The final velocity V_{NM} thus has an angle ϕ from the axis of chute. By adjusting Θ and liquid velocity, the required angle ϕ is obtained such that non magnetic particles are deflected sufficiently to enter the non magnetics side of the chute divider.

A magnetic particle will be deflected by the combined gravitational velocity and the velocity achieved under the influence of the magnetic field. By adjusting the magnetic field, particles may be deflected by an angle ϕ to the magnetics side of the chute. The resulting speed of the magnetic particle is the same as the non magnetic particle but deviating in direction by an angle of 2ϕ. The speed of the magnetic particle relative to the liquid V_{G+M} is also the same as the settling velocity V_G of a non magnetic particle. The two particles deviate from each other by an angle 2Θ. By considering two particles of half the settling velocity and by halving the liquid velocity a new vector diagram is produced, denoted by the dotted lines of Fig. (4-5). The total angle of deflection remains the same while only the time taken to reach the divider is doubled. Consequently the principle of varying liquid velocity with settling velocity allows material of wide size range, to be treated under the same force balance. Thus for the same isodynamic poles for paramagnetics:

$$(\kappa_p - \kappa_l) = \frac{(\rho_p - \rho_l)\ \sin\Theta\ 20.5\text{x}10^{-6}}{I_{50}^2} \qquad (4\text{-}9)$$

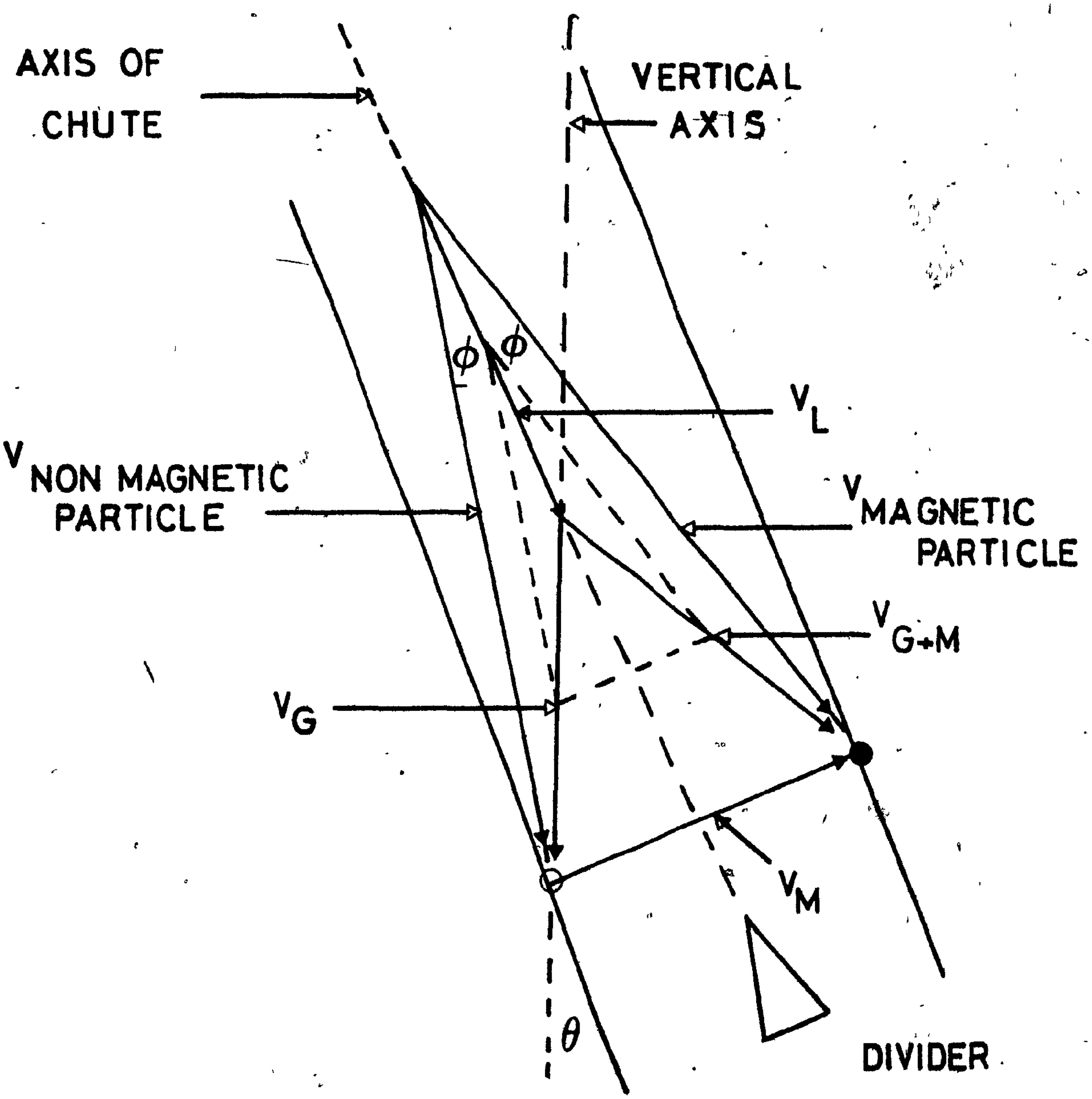

4-5 Vector diagram for particles in the chute of the wet Frantz separator.

Where κ_p and κ_l are the magnetic volume susceptibilities of the solid and liquid respectively and ρ_p and ρ_l the solid and liquid densities.

4.3.3.2(b) Technique

The carrier liquid used in the separator was water for all basic susceptibility measurements. To ensure particle dispersion, a wetting agent (Sodium Metaphosphate) and dispersing agent (sodium alkalate sulphonate) were added. Precipitate samples weighing ≈2 grams were placed in the carrier liquid and treated for 10mins in an ultrasonic bath prior to entry to the elutriator. As an investigation of the magnetic properties of industrial electrolyte, the CEZ liquor was substituted as the carrier fluid.

4.3.3.2(c) Foner Vibrating Magnetometer

In order to verify the results of the "Wet Frantz", a magnetic induction technique, the Foner vibrating magnetometer (117) was used to obtain magnetisation curves for the precipitates studied. The device is a high precision (0.5% accuracy claimed) instrument which monitors the voltage, induced in a set of stationary coils, by the moving dipole field of a sample vibrating perpendicularly between the coils in a uniform field. Samples were placed in a threaded Teflon holder 2cm in length, 0.25cm i.d.. Care was taken to completely fill the holder volume with sample to avoid movement of the material relative to the holder. Any movement of the sample results in a reduced vibration rate and hence a decreased signal from the coils. Calibration of the system was with a Gd_2O_3 sample of known mass and magnetisation.

4.3.4 Wire Magnetisation

4.3.4.1 Theory

In the presence of an increasing field the initial rate of magnetisation of ferromagnetics is geometry and field orientation dependent, while the saturation magnetisation is a characteristic of the material itself. An exponential fit can be made (118) to the experimentally determined curves relating wire magnetisation M_W, to the total field H such that:

$$M_W = M_S \exp\left(-\frac{K}{H}\right) \qquad (4\text{-}10)$$

where K is an empirical constant. The total field H is found from the applied field H_a minus the internal demagnetising field H_D of the material. Thus

$$H = H_a - H_D \qquad (4\text{-}11)$$

while

$$H_D = NM_w \qquad (4\text{-}12)$$

Where N is the demagnetising factor. For infinitely long rods magnetised perpendicular to the long axis there is an exact demagnetising factor of 2π: (119)

$$M_w = M_s \exp \left\{ - \frac{K}{H_a - 2\pi M_w} \right\} \qquad (4\text{-}13)$$

N may be calculated for ellipsoidal wire shapes, these magnetise uniformly throughout. For non ellipsoidal shapes H_D must be estimated experimentally. During initial magnetisation the interval field is very small in comparison to H_a and H_D consequently:

$$H_a \simeq H_D = NM_w$$

N is estimated from the initial slope of the magnetisation curve of the material. Valid estimations can now be made for the magnetisation curves of infinitely long rods (required by the model of Nesset and Finch), from the measured magnetisation slopes of relatively short non cylindrical samples.

4.3.4.2 Procedure

The initial slope $\frac{1}{N}$ is determined from the magnetisation curve of the stainless steel wool sample used as matrix material and measured using the Foner magnetometer. The demagnetising field H_D and internal field $(H_a - H_D)$ as a function of M_w are found. The applied fields necessary to generate the same magnetisation in infinitely long rods are calculated by adding the demagnetising field $H_D = 2\pi M_w$ to the previously determined internal field values. These curves are then fitted to the simple relationship suggested by Clarkson.(119)

4.3.5 Viscosity Measurements

Viscosity measurements of electrolyte solution were made using an Ubelohde suspended level viscometer. The general form of the Bell and Cannon (120) equation is used.

$$\nu = k\Theta - K/\Theta^m$$

Where ν is the kinematic viscosity, Θ the efflux time, and k and K are kinetic energy correction coeffecients associated with glass capillary viscometers. With m=2 calibration of the viscometer was made with water and acetone solutions of known viscosity. Values of k and K were consequently determined at the temperatures at which electrolyte viscosity values were required. A constant temperature water bath was used for all measurements.

4.4 Magnetic Filtrations

Magnetic filtration experiments were carried out using a Sala Magnetics 10-15-20 laboratory high gradient magnetic separator, installed at the Ore Processing Laboratories, CANMET, Ottawa. The magnet produces a uniform field over 10cms. of the central bore for eight fixed field settings, Table 4-1. The fluid system Fig. (4-6), is made from 1.27cm diameter copper tubing expanded at the solenoid bore to hold interchangable matrix cannisters of acrylic tubing (I.D. 3.86cms,O.D.5.14cms). A distance of 15cms between the expansion and the first matrix layer is left to minimize the effect of the expansion on the fluid flow profile (Fig. 4-7). Matricies were

TABLE 4-1

Field Settings and Velocities Available for Filtration Tests

Fields (kOe)	0.66	1.5	4.2	6.8	9.1	21.4
Flow (cm/s)	0.9	1.2	2.3	4.1		

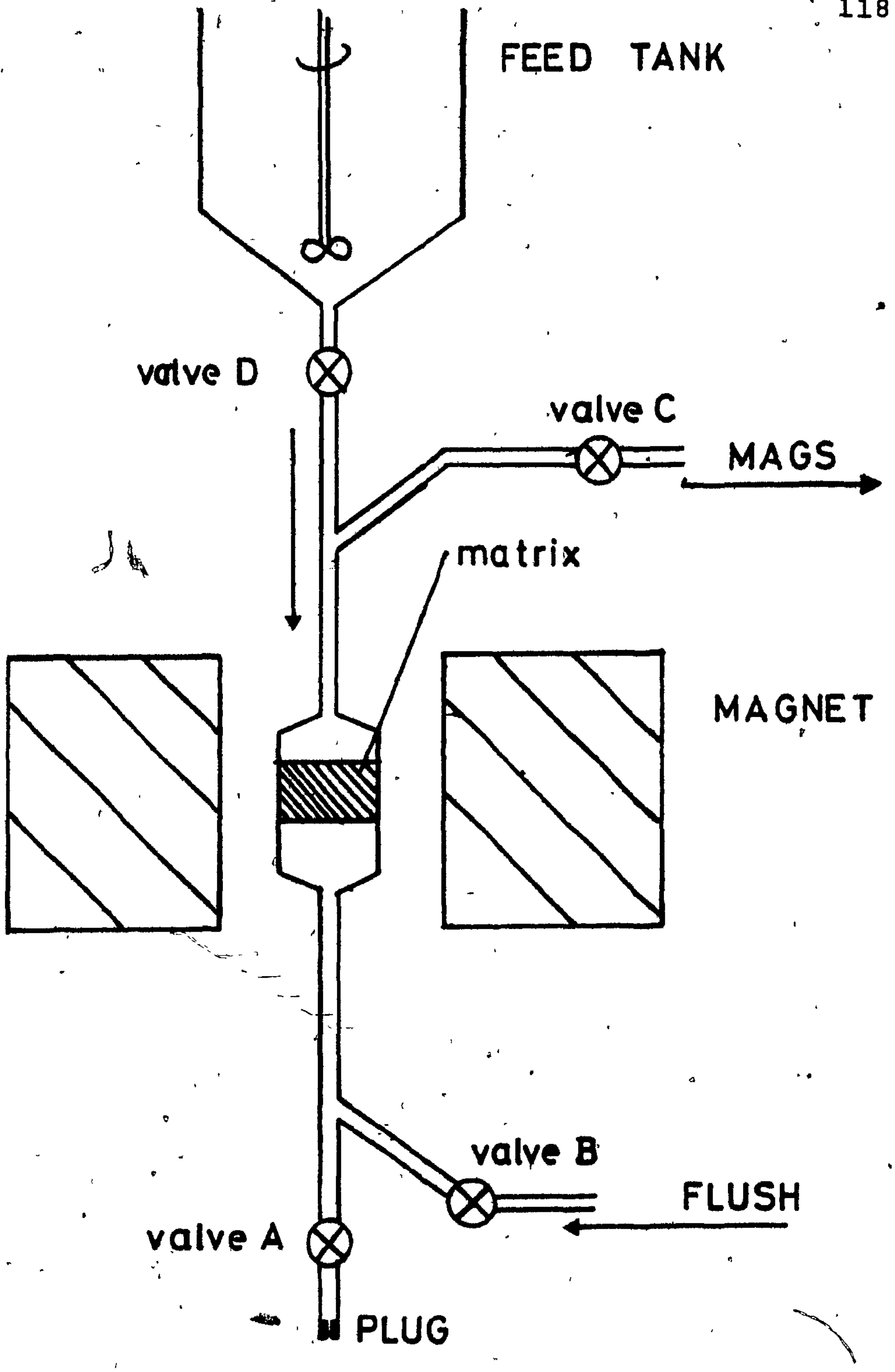

4-6 Fluid and Magnet systems for filtration tests.

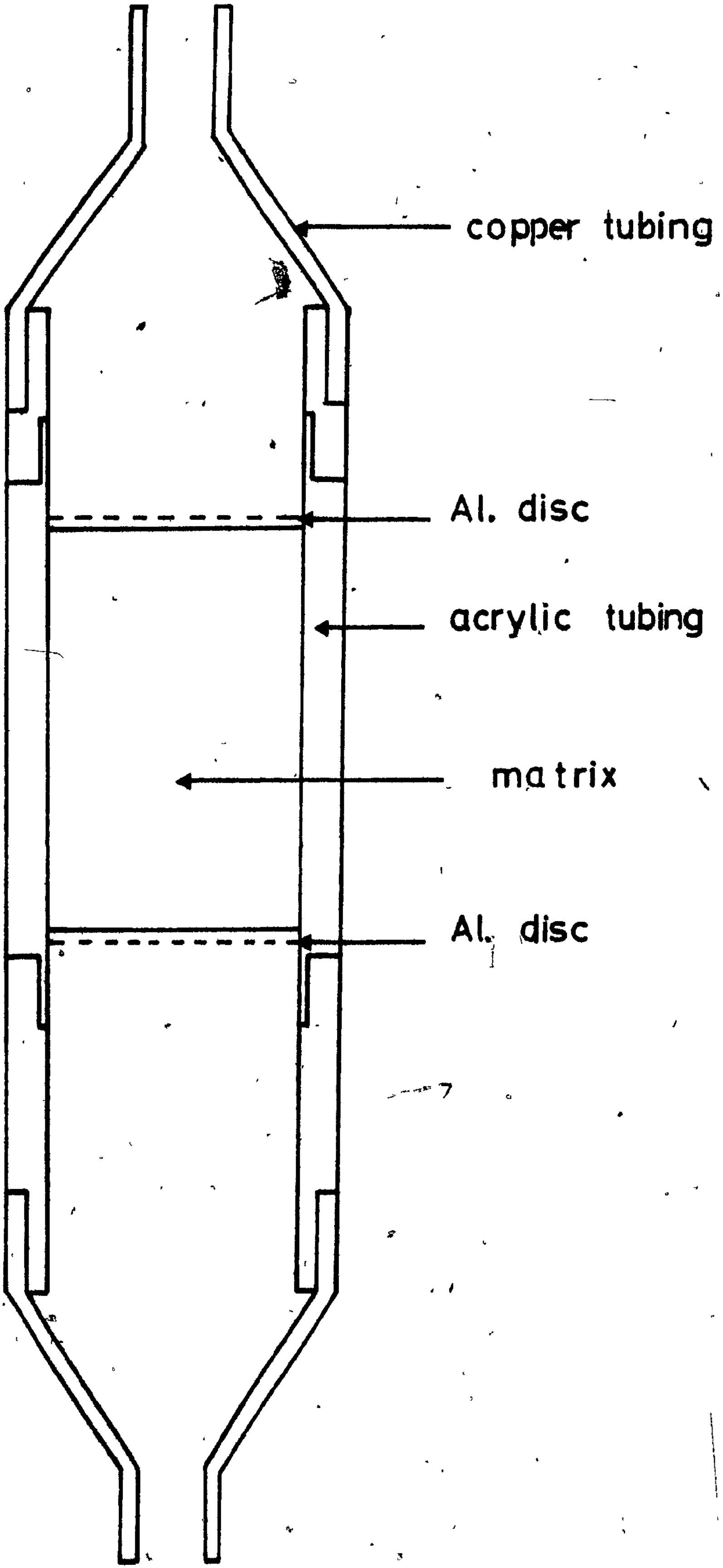

4-7 The matrix cannister design for filtration tests.

made of stainless steel wool (nominal diameter 60μm and density of 7.75g/cm^3) combed and rolled such that wires were oriented 90° to the field and flow. Matrix weight was ≃25 grams with a packing density of ≃5%. An expanded aluminium lath disc was placed at either end of the matrix to ensure matrix stability. Tests were run at constant velocity by employing a constant head in the feed tank sitting directly above the matrix. The velocity was controlled by the use of calibrated plugs of bored brass placed in the outlet of the fluid line. Slurry was fed to the feed tank from a slurry reservoir via a peristaltic pump. Solids in the head tank and reservoir were kept well suspended by vigorous mixing to ensure that constant slurry densities were maintained during filtration tests. The general test procedure was to place the required velocity control plug in the line, then with valves A and C closed backfill the matrix and line with fluid through valve B to just above valve D. (This procedure minimizes entrapment of air in the matrix.)

With all valves closed the head tank was filled with slurry to the correct head height. Field strength was then set to the required value and the filtration started by opening valves D and A simultaneously.

During a test ≈15ml samples of slurry effluent were collected at selected time periods for analysis. At the completion of a test the magnet was switched off and valves D and A were closed. Back flushing, to collect the captured solids, was then achieved by opening valves C and B.

Analysis of the collected samples was made by digesting the solids in acid and atomic absorption analysis. Filtration breakthrough curves were then constructed.

4.5 Experimental Design

Filtration experiments were carried out in three phases. (1) Samples of each precipitate were initially slurried in water then magnetically filtered. The general magnetic filtration characteristics of the precipitates could thus be estimated. The initial operating parameters were determined using the model of Nesset et al. Fluid velocities varied from 0.89 to 2.3cm/s with magnetic field strengths of between 4.2 and 21 kOe. Slurry densities were usually maintained at a level of 10g/L. (2) A second series of tests involved slurrying the precipitate in CEZ electrolyte under the same general experimental conditions as in (1). The experiments included treatment of the precipitates in electrolyte at both room temperature and the more realistic temperature of ≃75°C. (3) Finally, to investigate the ability of the system to treat very fine precipitate particles, a sample of CEZ jarosite thickener overflow was treated in the magnet, again at two operating temperatures.

V. RESULTS

5.1 Precipitate Analysis

5.1.1 X-Ray Diffraction

The diffraction patterns obtained for laboratory prepared jarosites together with CEZ NH_4 jarosite are listed in Table (5-1). Reference d values $^{(55)}$ are compared to measured values in confirming the identity of the respective jarosite phase. Patterns obtained for the iron oxide/hydroxide precipitates are presented in Table (5-2). Again comparison is made to reference patterns $^{(108,109)}$ in identifying the materials. In general the crystallinity of all jarosites precipitates was sufficient to provide well defined patterns and easy identification. This was also the case for α-Fe_2O_3 and Fe_3O_4 precipitates, but was not always so for the α and β FeOOH.

5.1.2 Differential Thermal Analysis

DTA curves produced from goethite precipitates from both EZ and VM procedures at varying precipitation rates are show in Figs. (5-1,2,3). Fig. (5-1) describes a typical curve found for products of the VM procedure.

TABLE 5-1

Experimentally Determined and Reference Diffraction Patterns for Jarosites

K jarosite			Na jarosite			NH_4 jarosite			CEZ NH_4 jarosite		
d values			d values			d values			d values		
meas.	ref.	hkl	meas.	ref.	hkl	meas.	ref.	hkl	meas.	ref.	hkl
5.01	5.10	012	5.85	5.93	101	5.74	5.79	003	5.78	5.79	003
3.64	3.65	110	5.48	5.56	003	5.07	5.12	012	5.12	5.12	012
3.56	3.55	104	5.01	5.05	012	3.61	3.66	110	3.65	3.66	110
3.14	3.11	021	3.66	3.64	110	3.55	3.58	104	3.11	3.12	021/113
3.07	3.08	113	3.13	3.12	021	3.11	3.12/3.09	021/113	3.04	3.05	015
2.88	2.96	006	3.08	3.06	113	2.91	2.91	006	2.91	2.89	006
2.57	2.54	024	2.98	2.96	202	2.56	2.56	024	2.55	2.56	024
2.30	2.30	122	2.79	2.78	006	2.32	2.32	107	2.32	2.31	107
2.29	2.28	107	2.53	2.52	024	1.99	1.99	033	1.99	1.98	033
1.99	1.98	033	2.24	2.23	107	1.93	1.93	027/009	1.81	1.83	220
1.94	1.93	027	1.98	1.98	033	1.83	1.83	220	1.72	1.74	208
1.90	1.90	009	1.90	1.90	027	1.74	1.75	223	1.71	1.72	312
1.84	1.83	220	1.86	1.85	009	1.72	1.72	312	——	——	——

Lattice Parameter Data Based on Hexagonal Cell (Angstroms)

a_o = 7.32 ±.003	a_o = 7.33 ±.002	a_o = 7.33 ±.003	a_o = 7.30 ±.004
c_o = 17.14 ±.005	c_o = 16.65 ±.005	c_o = 17.36 ±.005	c_o = 17.29 ±.005

TABLE 5-2a

Experimentally Determined and Reference Diffraction Patterns for Fe_3O_4 and α-Fe_2O_3

Fe_3O_4			α-Fe_2O_3		
d values			d values		
meas.	ref.	hkl	meas.	ref.	hkl
2.95	2.96	220	3.59	3.66	012
2.52	2.53	311	2.64	2.69	104
2.08	2.09	400	2.49	2.51	110
1.71	1.71	422	2.20	2.28	006
1.61	1.61	511	2.15	2.20	113
1.48	1.48	440	—	2.07	202
1.32	1.32	620	1.80	1.83	024
1.23	1.28	533	1.66	1.69	116
1.21	1.21	444	1.60	1.63	211
1.12	1.12	642	1.57	1.59	018
1.09	1.09	731	1.48	1.48	214
1.05	1.05	800	1.44	1.45	300

TABLE 5-2b

Experimentally Determined and Reference Diffraction Patterns for α and β FeOOH

α-FeOOH (based on orthorhombic)			β-FeOOH (based on tetragonal)		
d values			d values		
meas.	ref.	hkl	meas.	ref.	hkl
4.95	4.98	020	5.31	5.25	200
4.21	4.18	110	3.65	3.70	220
3.40	3.38	120	3.31	3.31	310
3.66	2.69	130	2.60	2.61	400
2.56	2.58	021	2.49	2.54	211
2.49	2.52	101	2.32	2.34	420
2.47	2.48	040	2.25	2.28	301
2.45	2.45	111	2.10	2.09	321
2.27	2.30	200	2.06	2.06	510
			1.95	1.94	411

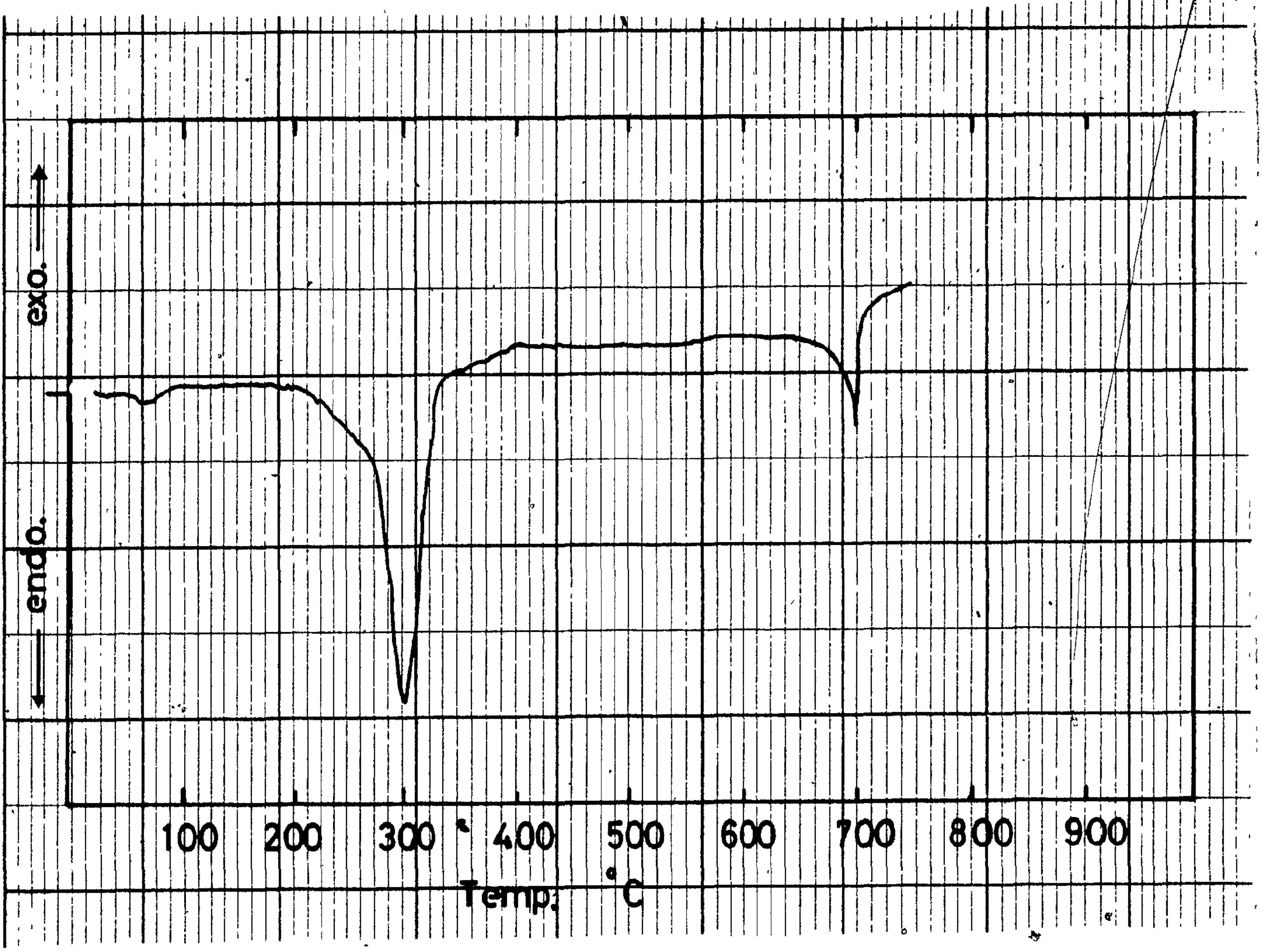

5-1 Differential Thermal Analysis for the VM procedure. α-FeOOH identified

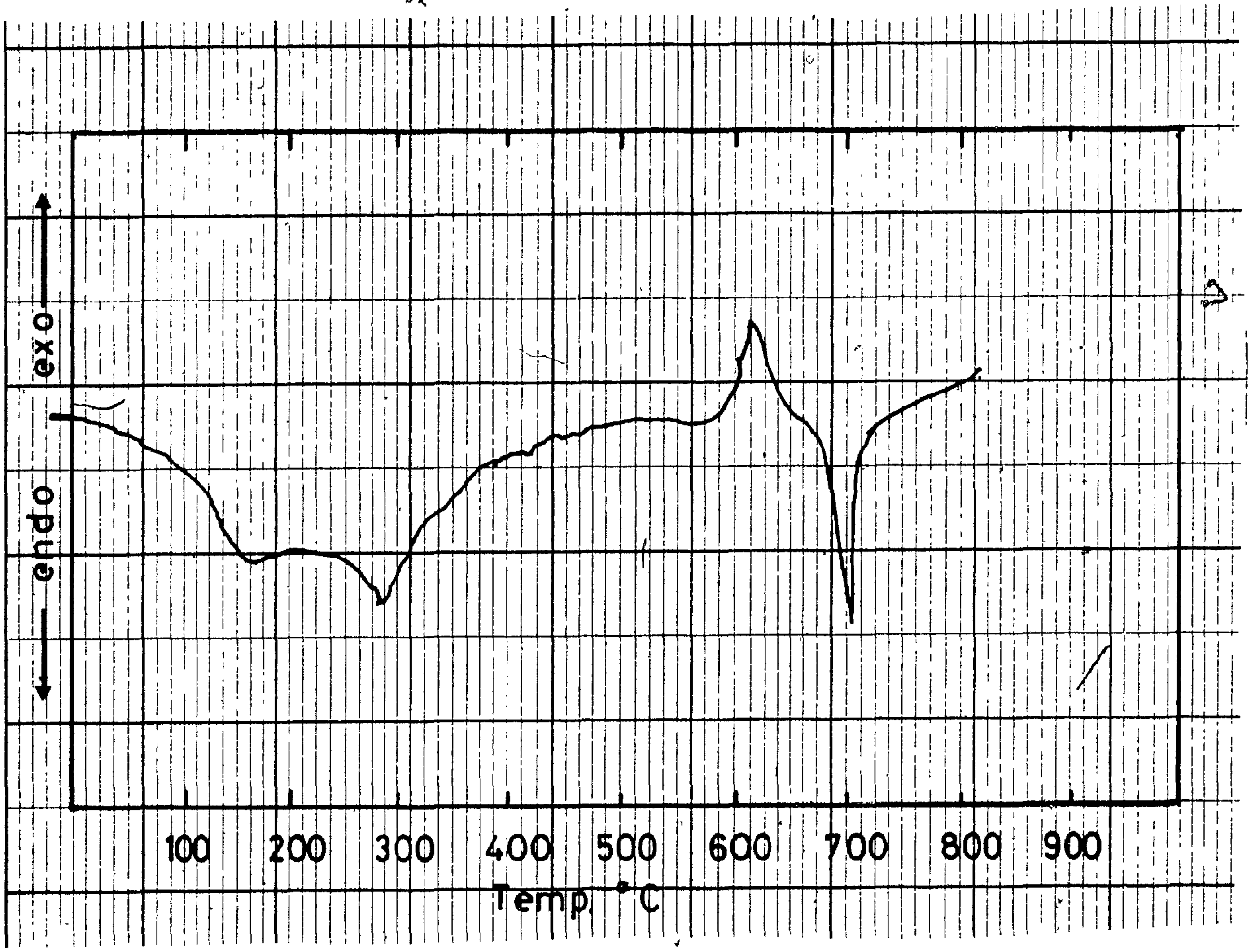

5-2 Differential Thermal Analysis for the EZ procedure. α+β FeOOH identified

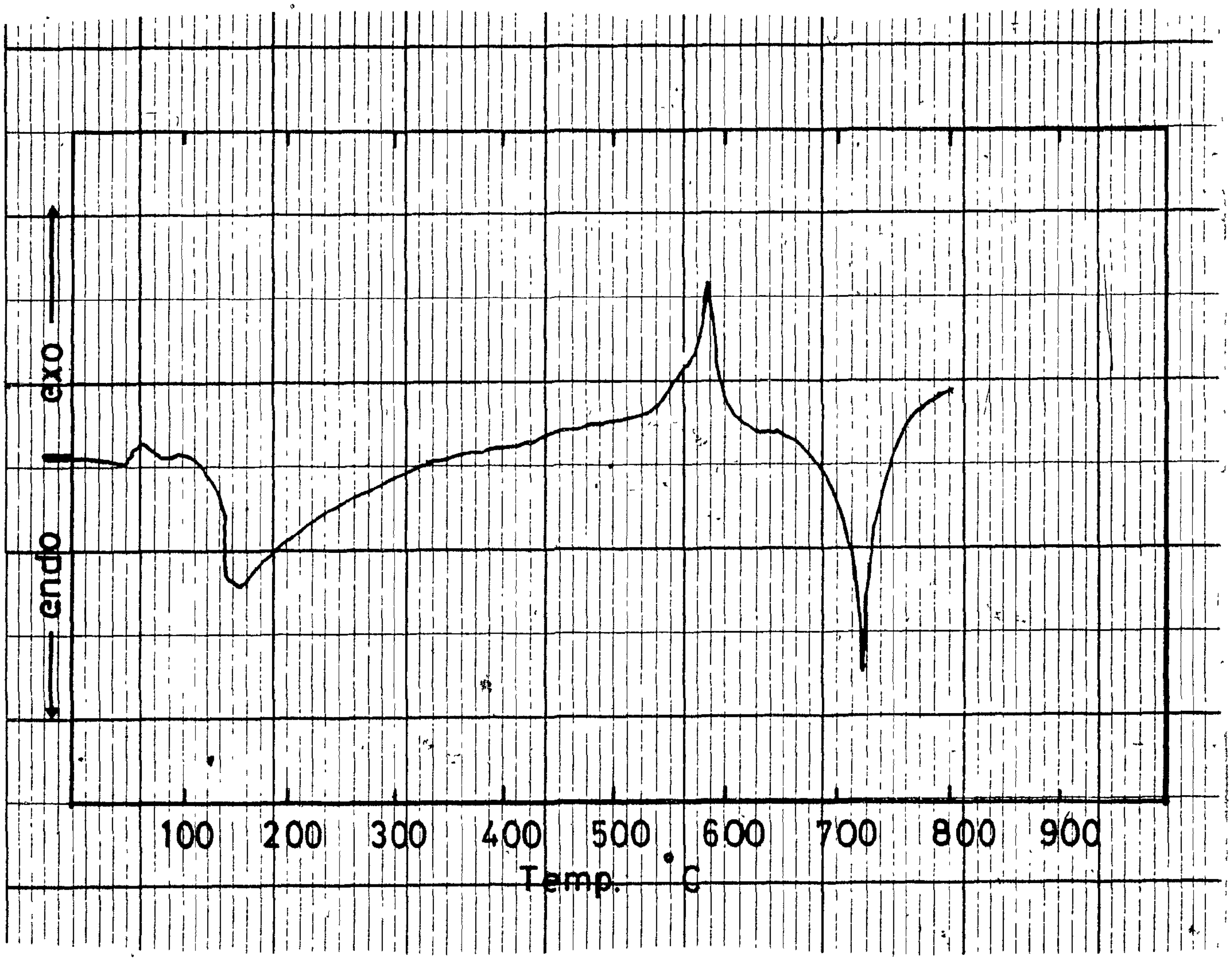

5-3 Differential Thermal Analysis for the EZ procedure at an increased precipitation rate (1.5x). β-FeOOH identified

The endothermic reaction at ≈300°C is characteristic of the dehydration of the goethite crystal and is well documented by Scott and Davey (63) and MacKenzie,(110) as typical of the the α-FeOOH phase. The second endotherm at ≈700°C, describes the breadkdown of the SO_4 ion, still present in small amounts prior to analysis.

Fig. (5-2) is the analysis of precipitates produced by the EZ procedure. A lower endotherm around ≈600° indicates the presence of β-FeOOH.(63) The expected endotherm associated with α-FeOOH is seen at ≈290°C. This more complex analysis is consequently the result of a mixture of fine grained α and β FeOOH.

By increasing the precipitation rate in the EZ procedure a single β-FeOOH phase is apparently produced. The DTA graph for the precipitated species is shown in Fig. (5-3). Here the previously weak endothermic reaction at ≈150°C and exothermic reaction at 580°C are better defined than that that found in the mixed species of Fig. (5-2) and a clear identification of single phase β-FeOOH is made.

5.1.3 Chemical Analysis

Chemical analysis of the synthetically produced precipitates is shown in Table (5-3). The deficiency

TABLE 5-3

CHEMICAL ANALYSIS OF JAROSITES (wt. %)

	Zn	K	Na	NH_4	Fe	SO_4	H_3O+OH
$KFe_3(SO_4)_2(OH)_6$	-	7.3	-	-	30.5	41.1	21.1
$NaFe_3(SO_4)_2(OH)_6$	-	-	3.9	-	32.0	40.5	23.6
$NH_4Fe_3(SO_4)_2(OH)_6$	-	-	-	3.5	29.9	41.6	25.0
CEZ $NH_4Fe_3(SO_4)_2(OH)_6$	1.91	-	-	1.7	27.6	42.1	26.69

of alkali ion from the the thoretical in the jarosite phases is almost certainly due to hydronium ion substitution during precipitation. (55) The magnetically cleaned CEZ jarosite shows a considerable zinc constituent, typical of precipitates formed in electrolyte of high dissolved metal ion content.

5.1.4 Microprobe Analysis

Analysis of the highly magnetic fraction of the CEZ jarosite reveals several distinct phases. Two principal grains are revealed, distinguished by a speckled or smooth appearance, Fig. (5-4). With the beam focused on the red speckled particles only peaks of the spectrum corresponding to iron were indicated. Assuming oxygen (by difference) is the only other element present, the phase was identified as magnetite, Fe_3O_4 "iron ferrite". The second form of particles analysed revealed iron together with up to 20% Zn. Again assuming oxygen by difference, the particles are identified as zinc ferrite, with a varying ratio of Zn:Fe. These ferrite particles originate from the calcine, added during precipitation as a solution neutraliser, and represent unreacted solids and a loss of Zn.

Fig. 5-4 Photograph of Mags product from Davis tube seperation of CEZ jarosite precipitation tank sample.

5.2 Electrolyte Analysis

Electrolyte analysis for iron and zinc content is shown in Table (5-4). Electrolyte (1) corresponds to samples taken from the CEZ jarosite precipitation tank, while Electrolyte (2) represents the thickener overflow sample.

5.3 Parameter Measurement

5.3.1 Particle Density

Pycnometer results for precipitate particle densities are presented in Table (5-5), together with other reported values.(55,111) The results are in good agreement.

5.3.2 Particle Size

Sedigraphs analysis of the precipitates is shown in Figs. 5-5,6,7. Table 5-6 indicates the measured K_{50} of each of the size distributions. It can be seen that synthetically produced jarosites appear to have a considerably larger particle size than those precipitates produced under industrial conditions. Iron oxide/hydroxide precipitates tend to have a smaller particle size than the jarosites.

Micrographs of all solids studied are presented in Figs. (5-8→17). The micrographs shown are representative of several analyses made on each of the precipitates. The general trends are that particle sizes appear to be smaller than those indicated by the sedigraph.

TABLE 5-4

Chemical Analysis of CEZ Electrolyte

	Fe g/L	Zn g/L
Electrolyte (1)	5.0	95.0
Electrolyte (2)	7.25	145.0

TABLE 5-5

Pycnometer Density Results for Precipitates (g/cm^3) .

Material	Measured	Referance
K jarosite	2.8	2.82 (55)
Na jarosite	2.84	2.94 (55)
NH_4 jarosite	2.70	2.66 (55)
α-FeOOH	3.80	4.00 (108)
β-FeOOH	3.81	3.66 (109)
α-Fe_2O_3	4.50	5.20 (111)
CEZ NH_4 jarosite	2.60	-

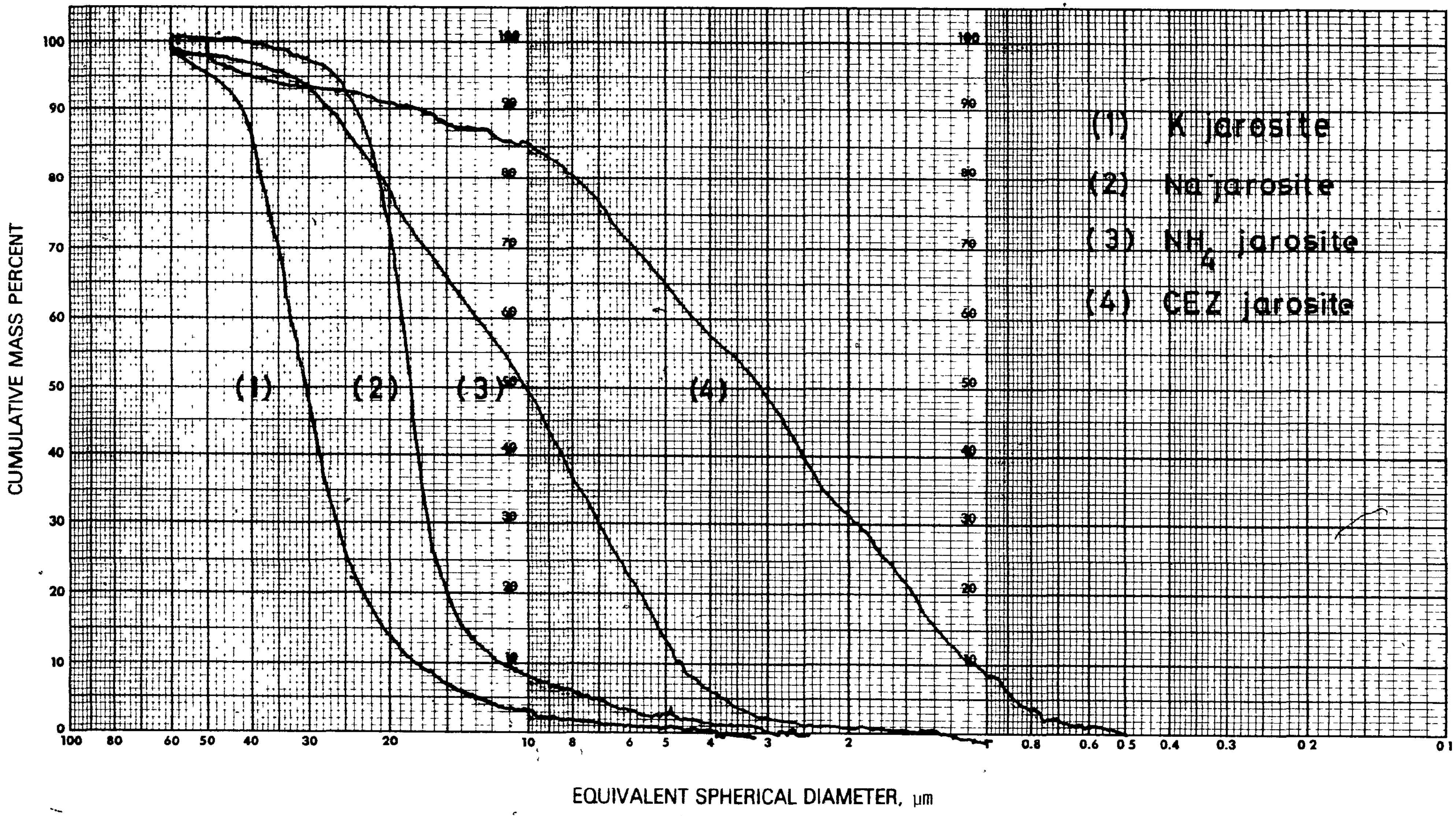

5-5 Sedigraph analysis of synthetic K,NH_4,Na jarosite and CEZ jarosite precipitates.

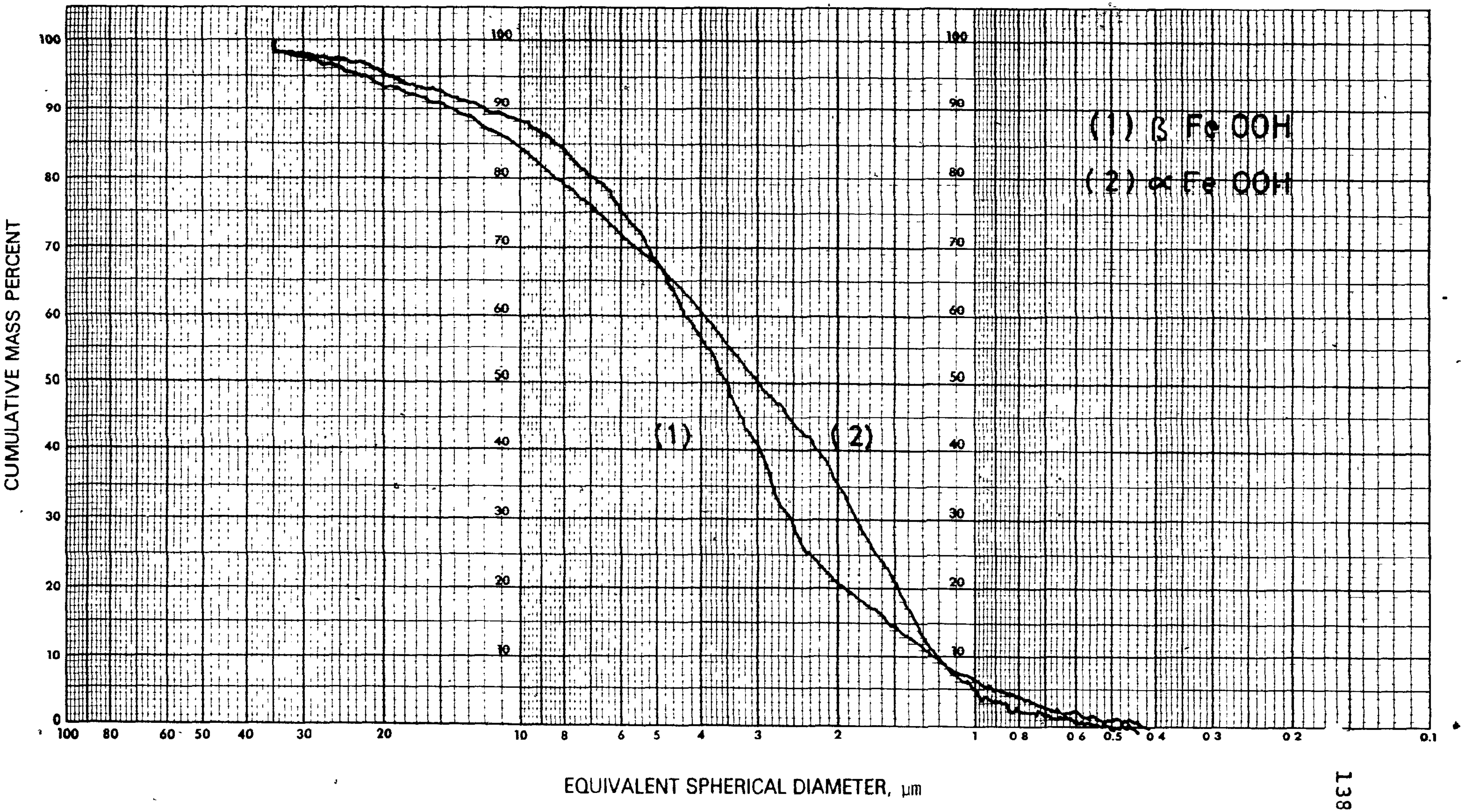

5-6 Sedigraph analysis of synthetic α and β FeOOH precipitates.

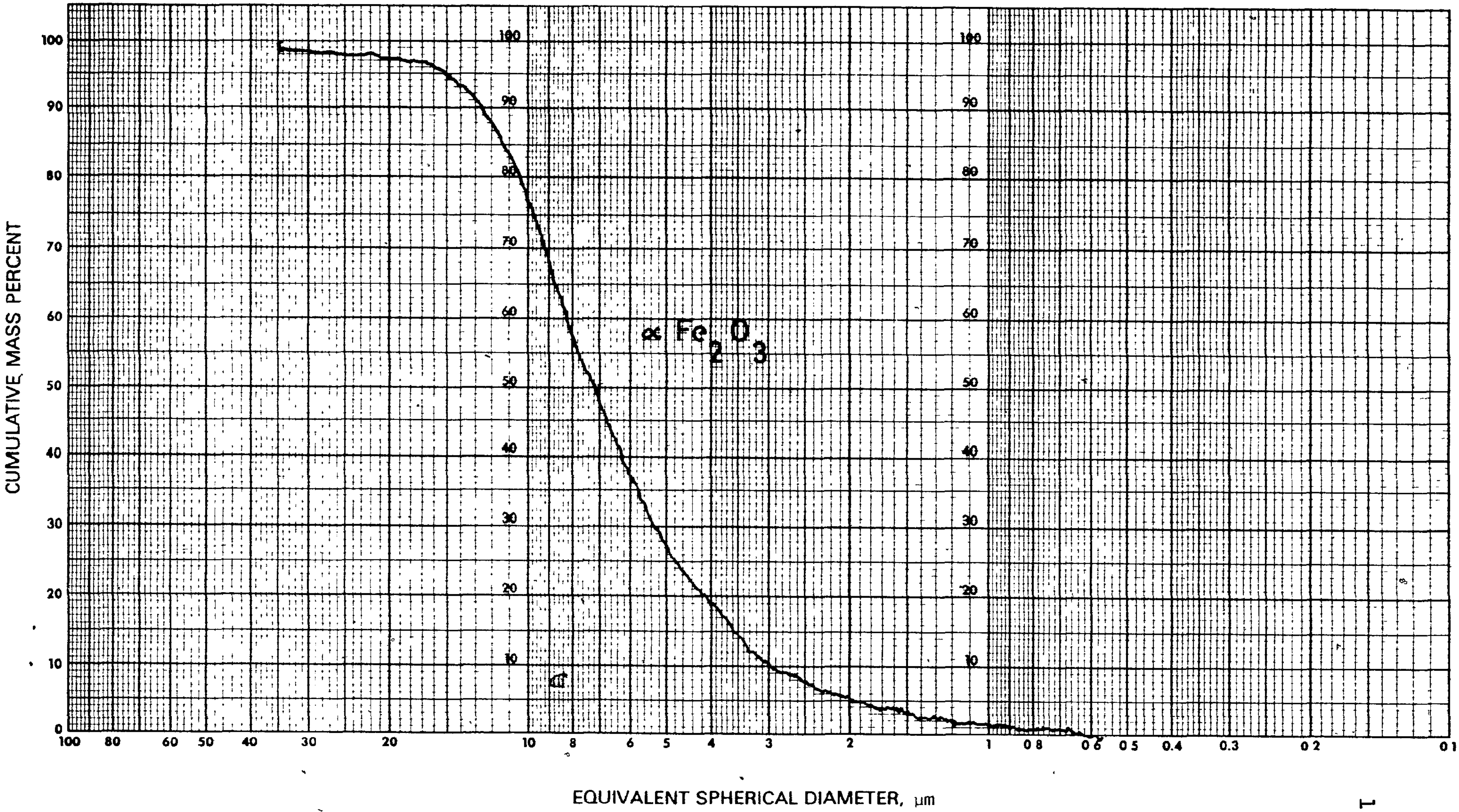

5-7 Sedigraph analysis of synthetic α-Fe_2O_3 precipitate.

TABLE 5-6

Sedigraph K_{50}^{*} Values for Precipitates

Material	K_{50} (μm)
K jarosite	30
Na jarosite	18
NH_4 jarosite	10
α-FeOOH	3.0
β-FeOOH	3.5
α-Fe_2O_3	7.0
CEZ jarosite	3.0

* Where K_{50} is the 50% passing size.

Fig. 5-8 Micrograph of CEZ jarosite, x 10,000

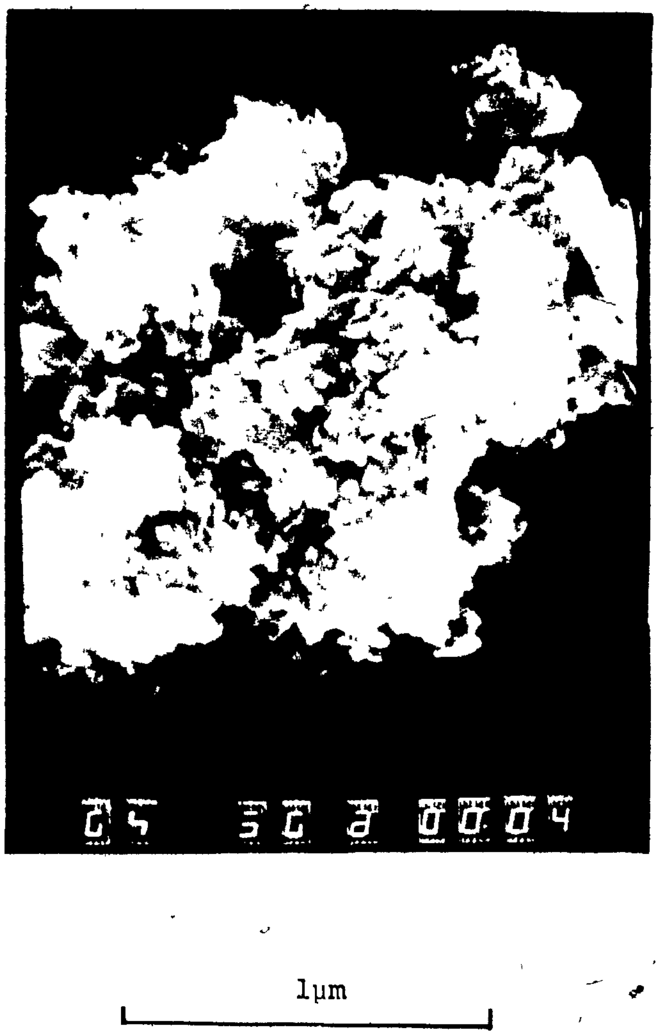

Fig. 5-9 Micrograph of CEZ jarosite, x 50,000

Fig. 5-10 Micrograph of synthetic NH_4 jarosite, x 6,000

Fig. 5-11 Micrograph of synthetic NH_4 jarosite, x 20,000

Fig. 5-12 Micrograph of synthetic K jarosite, x 1,000

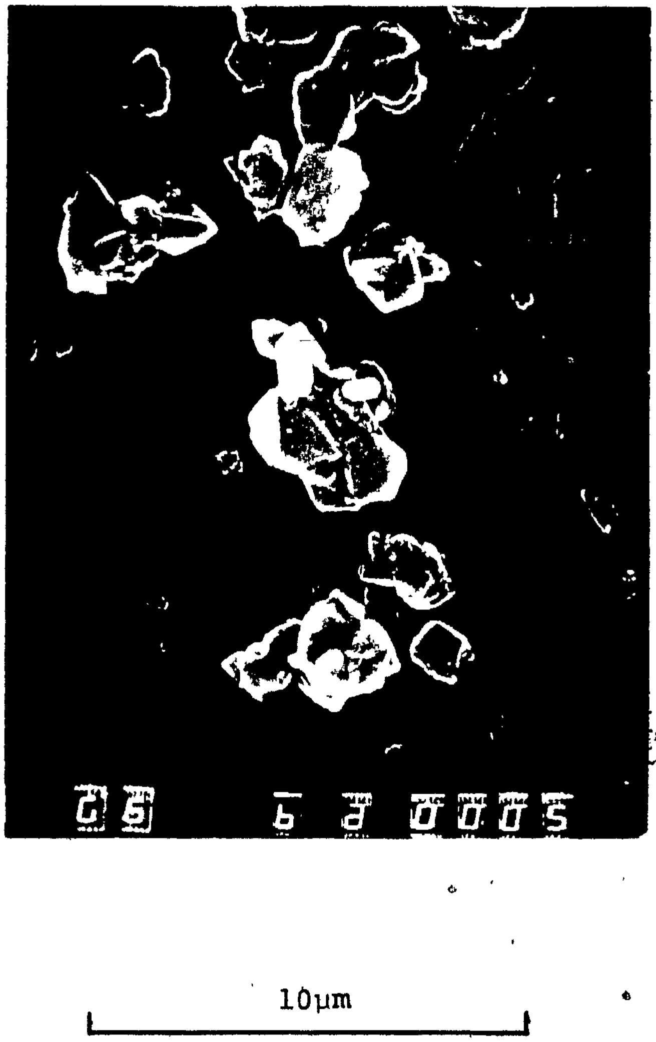

Fig. 5-13 Micrograph of synthetic Na jarosite, x 6,000

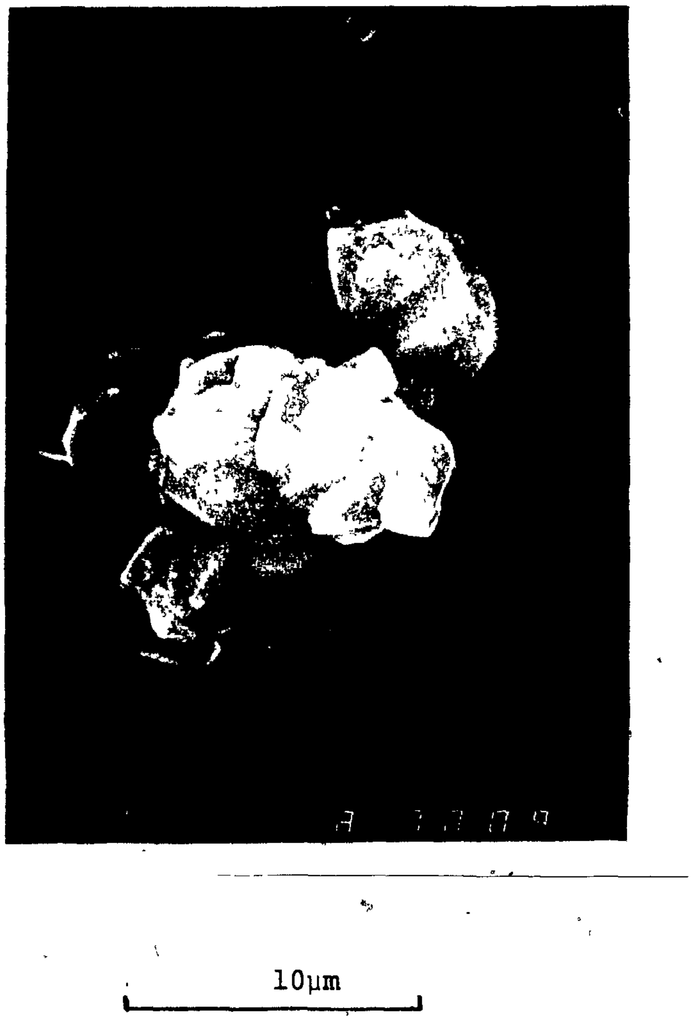

Fig. 5-14 Micrograph of synthetic Na jarosite, x 4,000

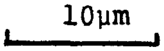

Fig. 5-15 Micrograph of synthetic α-FeOOH, x 2,000

Fig. 5-16 Micrograph of synthetic α-FeOOH, x 20,000

Fig. 5-17 Micrograph of synthetic α-Fe_2O_3, x 10,000

5.3.3 Particle Magnetisation

5.3.3.1 Wet Frantz Measurements

Magnetisation measurements obtained from the Wet Frantz are shown in Table (5-7). Values of I_{50} obtained for each precipitate were applied to equation (4-9) and susceptibility values determined. Magnetisation measurements for pure MnO_2 were also made and the close agreement to susceptibility values obtained by more conventional methods (6) verified the general technique employed with the Wet Frantz. Estimation for values of κ_∞ and M_0 for α-Fe_2O_3 precipitate were made from several measurements of I_{50} obtained from varying side slope Θ between 20^0 and 40^0 and then employing equation (4-8). Measurements of susceptibility for CEZ jarosite with both H_2O and electrolyte as the liquid carrier are also shown. It can be seen that the electrolyte appears to display little effect on the magnetic properties of the material.

5.3.3.2 Magnetometer Measurements

Susceptibility values for the same precipitates obtained using the Foner vibrating magnetometer are also presented in Table (5-7) together with a comparison of results from the Wet Frantz. Values of κ from the

TABLE 5-7

Susceptibility Measurements for Jarosites and Goethites

	Wet Frantz	Foner
	κ x 10^5 (emu/cm^{3}Oe)	κ x 10^5 (emu/cm^{3}Oe)
MnO_2*	11.6 ± .50	———
K jarosite	7.90 ± .27	7.98 ± .16
Na jarosite	7.91 ± .27	7.78 ± .15
NH_4 jarosite	7.82 ± .28	8.04 ± .16
α-FeOOH	14.4 ± .7	15.5 ± .30
β-FeOOH	15.5 ± .7	16.5 ± .40
CEZ jarosite (H_2O)	7.7 ± .24	7.2 ± .14
CEZ jarosite (Electrolyte)	6.97 ± .26	———

* Used as standard to check accuracy of wet system against a value of 11.7×10^{-5} emu/cm^{3}Oe reported (91) using the dry Frantz technique.

Standard errors are based on the pooled variance of 20 measurements of I_{50} including four repeats for K jarosite.

two methods are very similar for all the precipitates. Hematite magnetisation measurements (Table 5-8) however, differ slightly in values of κ_∞ and more perceptibly in values of M_0.

5.3.4 Wire Magnetisation

Wire magnetisation curves for 60μm stainless steel wire are presented in Fig. (5-18). The curves represent measured and corrected magnetisation behaviour, together with a fit to equation (4-10). Table (5-9) describes the value of M_s and K found from the presented magnetisation curves, as well as reported values for expanded metal lath (wire diameter 800μm).(101) The stainless steel wool begins to saturate at 8-10KOe towards a value of M_s estimated at 190emu/g.

5.3.5 Electrolyte Viscosity and Density Measurements

Viscosity and density measurements for both electrolyte samples are presented in Table (5-10). Results for both kinematic and absolute viscosity are presented. The expected decrease in viscosity is observed at elevated temperatures with a concurrent decrease in density.

TABLE 5-8

Magnetic Susceptibility and Magnetisation Values for α-Fe_2O_3 Precipitate

Technique	$\kappa_\infty \times 10^4$ emu/cm^{3}Oe	M_0 emu/cm^3
Magnetometer	1.28 ± .25	0.661 ± .05
Wet Frantz	1.35 ± .32	0.495 ± .12

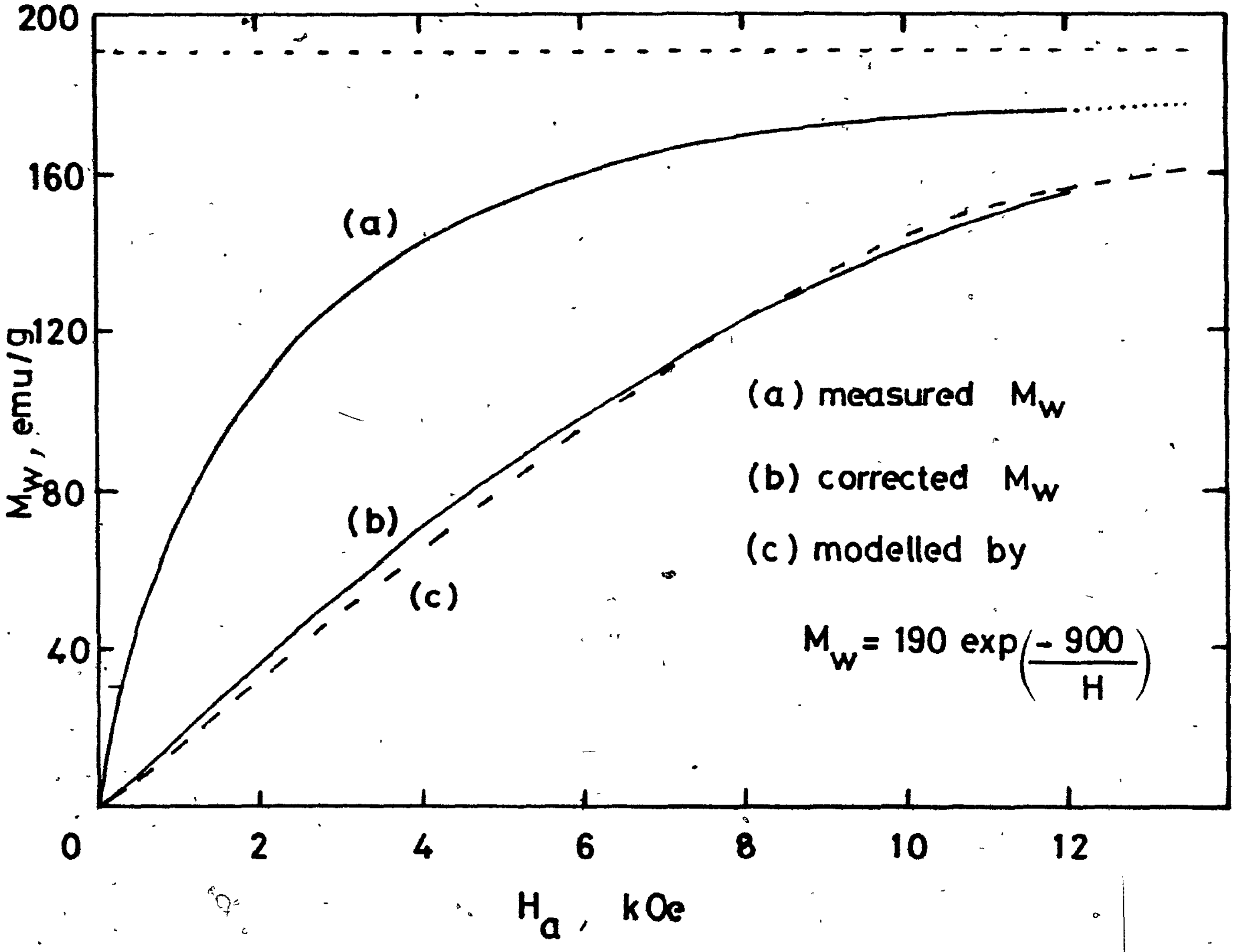

5-18 Wire magnetisation curves for stainless steel wool of diameter 60μm.

TABLE 5-9

Wire Magnetisation Data

Material	M_s emu/g.	K
s/s mesh	190	400
s/s wool	190	900

TABLE 5-10

Viscosity and Density Measurements for CEZ Electrolytes

Sample	Viscosity		Density
	Kinematic (Stokes)	Absolute (Poise)	g/cm^3
Electro (1) (25°C)	.0338	0.0453	1.340
Electro (1) (70°C)	.0127	0.0167	1.314
Electro (1) (80°C)	.0105	0.0138	1.308
Electro (2) (25°C)	.0414	0.0567	1.370
Electro (2) (70°C)	.0143	0.0192	1.349

5.4 Filtration Experiments

Details of all filtration experiments are shown in Table (5-11). Initial experimental conditions were calculated for 100% recovery using the equations of Nessét et al (Appendix 2). The resulting breakthrough curves are presented together with the data fitted curves produced from the model of Collan et al.$^{(105)}$

Initial experiments with synthetic potassium jarosite (Runs 1,2) gave 100% recovery for the conditions indicated, while plugging of the matrix was minimal. A range in filtration curves for the system were then produced by adjusting field and flow. Fig. (5-19) indicates the produced breakthrough curves runs 3,4. Experimentally determined points are shown together with the data fitted curve. The essential feature of Fig. (5-19) is the dependence of filtering performance on slurry velocity. Inspection of t_e values (time to C_{out}/C_{in} = 0.1) Table (5-11), indicates that a considerable decrease in filter efficiency takes place with increasing flowrate.

The performance of synthetic potassium jarosite using an expanded metal lath matrix is shown in Fig. (5-20) (runs 5,6,7). A general deterioration in filter performance is apparent in comparison to steel wool filtration and clearly indicates the reduction in field gradient by

Run #	Material	Fluid	Matrix	H_a	U_∞	Feed	t_e	t_0	ℓ_0	K
19**	CEZ+F	H_2O	24g wool	9,100-Oe	0.9 cm/s	35g-10g/L	—	—	—	—
20	CEZ-F	H_2O	24g wool	9,100-Oe	0.9	35g-10g/l	270s.	342s.	0.44cm.	12.18
21	$Fe(OH)_3$	H_2O	24g wool	21,000-Oe	0.9	5L.	<15s.	99s.	4.23cm.	1.27
22	NH_4	Electro 1	24g wool	9,100-Oe	0.9	50g-10g/L	165s.	246s.	0.7cm.	7.67
23	α-FeOOH**	Electro 1	24g wool	9,100-Oe	0.9	45g-10g/L	90s.	192s.	1.36cm.	3.95
24	α-Fe_2O_3	Electro 1	24g wool	9,100-Oe	0.9	40g-10g/L	170s.	299s.	1.02cm.	5.27
25	CEZ-F	Electro 1	24g wool	4,240-Oe	0.9	48g-10g/L	60s.	151s.	2.06cm.	2.61
26	CEZ-F	Electro 1	24g wool	9,100-Oe	0.9	40g-10g/L	95s.	166s.	0.96cm.	5.58
27	CEZ-F	Hot Electro 1	24g wool	9,100-Oe	0.9	40g-10g/L	135s.	210s.	0.672cm	8.02
28	CEZ ov	Electro 2	24g wool	21,000-Oe	0.9	5L	120s.	199s.	1.02cm.	5.28
29	CEZ ov.	Hot Electro 2	24g wool	21,000-Oe	0.9	5L	150s.	203s.	0.77cm.	6.99
30	Na	H_2O	24g wool	4,240-Oe	0.9	70g-10g/L	120s.	190s.	0.94cm.	5.71
31*	Fe_3O_4	Electro 1	35g mesh	1,500-Oe	2.9	40g-10g/L	—	—	—	—
32*	CEZ+F	Electro 1	35g mesh	1,500-Oe	2.9	—	—	—	—	—

* 100 capture of material

** Plugging of matrix encountered

PAGE-159 missing

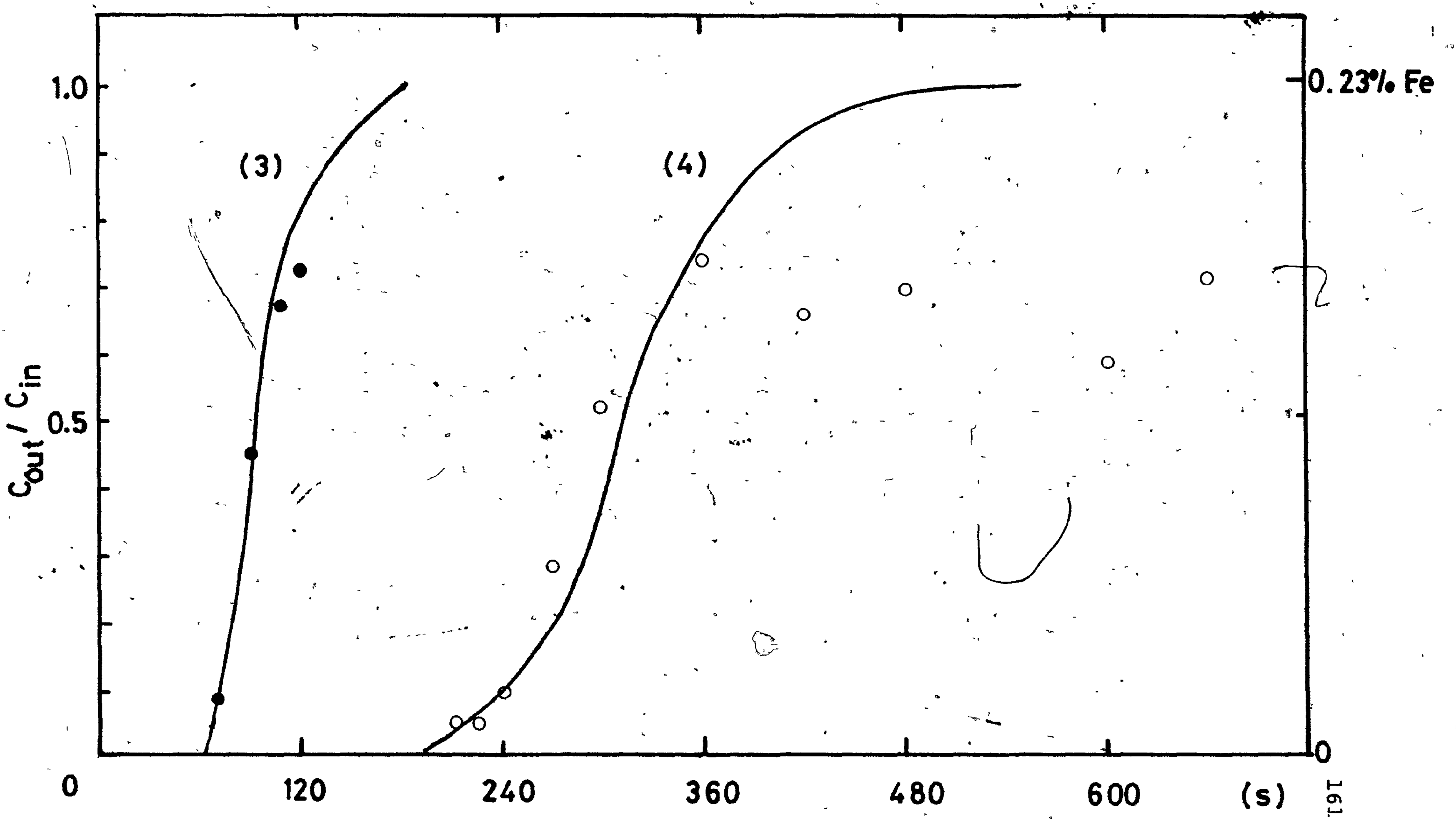

5-19 Breakthrough curves for synthetic K jarosite, runs (3) H_a=4.2kOe, U_∞=2.3cm/s. (4) H_a=4.2kOe, U_∞=1.2cm/s.

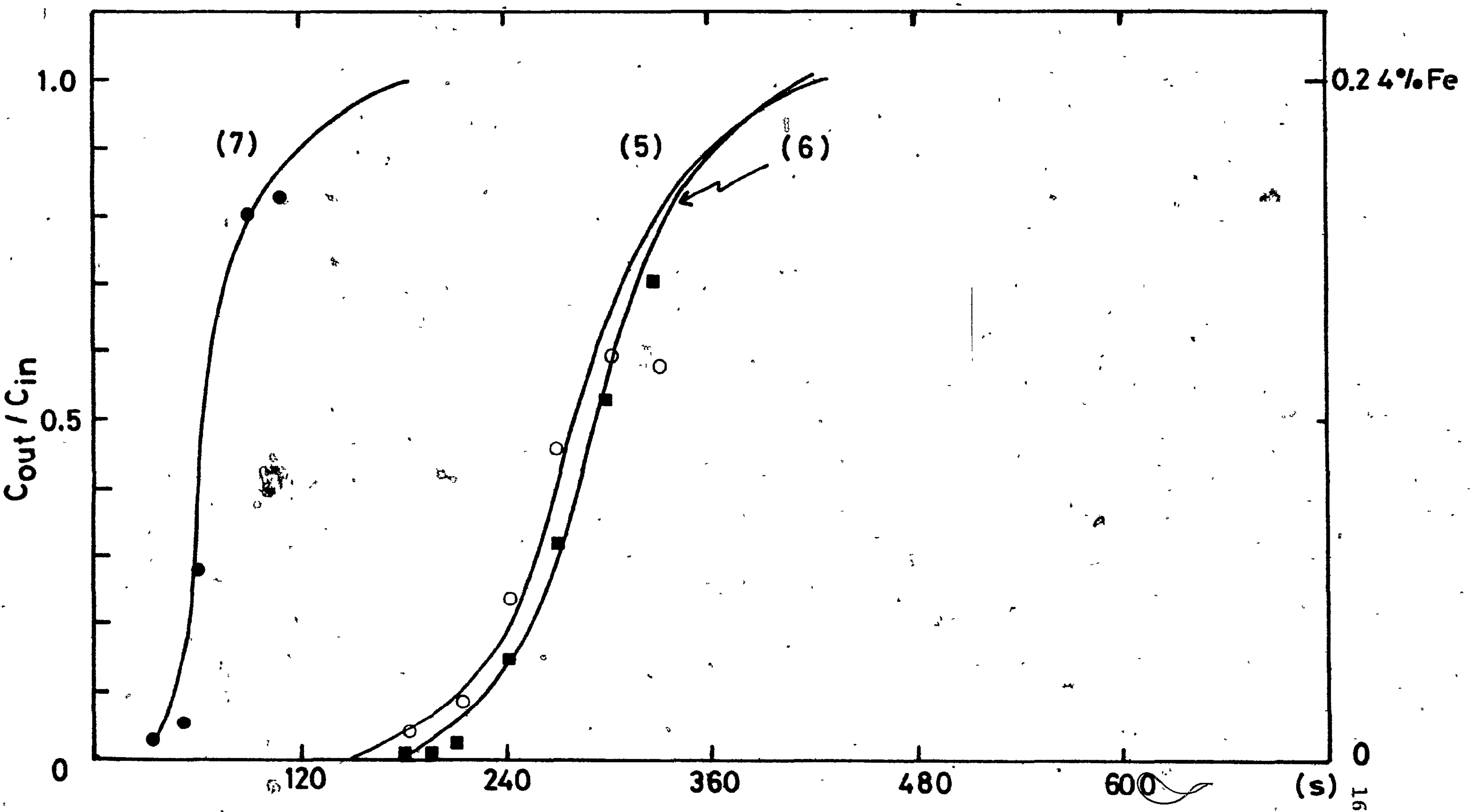

5-20 Breakthrough curves for synthetic K jarosite, runs (5) H_a=4.2kOe, U_∞=0.9cm/s. (6) H_a=9.1kOe, U_∞=0.9cm/s. (7) H_a=9.1kOe, U_∞=2.3cm/s.

introducing larger diameter wires as matrix material. The stainless steel wool matrix was consequently used for the bulk of the remaining tests.

The performance of synthetic Na jarosite is shown in Fig. (5-21) (runs 8,9,10). Here an increase in field strength results in the expected improvement in filtration performance, while runs 8,9 indicate the general repeatability of the tests. In order to demonstrate the effectiveness of the filtration process a test was made, run 30, with Na jarosite passing through the matrix with no magnetic field. After two minutes the field was turned on and the filtration process started under the same conditions as run 9. Fig. (5-22) denotes the comparison behaviour of the breakthrough curve of run 30 with that of runs 8,9, while Fig. (5-23) displays visually how in samples of effluent, solids content changes with time after the magnet is switched on. Comparison of K values (Table 5-11) for both runs indicate the similarity of the matrix filtration characteristic even though the matrix operated under slightly different conditions in run 30. Comparison of t_0 values shows a decrease for run 30, which can be expected as solids are present throughout the matrix at the time when the magnet is switched on. This test does visually demonstrate that true magnetic capture is

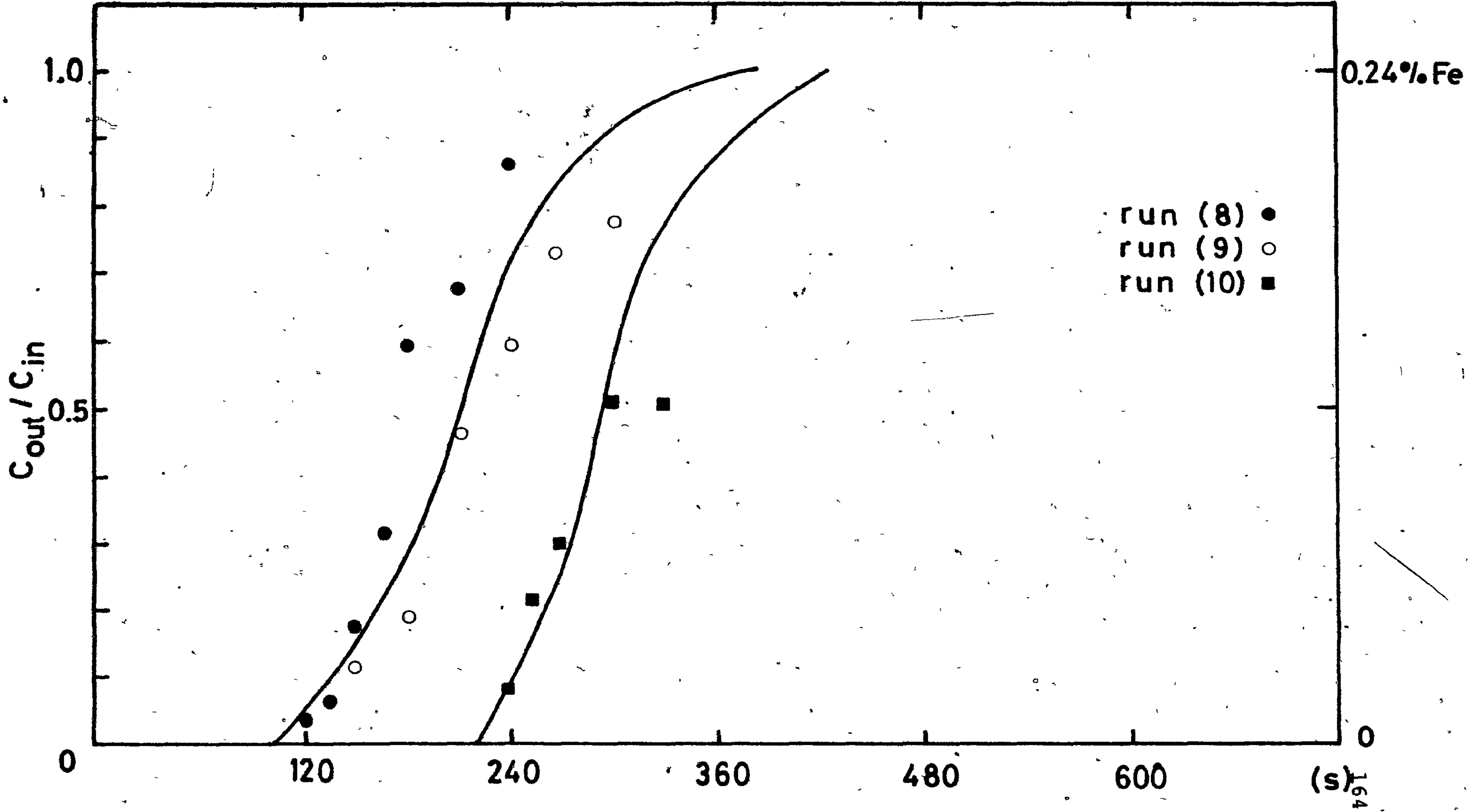

5-21 Breakthrough curves for synthetic Na jarosite, runs (8),(9) H_a=4.2kOe, U_∞=0.9cm/s., (10) H_a=9.1kOe, U_∞=2.3cm/s.

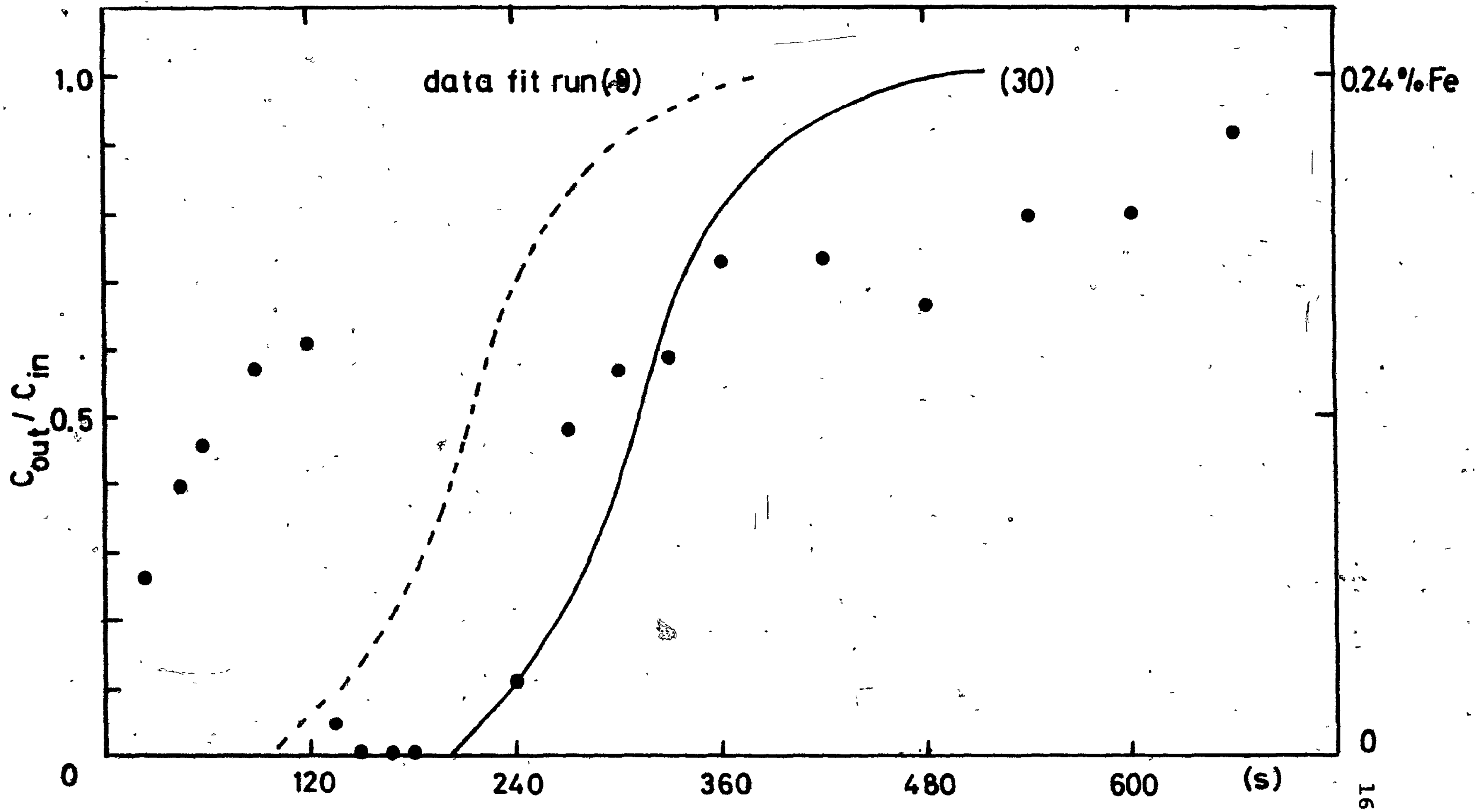

5-22 Breakthrough curve comparison of run 9 with the delayed magnet energizing of run 30. H_a=4.2kOe, U_∞0.9cm/s.

5-23 Photograph of samples of effluent with time of run 30.

taking place and that errors in establishing when filtration starts in the usual test procedure are minimal. Fig. (5-24) (runs 11,12,13) shows the results of synthetic NH_4 jarosite under the same conditions as for Na jarosite. The filtration performance is very similar, especially when considering t_0 values. The t_0 is almost doubled by an approximate doubling of the field strength. Similarly the increasing steepness of the curves with field strength is noted with a corresponding increase in values of K. This indicates that the matrix approaches a fully loaded condition closer to the efficient filtration time t_0, and that the filter is working more efficiently.

Tests involving goethite precipitates were made exclusively with α-FeOOH. The physical properties of both α and β phases are similar, while α-FeOOH is the major constituent of both VM and EZ processes. Fig. (5-25) (runs 14,15,16) shows how filtration times are considerably shorter than those found for the jarosites. While this material has a higher magnetic susceptibility than the jarosites the much reduced particle size accounts for the reduction in filtering efficiency. Fig. (5-25) (run 19) also includes the results of filtration tests of α-Fe_2O_3 precipitate. A considerable

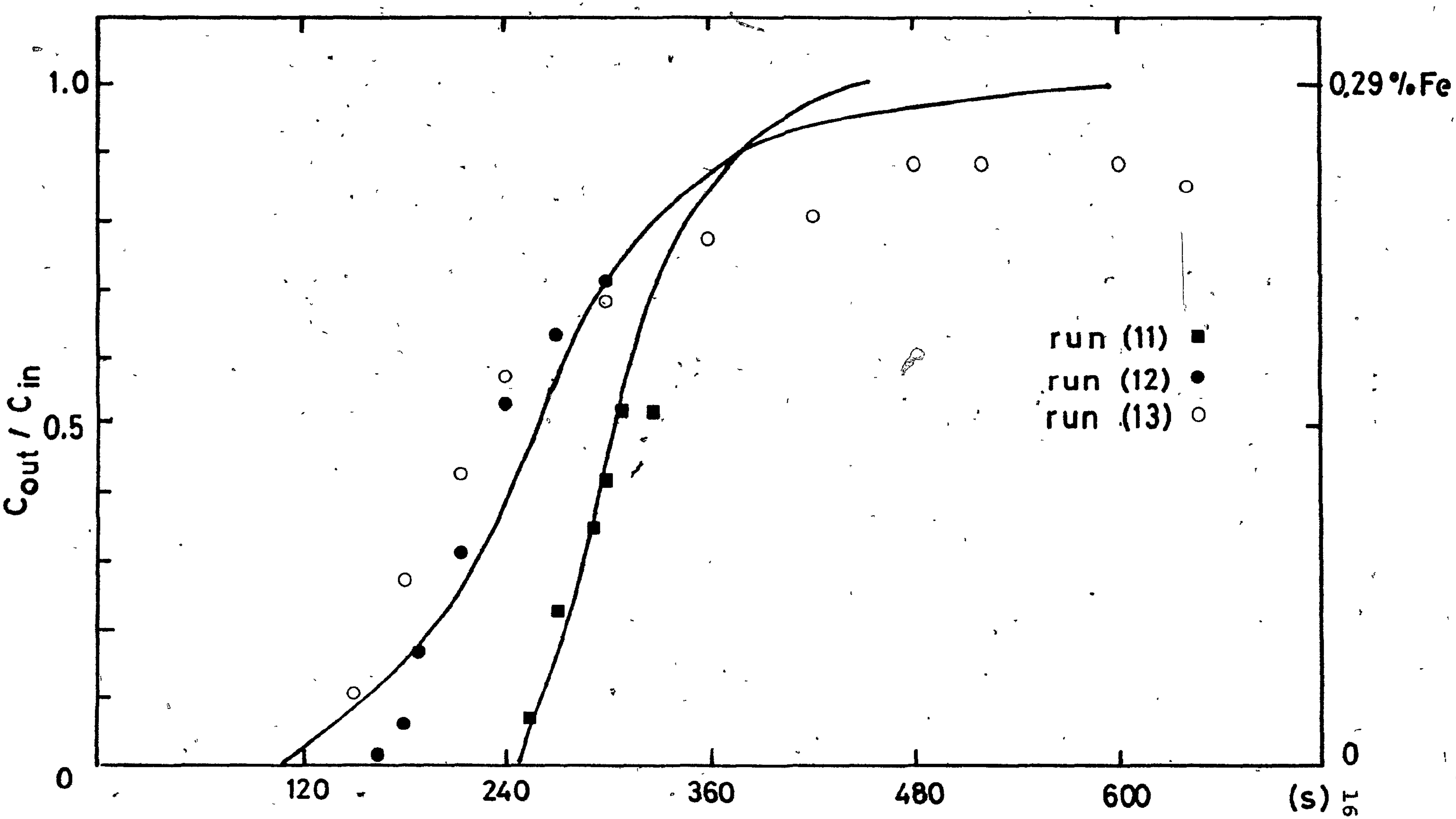

5-24 Breakthrough curves for synthetic NH_4 jarosite runs (11) H_a=9.1kOe, U_∞=0.9cm/s, (12)(13) H_a=4.2kOe, U_∞=0.9cm/s.

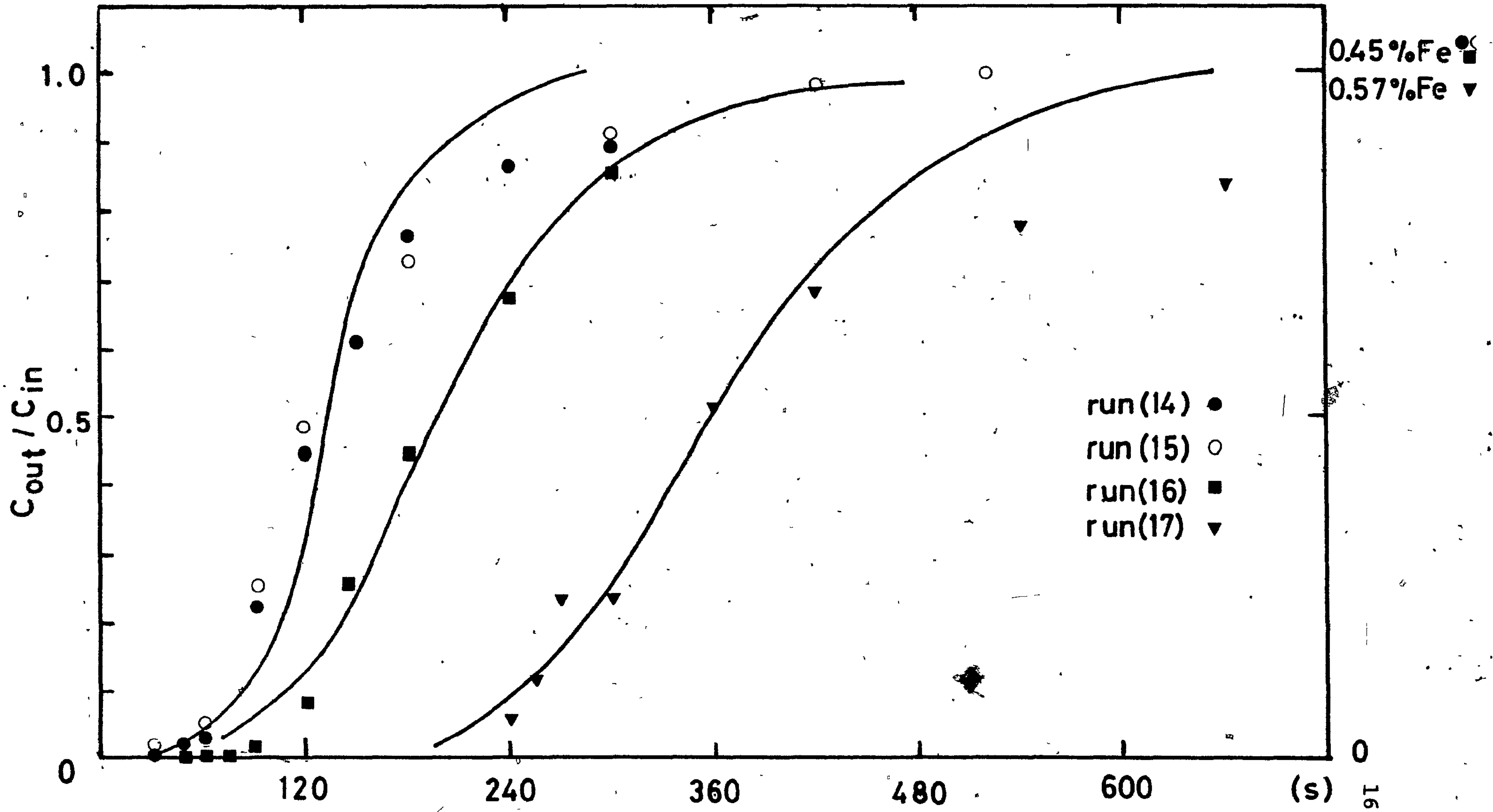

5-25 Breakthrough curves for synthetic α-FeOOH runs 14,15,16 and α-Fe_2O_3, run 17. (14),(15) H_a=4.2kOe, U_∞=0.9cm/s. (16) H_a=9.1kOe, (17) H_a=9.1kOe, U_∞=0.9cm/s.

improvement in filtration characteristics over α-FeOOH can be seen. This is accounted for by the larger particle size exhibited by the hematite precipitate.

The performance of material obtained from the CEZ jarosite precipitation tanks is indicated in runs 18,19. Plugging of the matrix took place after very short filtration times. This was the result of the highly magnetic ferrite fraction overloading and blocking the front of the wool matrix. In order to test CEZ jarosites, samples were magnetically cleaned prior to any filtration tests. This was initially achieved by passing slurried samples of the CEZ solids through a Davis Tube to obtain a jarosite "non-mags" product suitable for further testing. Fig. (5-26) (run 20) shows the initial results of "clean" CEZ jarosite filtration. Comparison with Fig. (5-24) (run 11), synthetic NH_4 jarosite, shows some deterioration in filtration performance with a decrease in efficient filtration times. Although the magnetic susceptibility of this material is comparable to that of synthetic NH_4 jarosite, the considerably reduced particle size obviously deteriorates the magnetic filtration performance.

Final filtration runs with water as carrier fluid were made on a slurry of freshly precipitated ferric hydroxide (Fig. 5-27) (run 21). The colloidal nature of the precipitate

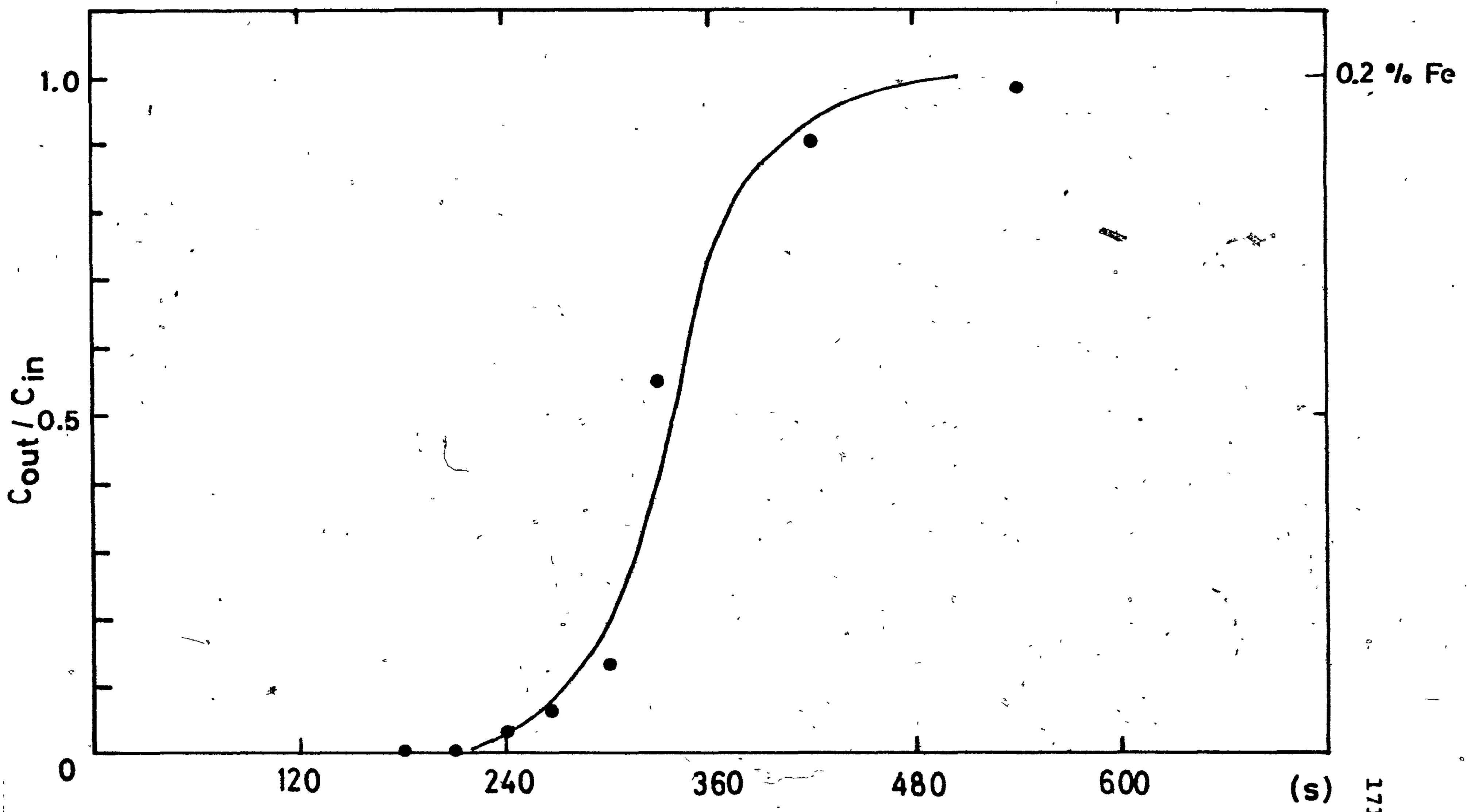

5-26 Breakthrough curve for "clean" CEZ jarosite, run 20. H_a=9.1kOe, U_∞=0.9cm/s.

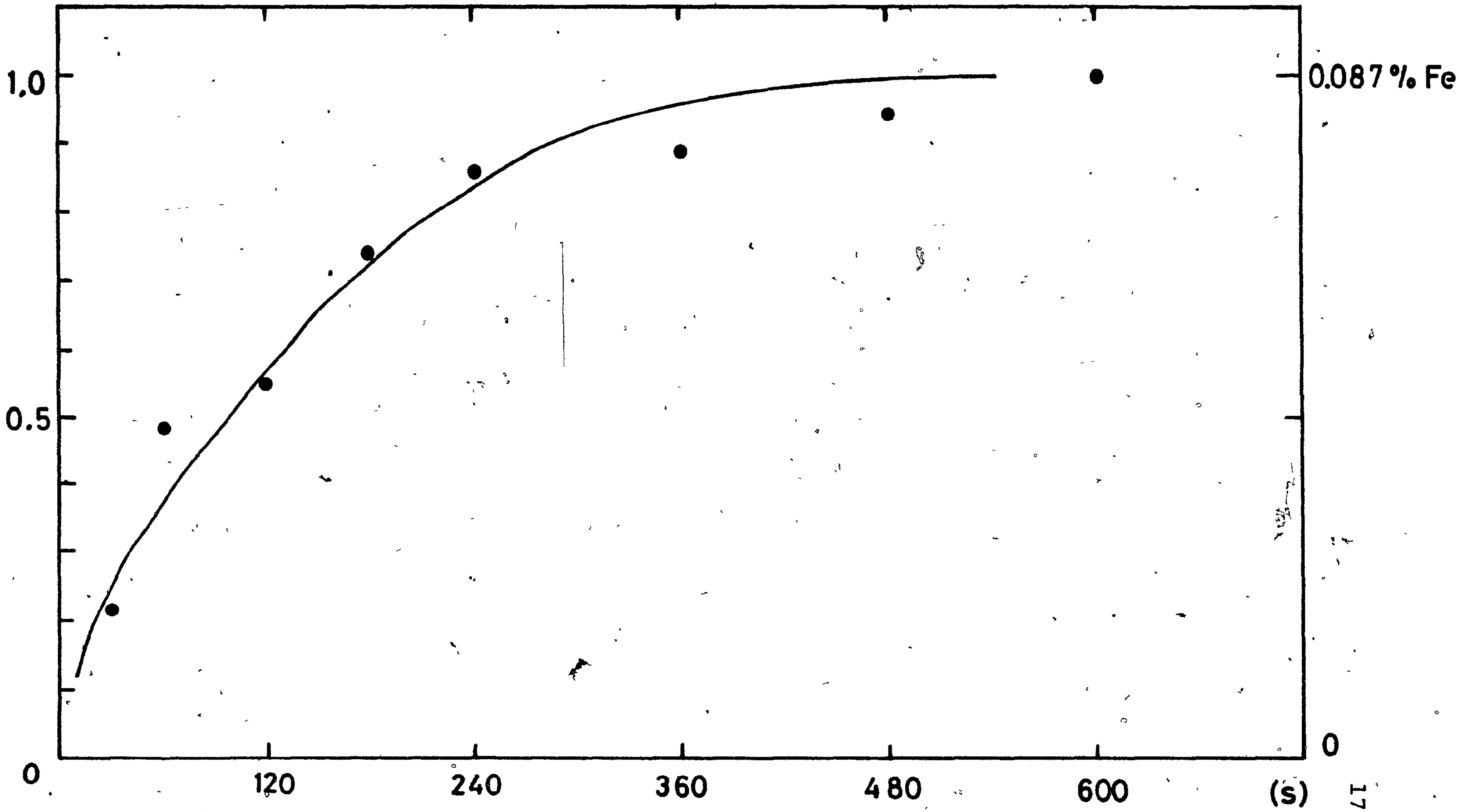

5-27 Breakthrough curve for hydrated ferric oxide, run 21. H_a=21.0kOe, U_∞=0.9cm/s.

does not appear to lend itself to easy magnetic filtration although appreciable solids removal does take place.

Having defined the general filtration characteristics of the precipitates a second series of tests was carried out with CEZ electrolyte as the carrier fluid. Fig. (5-28) (run 22) and Fig. (5-29) (runs 23,24) show how a synthetic NH_4 jarosite and α-FeOOH and α-Fe_2O_3 behave in the filter with an electrolyte. For the same filtration conditions used with water as the fluid medium, the electrolyte has a considerable deliterious effect on the filtration process. Efficient filtration times appear to be halved with curves becomming shallow commensurate with less efficient use of matrix capacity. Plugging of the matrix took place with α-FeOOH precipitate.

Tests with clean CEZ jarosite in electrolyte at 25°C and 75°C are presented in Fig. (5-30) (runs 25,26, 27). Again the decrease in filter efficiency with electrolyte at room temperature compared to hot electrolyte is indicated,with only a slight improvement in the filtration taking place with increase in background field. Run 27 shows the effect of hot electrolyte. A considerable improvement can be seen in the curve, with an efficient filtration time approaching that found with water as the liquid carrier.

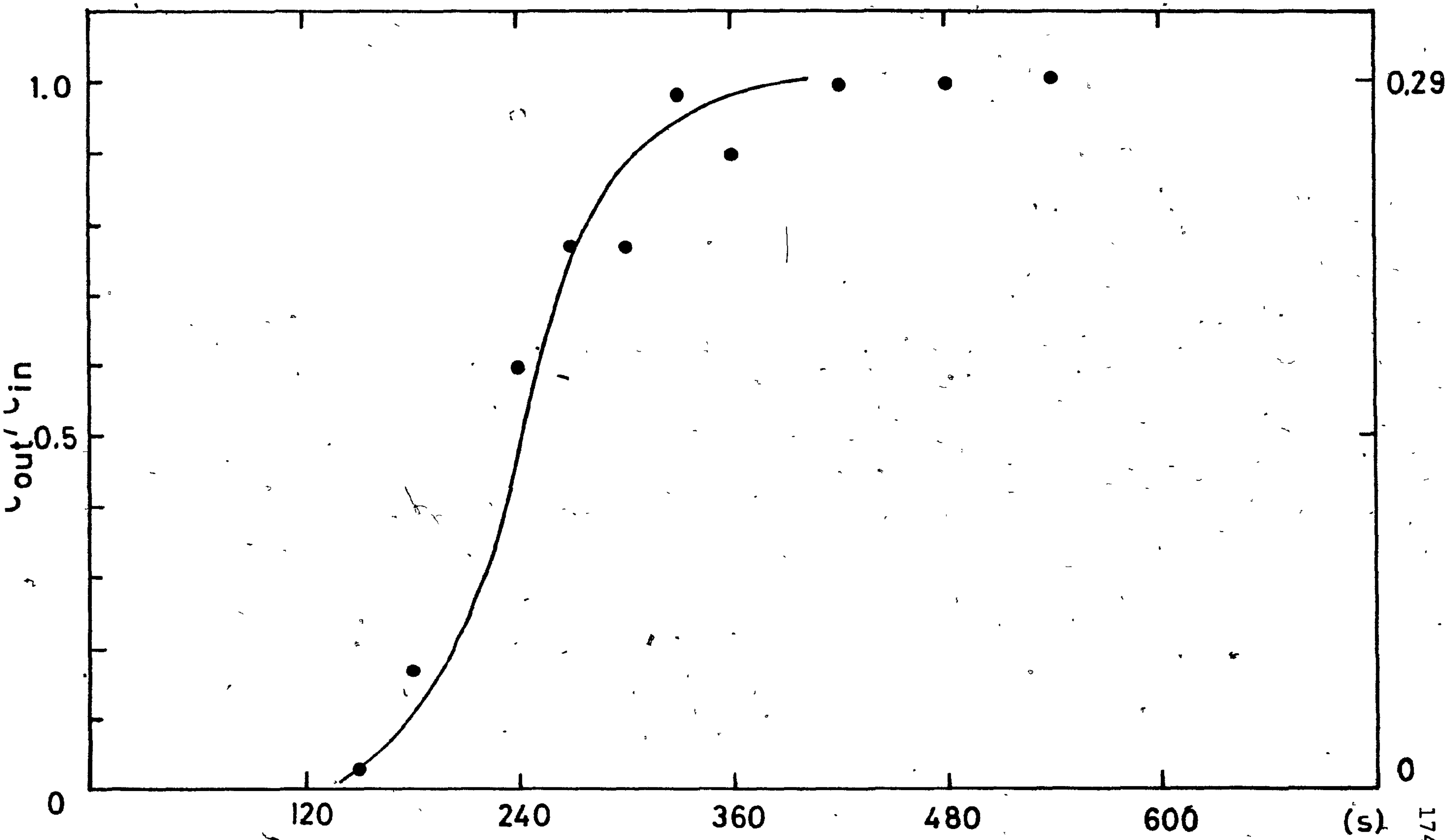

5-28 Breakthrough curve for synthetic NH_4 jarosite, electrolyte as fluid carrier, run 22. H_a=9.1kOe, U_∞=0.9cm/s.

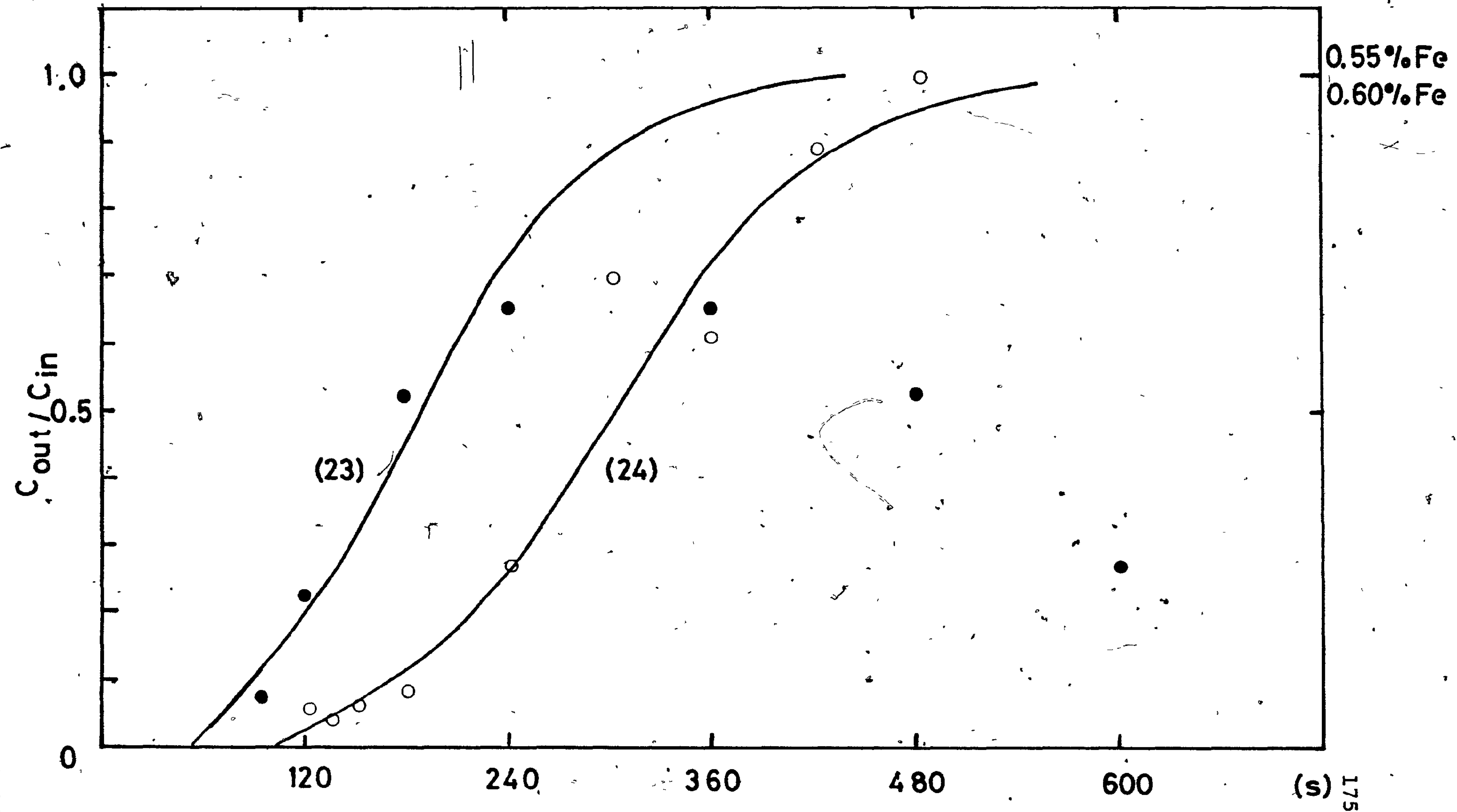

5-29 Breakthrough curve for synthetic α-FeOOH in electrolyte, run 23 and α-Fe_2O_3 in electrolyte, run 24. H_a=9.1kOe and U_∞=0.9cm/s.

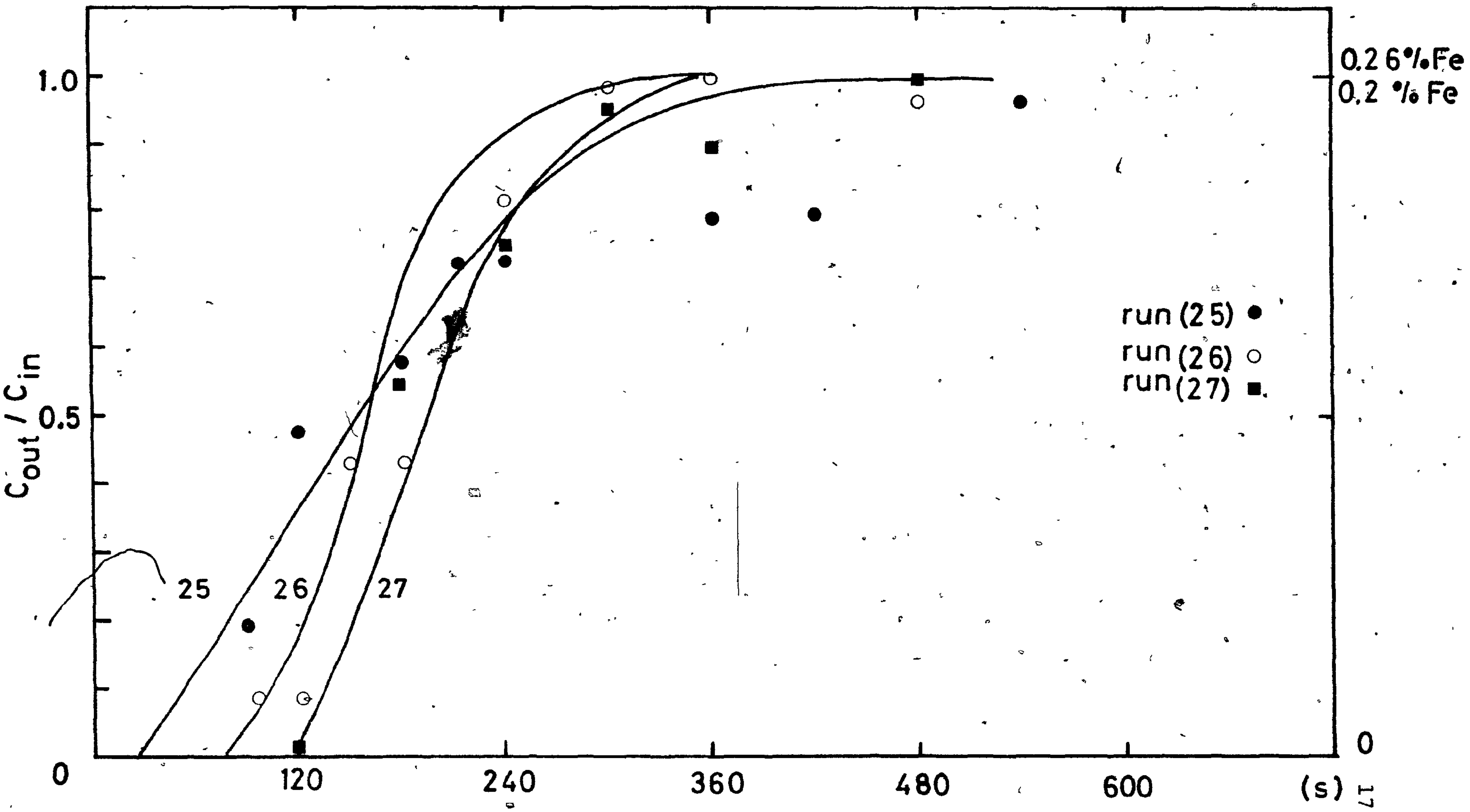

5-30 Breakthrough curve for clean CEZ jarosite in electrolyte, runs 25,26 (at 25^{o}C) and run 27 (at 75^{o}C). (25) H_a=4.2kOe, U_∞=0.9cm/s. (26),(27) H_a=9.1kOe, $U_\infty \cong$0.9cm/s.

Final filtration runs were made with CEZ thickener overflow samples, where slurry densities are considerably lower than those tested above and particle sizes are close to colloidal. Fig. (5-31) runs 28,29 indicate results of filtration tests with CEZ overflow samples at a field of 21 kOe in electrolyte at 25°C and 75°C. The ability to produce a clean electrolyte is evident with again improved performance obtained with electrolyte at elevated temperature.

In an industrial system, washing to remove entrapped electrolyte followed by backflushing of the matrix to remove trapped solids is an integral part of the filtration cycle. Table (5-12) displays the results of washing and backflushing on the loaded matrix of run 26. With the magnet left on the matrix was drained of slurry then backwashed for five minutes with water. Values of dissolved iron and zinc are presented as functions of washing time in the wash effluent. The volume of water used was 2.5l at a flow rate of 0.9cm/s. Solids removed from the matrix during washing were found to be considerably less than 1 gram. (less than 5% of collected solids). With the magnet switched off all solids were removed from the matrix by vigorous back-

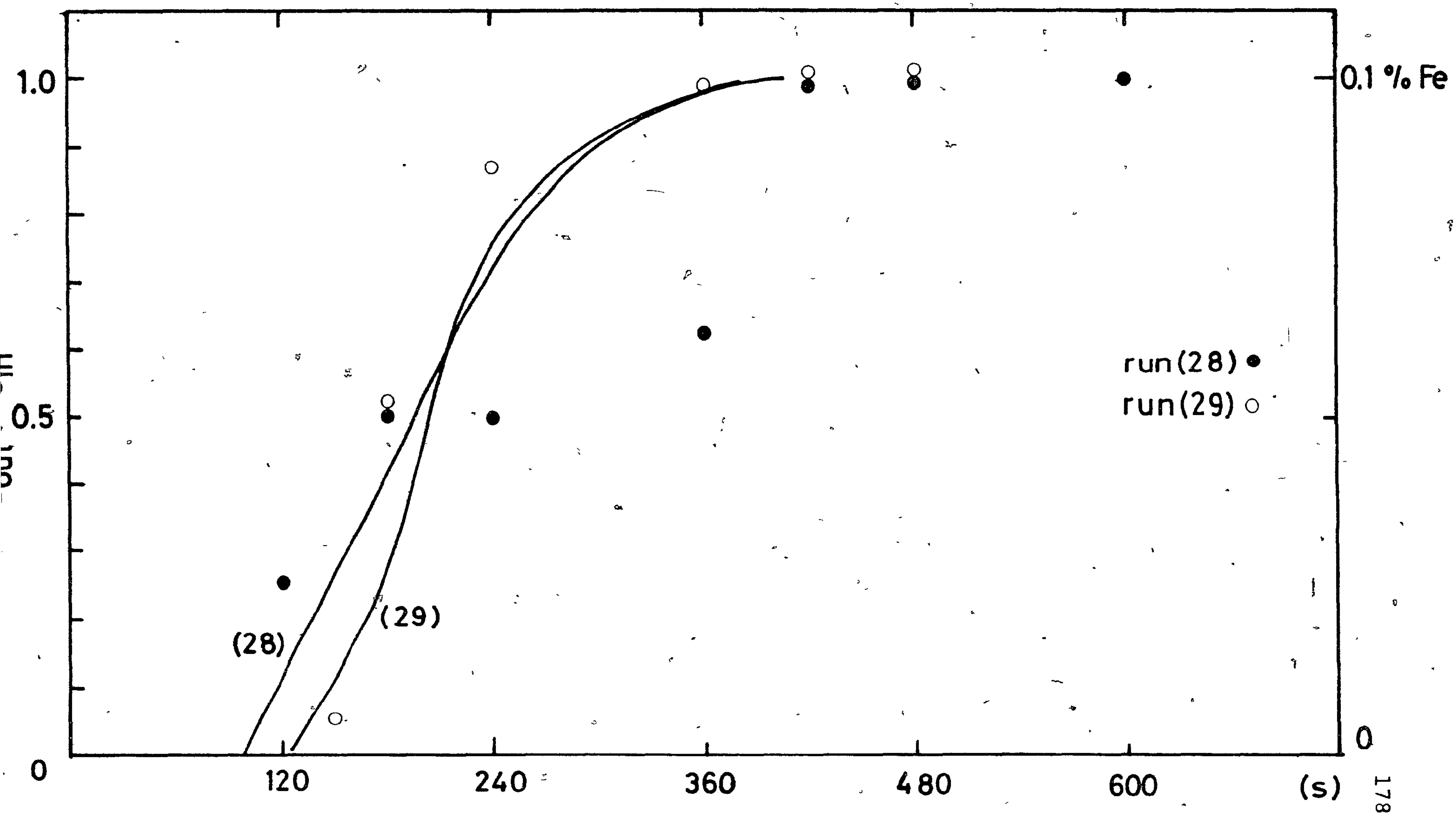

5-31 Breakthrough curves for CEZ jarosite thickener overflow, run 28 (at 25°C) and run 29 (at 75°C). H_a=21kOe, U_∞=0.9cm/s.

TABLE 5-12

Analysis of Backwash Effluent (run 26)

Time	Fe.g/L	Zn.g/L
15s.	0.18	6.12
30	0.75	12.62
60	0.50	11.50
90	0.37	6.25
120	0.25	4.75
180	———	2.25
240	———	1.50
300	———	0.50

flushing. A 2L flush was required to effectively remove all solids.

Two final filtration runs were made on electrolyte slurries containing solids considered to be highly magnetic. Run 31 (Table 5-11) shows the results of synthetic magnetite filtration. Full recovery of the magnetite was achieved at a low magnetic field and a relatively high processing rate with a 35g stainless steel mesh matrix. Run 32 indicates the results of the separation of ferrite phases from the CEZ jarosite slurry using the hgms technique. Previous separations had used the laboratory Davis Tube separator. A clear separation of highly magnetic phases from the weakly magnetic jarosite appears feasable. Table (5-13) denotes the results of weight distribution of the "mags" and "non mags" products, together with an analysis of zinc distribution. About 30% of the Zn is recovered to the "mags" product.

5.5 Magnet Sizing

5.5.1 The Collan Model

Initial sizing has been made using the results of synthetic material in order to study the influence

TABLE 5-13

Weight Distribution and Zinc Assay for Ferrite Separation (run 23)

	Weight (g)	Zn grade (%)	Zn distribution (%)
Mags	2.51	6.06	27.6
Non Mags	20.89	1.91	72.4
Calc. Feed	23.40	2.35	100.0
Head.	25.00	2.33	

of operating parameters. Fig. 5-32 shows the sizing results of runs 3,4 (Fig. 5-19) for synthetic potassium jarosite at processing rates of 1.2cm/s and 2.3cm/s. Volumetric flow rates, solids concentrations and magnet flush times were chosen to approximate the industrial situation The advantage of using filters of increased bed depth can be seen as a <10% change in surface area requirement occurs at bed depths of >2m even though processing rates are doubled. Similarly analysis of runs 11,12,13 (synthetic NH_4 jarosite) (Fig. 5-33) shows how the applied field only marginally reduces filter size areas at bed depths of 2m. Sizing does become sensitive when considering total matrix volumes. Large decreases in matrix volumes are observed with filters of short bed depth (<1m). In this region changes in field and flow parameters markedly affect matrix volume requirements with an almost 20% difference seen at bed depths of 0.5m when doubling either field or flow.

At this point it is important to consider the effect of operating parameters on t_f, the effective filtration time or the time of the filtration cycle. Tables 5-14,15 show how t_f changes with magnet size. Realistic

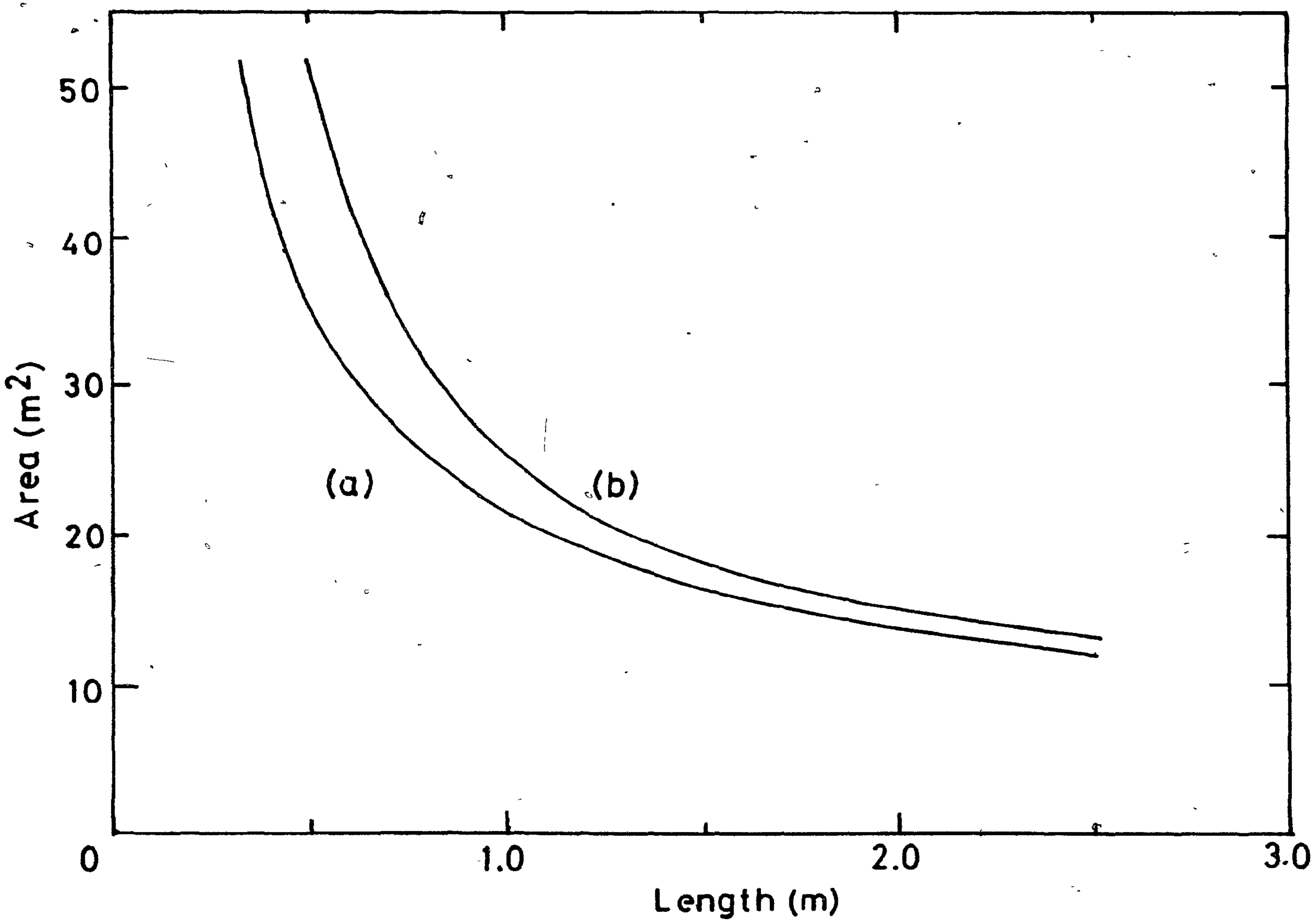

5-32 Magnet sizing curves for synthetic K jarosite (run 4) at processing rates of (a) 1.2cm/s. (b) 2.3cm/s.

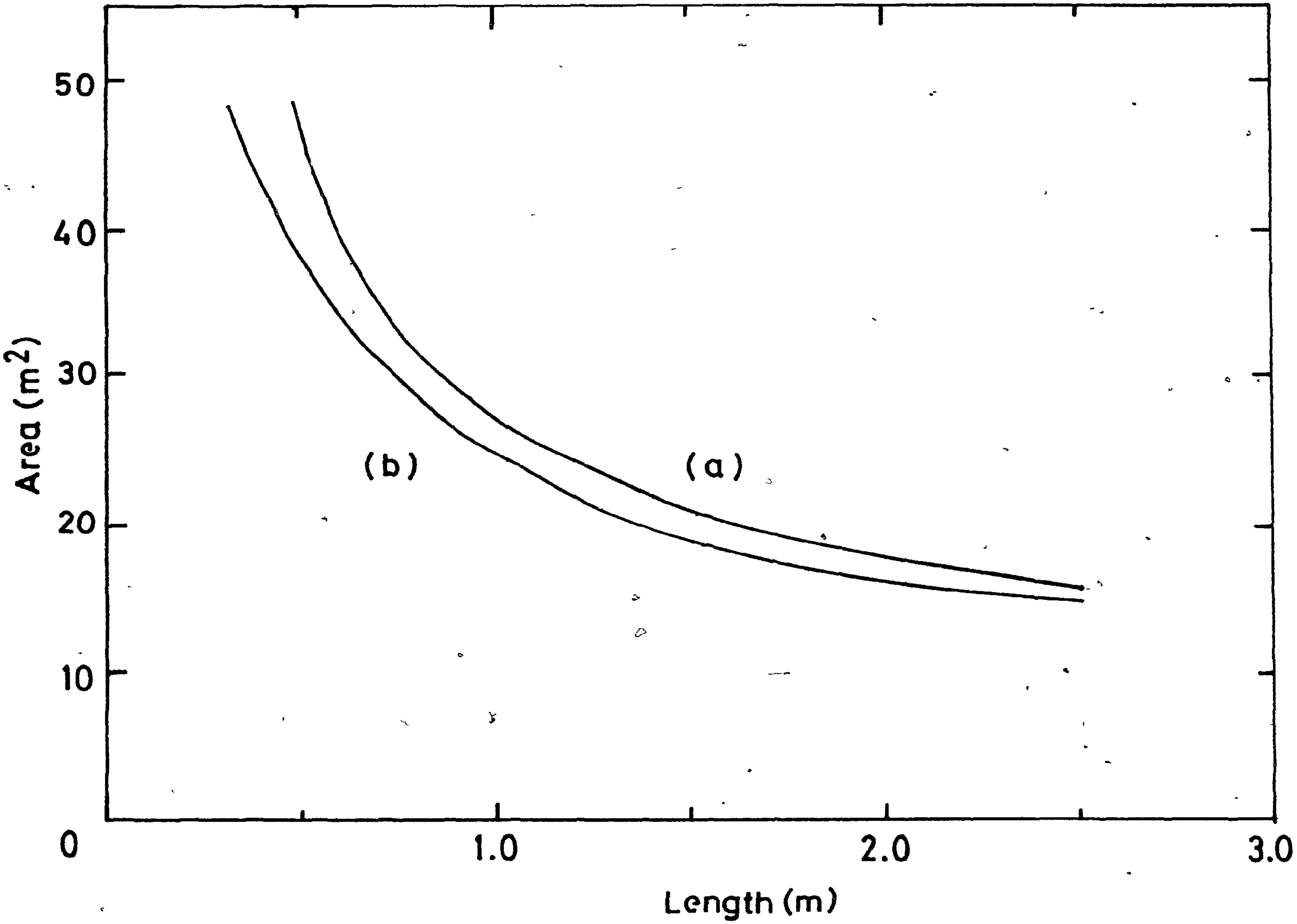

5-33 Magnet sizing for synthetic NH_4 jarosite, runs 11,12,13 applied field of (a) 4.2kOe and (b) 9.1kOe.

TABLE 5-14

Values of L, A and t_f for Magnet Sizing in Fig. 5-32

Run 3			Run 4		
L	A	t_f	L	A	t_f
0.1m	314m^2	6.99s.	0.1	183	23.6
0.5	5117	45.7	0.5	35.90	143.6
1.0	23.09	94.1	1.0	21.14	293.0
1.5	18.87	142.5	1.5	16.25	147.7
2.0	15.01	190.9	2.0	13.96	593.6
2.5	12.70	239.3	2.5	12.54	743.6

TABLE 5-15

Values of L,A and t_f for Magnet Sizing in Fig. 5-33

Runs 12,13			Runs 11		
L	A	t_f	L	A	t_f
0.1m	281.7m^2	20.4s.	0.1m	182.9m^2	31.9s.
0.5	46.6	148.3	0.5	39.4	39.4
1.0	27.2	308.8	1.0	24.12	24.12
1.5	21.0	469.0	1.5	19.10	19.11
2.0	18.1	629.0	2.0	16.6	16.63
2.5	16.3	789.0	2.5	15.1	15.14

filtration times for runs 3,4, (Table 5-14) are considered to be >10mins. This would only be achieved for the processing rate of 1.2cm/s and the process would benefit from reductions in V_0. Effective filtration times shown in Table 5-15 show how a large increase in t_f occurs with a corresponding decrease in magnet size when field strengths are increased. When calculating the number of magnets required for a particular process a balance between the total magnet area required and realistic effective filtration times must be struck.

Magnet sizing for the CEZ circuit is shown in Fig. (5-34), run 27. Values of C_{in} have been varied from 150g/L solids, curves (a,b), to 15g/L solids curve (c). Table 5-16 denote the calculated t_f values for both systems and indicates not only the considerable filtration capacity required to treat the 150g/L case but also the short cycle times. Curve (b) of Fig. (5-34) shows the effect of decreasing t_w, the estimated flushing time, from a value of 600s (considered to be realistic in batch magnet operations) to that quoted by Collan et al $^{(104)}$ of $t_w = 120$. The decrease in estimated magnet size shows clearly the importance of dilineating closely the t_w, especially when $t_w \approx t_f$.

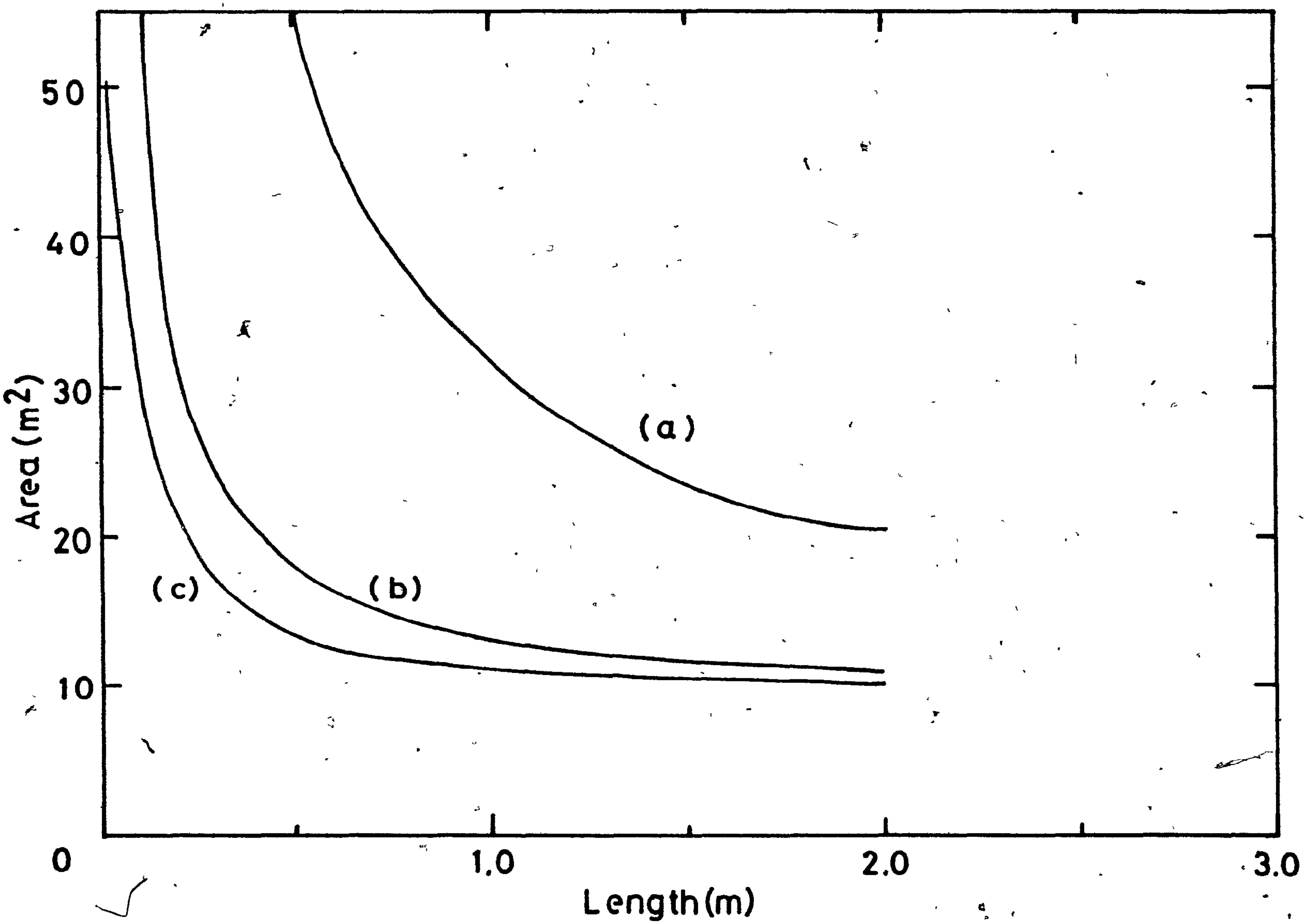

5-34 Magnet sizing for CEZ jarosite in electrolyte at 75°C, run 27. Curve (a) C_{in}=150g/L solids, t_w=600s, (b) C_{in}=150g/L, t_w=120s. (c) C_{in}=15g/L, t_w=600s.

TABLE 5-16

Values of L,A and t_f for Magnet Sizing in Fig. 5-34

(a) C_{in}=150g/L, t_w=600s. (b) t_w=120s. (c) C_{in}=15g/L, t_w=600s.

Run 27a		
L	A	t_f
0.1m	280m^2	20.1s.
0.5	54.2	123.7
1.0	31.2	253.3
1.5	23.7	383.0
2.0	20.1	512.6

Run 27b	
L	A
0.1m	63.4m^2
0.5	18.2
1.0	13.6
1.5	12.1
2.0	11.4

Run 27c		
L	A	t_f
0.1m	31.7m^2	247s.
0.5	13.5	1284
1.0	11.4	2580
1.5	10.6	3876
2.0	10.3	5173

Figs. (5-35,36) show magnet sizing for treatment of actual CEZ thickener overflow, run 29. Solids contents C_{in}, of 3g/L and 15g/l with C_{max} = 0.3g/L were assumed for sizing. In Fig. (5-35) sizing curves are shown with t_w = 600s curve (a) and t_w = 120s curve (b) for C_{in} = 3g/L. The effect of flushing time is considerably diminished as values of t_f, Table 5-17, are quite large. This is to be expected with such low solids concentrations being treated. Fig. (5-35) curve (c) shows magnet sizing for C_{in} = 15g/L solids and t_w = 600s for the same CEZ sample.

5.5.2 The Nesset Model

An example of filtration curves from the Nesset model is shown in Fig. (5-36), run 27. A comparison is made with the data fitted curve of Collan and the filtration curves predicted by the Nesset model. Particle size has been treated as an adjustable parameter in the Nesset model. It can be seen that the general curve features only approximate those experimentally determined, even though the curve is essentially data fitted. Small increases in the assumed particle size dramatically affect the position of the predicted curve. This results in a considerable increase in the effective filtration time.

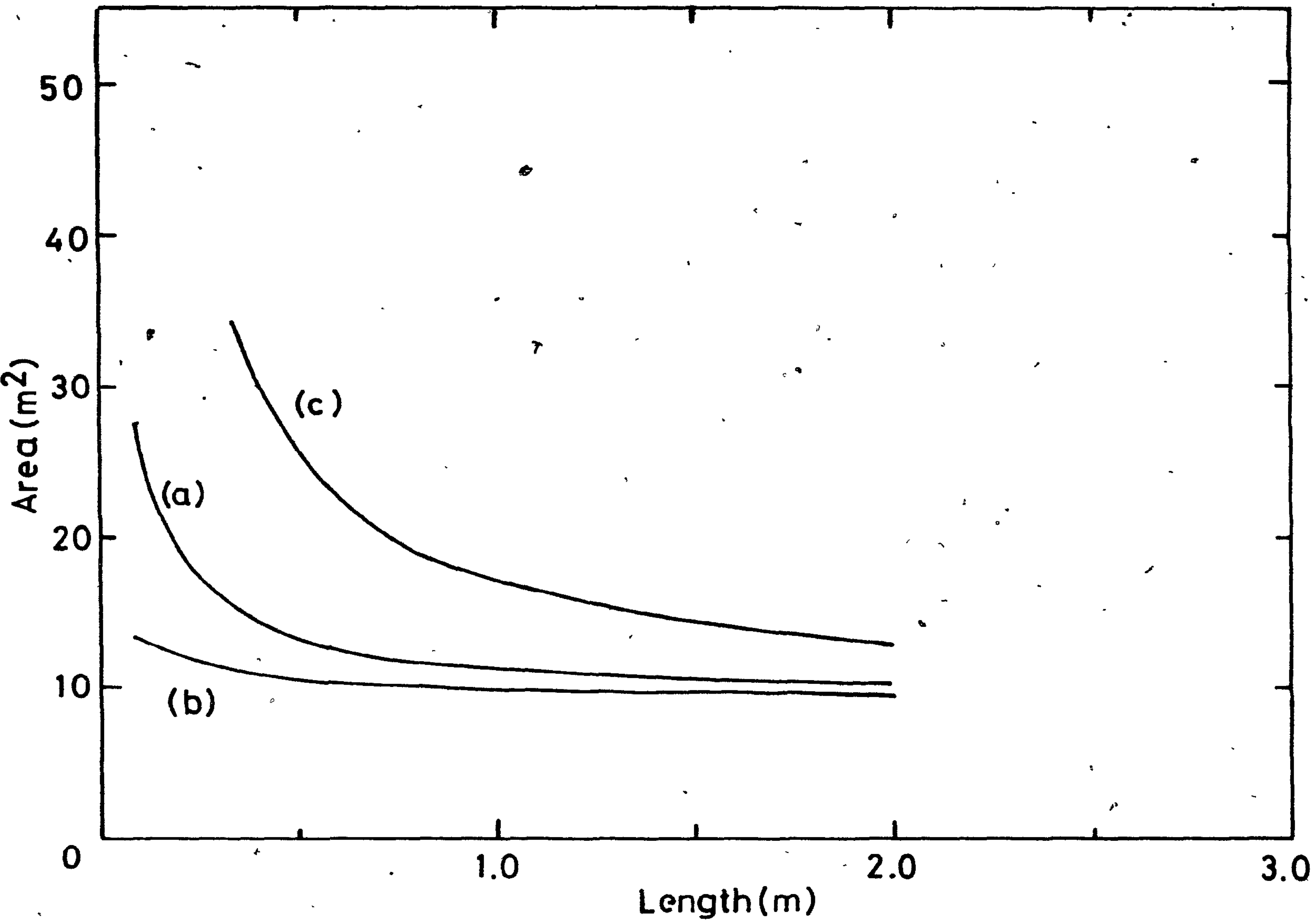

5-35 Magnet sizing for CEZ jarosite overflow sample, run 29. C_{in}=3g/L (a) t_w=600s, (b) t_w=120s, (c) C_{in}=15g/L, t_w=600s.

TABLE 5-17

Values of L,A and t_f for Magnet Sizing in Fig. 5-35 (run 29), C_{in}=3g/L, t_w=(a) 600s. (b) 120s. and (c) C_{in}=15g/L, t_w=600s.

	Run 29a		Run 29b		Run 29c
L	A	t_f	A	t_f	A
0.1m	27.0m^2	313s.	12.80m^2	52.7s.	114.5m^2
0.5	12.3	1822	9.86	354	24.95
1.0	10.75	3708	9.55	730	16.86
1.5	10.25	5594	9.45	1,107	14.27
2.0	10.00	7480	9.41	1,484	13.00

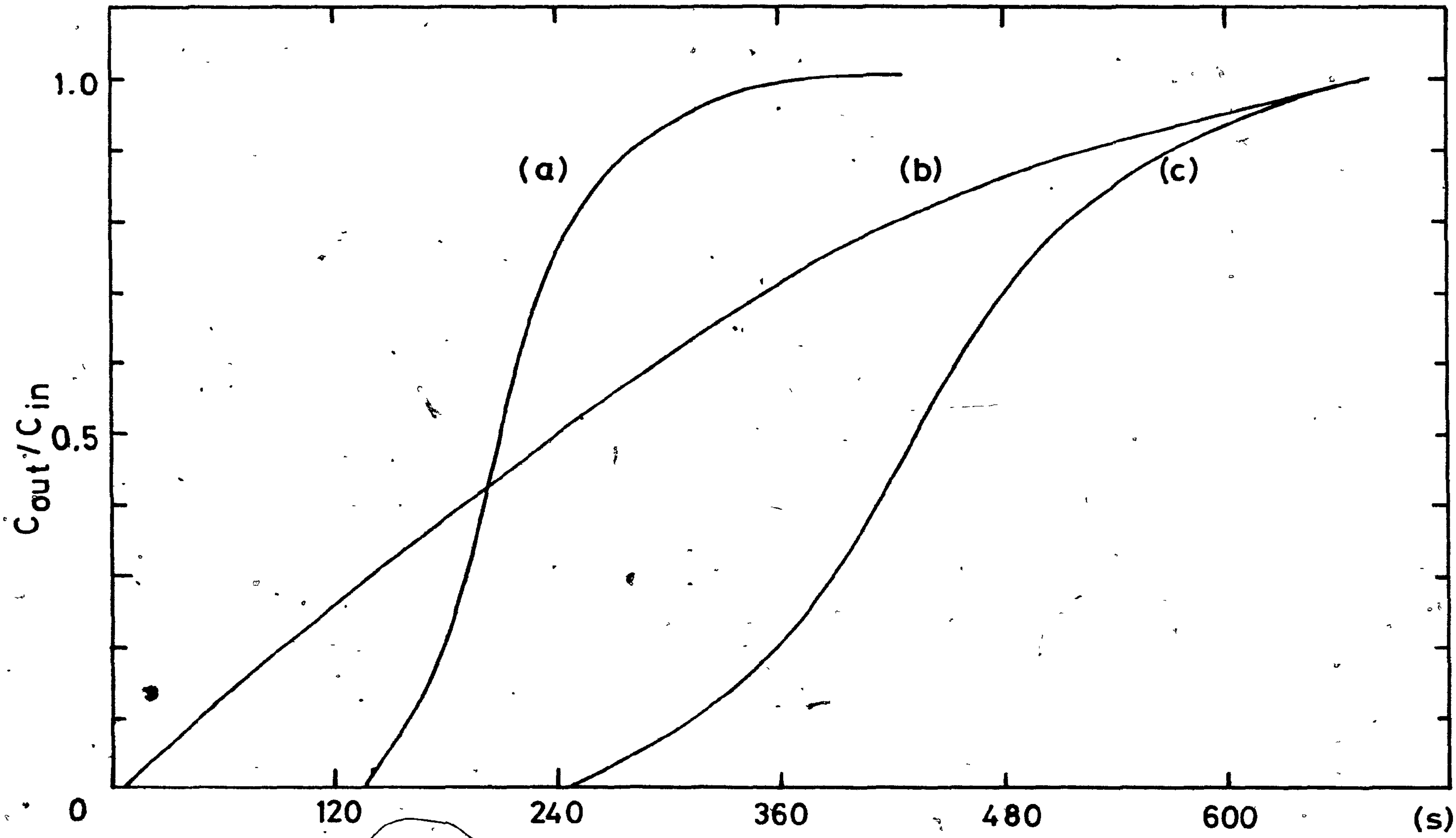

5-36 Breakthrough curves for CEZ jarosite, run 27 (a) Collan data fit (b) Nesset fit, b=1μm (c) Nesset, b=2μm.

Estimation of magnet size can be made from the Nesset model by applying equations 3-10,12,13. Using the experimentally determined parameters and a fitted particle size, matrix loading γ_m can be calculated, together with the maximum allowabled solids content in the feed L, for 100% recovery. The magnets are assumed to be of batch design and to operate on an hourly cycle, with an included 10min. wash time. A basic magnet unit size of diameter 2.60m was chosen as it approximates those commercially available.$^{(128)}$ Two cases are considered for treatment of CEZ thickener overflow as treated in the Collan approach of run 29, with C_{in} = 3g/L and 15g/L. Table (5-18) denotes the conditions for magnet sizing calculations. Table (5-19) shows for the Collan and Nesset approach the number of magnets required for the treatment of CEZ material in hot electrolyte of solids content 3g/l and 15g/l. Total magnet volumes required as predicted by the Nesset model are approximately three times less than those calculated from the Collan model.

TABLE 5-18

Parameter Values for Magnet Sizing Using the Nesset Model

(a) C_{in} = 15g/L solids (b) C_{in} = 3g/L solids

Measured Parameters

μ_f - 5.4
2b - 0.0001cm
ρ_p - 2.7g/cm
κ - 6.97x10^{-5}
M_0 - 0
f_b - 0.39
2a - 0.006cm
ρ_w - 7.75g/cm^3
M_s - 1472 emu/cm^3
K - 900 0e
ν - .013cm^2/s (stokes)
U_∞ - 0.9cm/s
ρ_f - 1.31
ℓ^2 - 3
H_a - 21 k0e
g - 980cm/s^2
A - 0.409

(a)	(b)
Q = 350,000L/hr	Q = 350,000ℓ/hr
L = 900,000g/hr	L = 4,500,000g/hr
t_w = 600s	t_w = 600s
N_L = 169	N_L = 169
γ_m = 1.71 g.solids/g.matrix	γ_m = 1.71 g.solids/ g.matrix
Magnets of unit size 2.6m diameter required = 2 x 13cm depth	Magnets of unit size 2.6m 2 x 65cm bed depth

TABLE 5-19

Calculated Magnet Numbers Required from Nesset and Collan Models Based on a Magnet Unit Size of 2.6m Diameter

C_{in}	Collan	Nesset
15g/L solids	3 x 1.1m. ($17.5m^3$)	2 x 0.65m. ($6.9m^3$)
3g/L solids	2 x 0.4m. ($4.24m^3$)	2 x 0.13m. ($1.4m^3$)

Magnet Operating Conditions

C_{max} = 0.3g/L solids

t_w = 600s.

H_a = 21kOe

U_∞ = 0.9cm/s

Q = $300m^3/hr$

VI. Discussion

6.1 Precipitate Analysis

The agreement of the X-ray diffraction patterns and differential thermal analysis curves with previously reported data, conclusively supports the procedures used to produce the precipitate phases. Synthetic NH_4 jarosite showed better crystallinity than that produced industrially, as evidenced by the sharper diffraction patterns obtained. This observation is most likely due to the contamination of the industrial precipitate not only by retained zinc but by slight hydronium ion substitution for the ammonium ion in the lattice.(55) Although potassium and sodium jarosite are the preferred species over hydronium jarosite, the substitution may take place during solidification when a number of solid solution compounds are being formed.

Identification of goethite was facilitated by an unexpectedly high degree of crystallinity in the precipitated phases. Indeed, for the case of β-FeOOH, well defined diffraction patterns were obtained and the difficulties described by Scott and Davey (63) were not encountered. As the experimental techniques were identical the strict control over reagent addition, temperature and pH exercised here could be critical in the production of well crystallised β-FeOOH. The reaction peaks for both α and β-FeOOH phases obtained from differential thermal analysis, although not identical in temperatures of reaction to those found by the above workers, still lie well within the range of the other reported values. (109,110) The anomolies are attributable to the likely difference in particle size (a common problem in the repeatability of DTA curves).

6.2 Particle Magnetisation

The ability to accurately determine susceptibility values of materials without the need to use sophisticated magnetometers has been extended by use of the.wet Frantz system. Comparison of the measured susceptibility values with those of the magnetometer showed excellent agreement. This indicates that the force balance model developed for the dry system appears to hold equally well for the wet Frantz. The advantage of the latter technique is the ability to treat material of much smaller particle size than that recommended for the dry system. (113) Precipitates with a size distribution below 10μm can be handled adequately (if somewhat laboriously due to the slow processing rates required). With liquid as a particle carrier the difficulties encountered by Nesset (112) when processing very small particles in the dry system, are not encountered.

The synthetic jarosites all display similar susceptibilities (Table 5-8). Further, synthetic K jarosite gave a value close to that reported for natural K jarosite, $7.3\text{x}10^{-5}$emu/cm^3Oe. (122) The slightly lower value for CEZ jarosite can be attributed to the impure nature of this precipitated phase, as previously discussed.

The Frantz generated data for hematite susceptibilities demonstrates the Frantz method can yield information on materials which are magnetically complex. There is good agreement in both the measured values of χ_∞($28\text{x}10^{-6}$emu/g Oe) (Table 6-1) and that reported by Pastrana and Hopstock (42) for reagent grade hematite and Nesset and Finch, (112) for a natural specular hematite. The differences in values of spontaneous magnetisation measured by the magnetometer and Frantz may be due to orientation effects. (112) Particles passing through the Frantz device are allowed to freely orient in the crystal direction of maximum magnetisation, while in the magnetometer the powder is randomnly packed and particles cannot orient. This results in values of σ_0 (Frantz) being greater than values of σ_0 (Foner). In the present work σ_0(Frantz) = $\frac{2.7}{2}$ σ_0(Foner). This is somewhat larger than that found by Nesset and Finch where σ_0(Frantz)

TABLE 6-1

Magnetisation Data for α-hematite.

	χ_∞ emu/g.Oe x 10^6	σ_o emu/g.
Wet Frantz	28.4 ± 6	0.110 ± .04
Pastrana & Hopstock(42)	32.4 ± 7	0.38 ± 0.17
Nesset & Finch(112)	23.2 ± 6	0.25 ± .03

χ (mass susceptibility) = $\frac{\kappa}{\rho}$

$= \frac{3}{2.5} \sigma_0$ Foner. For particles fully able to orientate, theoretically $\sigma_0(\max) = 3/2\sigma(\text{average})$, (123) which is close to the value found in the present study. This suggests that the wet system allows the particles to orient even more freely than in the dry system. Magnetic data obtained from the Frantz is felt to be more applicable to hgms as both systems allow particles to freely orient within the magnet.

Measured volume susceptibilities for both goethite samples are in good agreement, Table (5-7), with the reported value by Hoferet al(124) of $1.3\text{x}10^{-4}$ emu/cm^3 for a similarily precipitated goethite. There also appears to be little difference in susceptibility values between the two phases of goethite under investigation. The magnetisation curves produced by the magnetometer for both $\alpha + \beta$ phases did not show any field dependancy for susceptibility. This is contrary to the work of Pastrana and Hopstock (42) for naturally occuring goethites. It is likely that this reflects the freedom from ferromagnetic impurities which sometimes occurs in natural goethite samples.

6.3 Particle Size Analysis

The size distribution of all precipitate samples is shown in the Sedigraph data Table (5-6) and corresponding electron micrographs (Figs. 5-8→18). The sedimentation technique can suffer from flocculation though considerable effort was made to prevent this. This may account for the apparently smaller particles indicated in the micrographs. CEZ jarosite particles Figs. (5-8,9) are considerably smaller and less well defined than those produced synthetically. Although general reaction parameters are the same, the presence of high quantities of dissolved Zn metal ion may be a factor in determining particle size. Dutrizac$^{(125)}$ has indicated that jarosite particle sizes do not generally exceed 10μm. Some particles are observed, Figs. (5-10,11), as large as 20μm. These particles are clearly composed of intergrowths of smaller crystals. The inability to discern particle size unambiguously affects the application of the Nesset model in predicting breakthrough curves. In contrast the approach of Collan et al requires no knowledge of the experimental parameters in determining filter performance.

6.4 Filtration

6.4.1 General Comments

The general features of all the magnetic filtration breakthrough curves are similar to those obtained from more conventional filtration processes. The form is of the expected exponential type. The curves are not symmetrical, however, as the condition $C_{out} = C_{in}$ (i.e. full loading of the matrix) is not entirely dependent on magnetic factors. Physical entrapment of material is inevitable and sloughing off and recapture of this material is possible. This effect is emphasized by the data fitted curve which is based on a fitting of only the central portion of the experimentally determined breakthrough curve. The fitted curves tend to approach saturation more quickly than found experimentally. While physical entrapment is of interest as an explanation of the long tail in the breakthrough curve the present work is not concerned with this latter stage since it is of no practical use.

The general experimental technique of the study appears to be validated by the repeatability of filter performance as exhibited in runs 8,9 (Fig. 5-21), runs 12,13 (Fig. 5-24) and runs 14,15 (Fig. 5-25). Run 30 (Fig. 5-22) is similar to run 9 (Fig. 5-22) except that slurry was passed through the matrix prior to energizing the magnet. Fig. (5-22) shows this procedure gave shorter filtration times. This can be explained by the instantaneous capture of material already present in the matrix at the time when filtration is initiated. However there appears to be little effect on the value of K. Since K measures the speed with which the saturation front moves through the matrix - this should not change because of capture of material already present, run 30 compares with run 9. For constant values of t_0 increasing K values will steepen the breakthrough curve, shown by comparing run 17 (t_0=364s., K=6.55; Fig. (5-25)) and run 20 (t_0=342s, K=12.18; Fig. (5-26)).

6.4.2 Filter Performance of Precipitates

A comparison of the general filter performance of synthetic jarosites, Fig. (6-1), reveals great similarity. This is not entirely surprising as the major physical properties of the precipitates are similar. The greater filterability of K jarosite is due most likely to the larger particle size encountered with this precipitate. Comparison of the Fe_2O_3 and FeOOH curves Fig. (6-2) shows again how precipitates of comparable properties behave similarily in the magnetic filter. Of all the precipitates it does appear that hematite gives the best filterability, a factor which may be of interest in future selection of iron precipitation routes.

The effects of filtration parameters appear to be common to all the precipitates tested. Changes in field strength, Fig. (6-3), shows how effective filtration time increases in

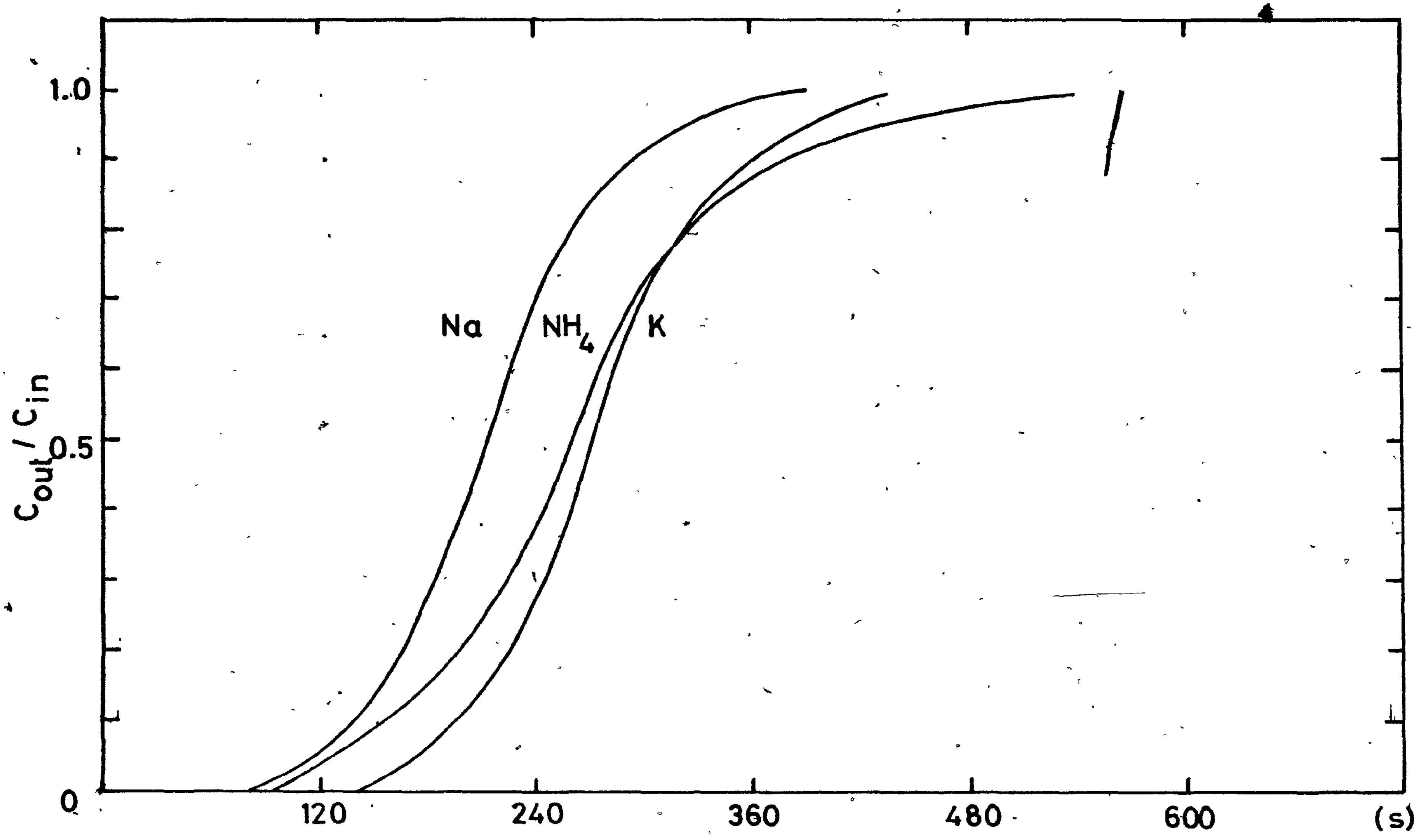

6-1 Comparison K,NH_4,Na jarosite breakthrough curves. H_a=4.2kOe, U_∞=0.9cm/s, in H_2O.

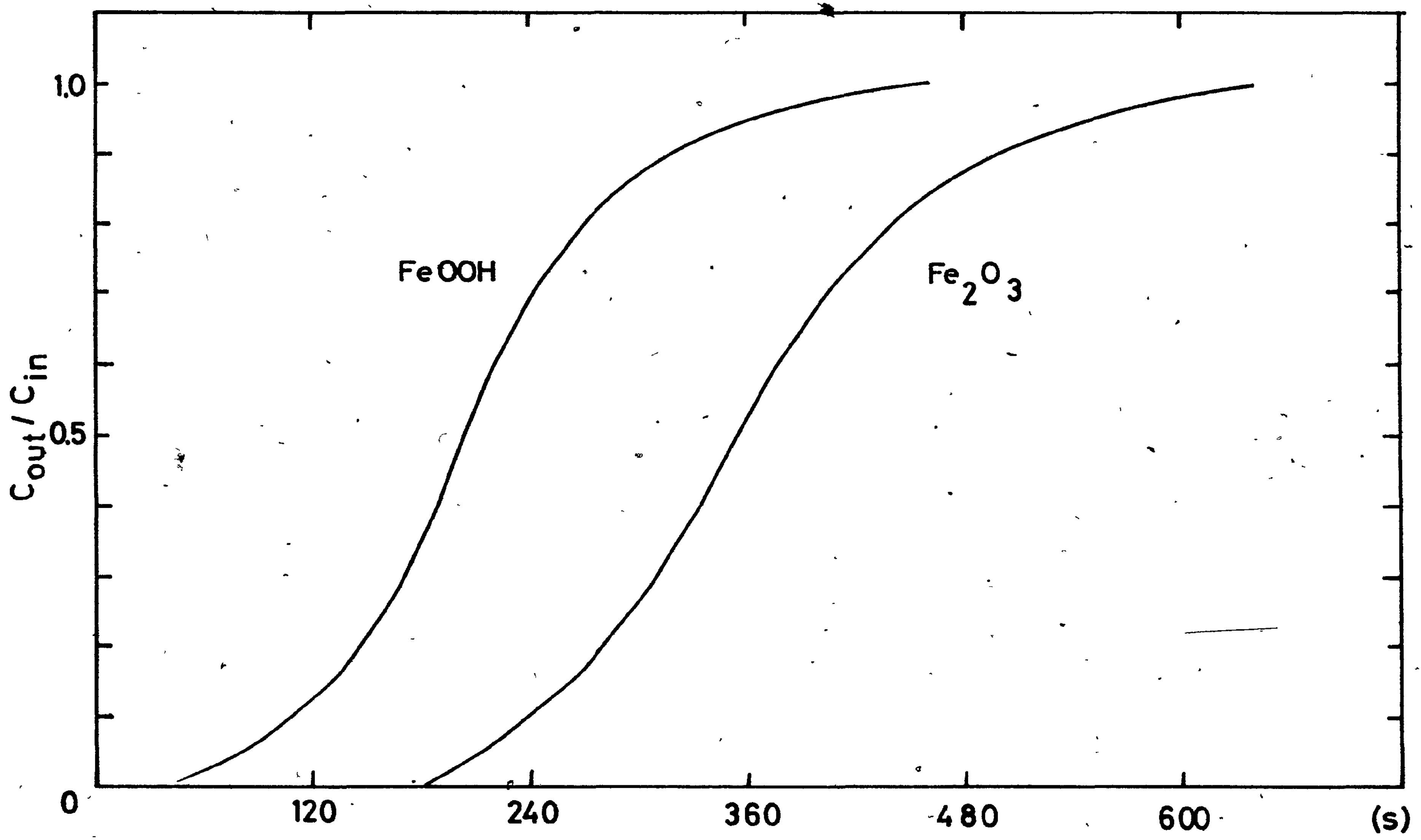

6-2 Comparison of FeOOH, Fe_2O_3 breakthrough curves.
H_a=9.1kOe, U_∞=0.9cm/s, in H_2O.

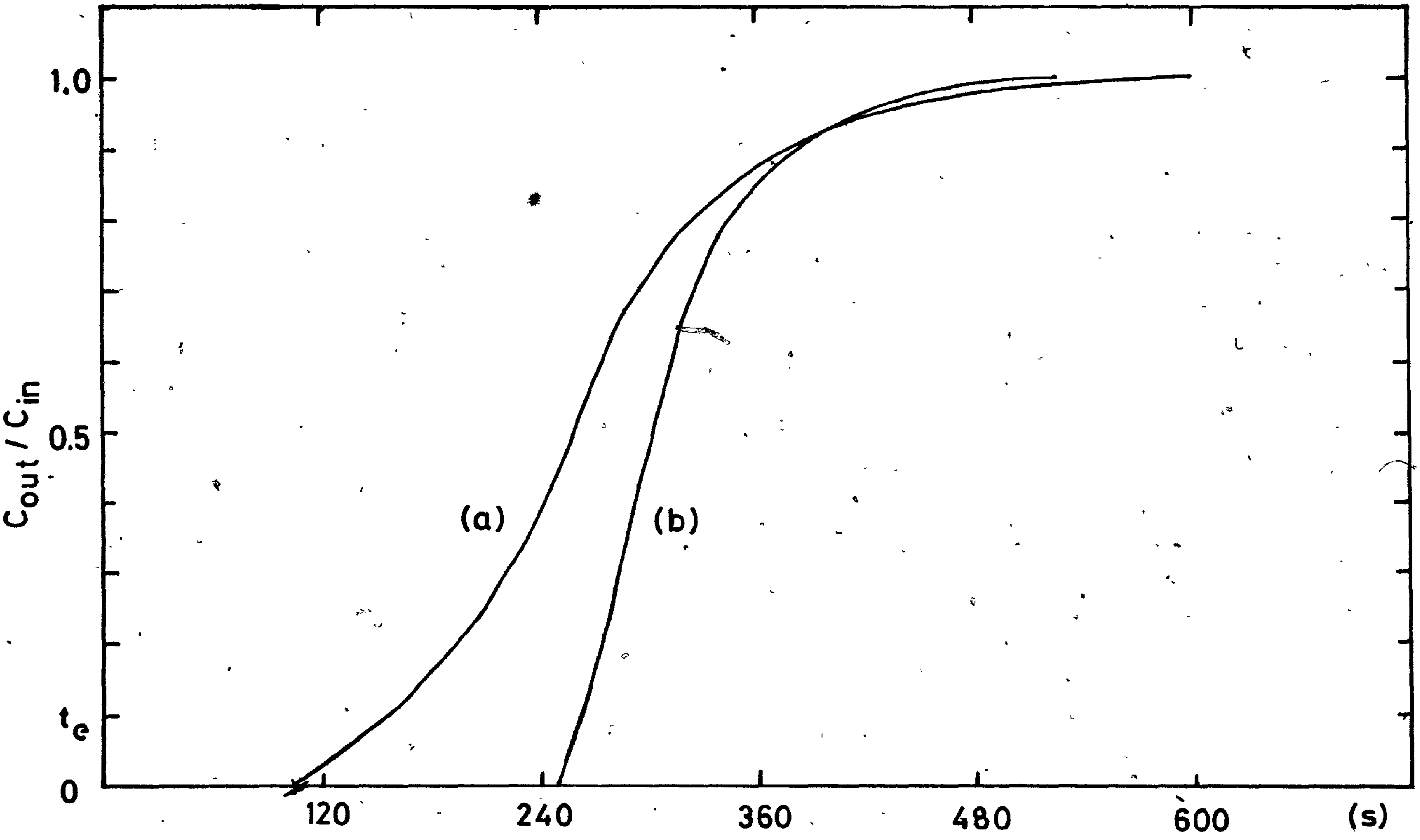

6-3 Effect of field on breakthrough curves of NH_4 jarosite in H_2O. (a) H_a=4.2kOe, U_∞=0.9cm/s. (b) H_a=9.1kOe, U_∞=0.9cm/s.

proportion to the field. This relationship is likely only up to field strengths of about 10kOe. Beyond this field, matrix filaments become magnetically saturated and the rate of increase of magnetic force with field decreases.(126) The expected decrease in filter efficiency by increasing the flow rate of material through the matrix is demonstrated in Fig. (5-19). The filtration process is clearly sensitive to only moderate changes in slurry velocity. Similar decreases in filter efficiency are evident when considering the viscosity of the liquid carrier. Fig. (6-4) shows the poorer filtration performance of CEZ jarosite in fluid media of increasing viscosity. The detrimental effects of both increasing fluid velocity and viscosity are predictable when considering the increased effect these parameters have on the fluid drag forces (Equation 3-8). There is not sufficient data to model changes in t_0 or K with the operating parameters of field, fluid flow and viscosity.

6.4.3 Using the Nesset and Collan Models in Magnet Sizing

The general observations made concerning the role of the parameters on magnetic filtration are predicted by the Nesset model (section 3.2.3). However, the ability to use the calculated values of N_L for either magnet sizing or describing the magnetic filtration breakthrough curve is

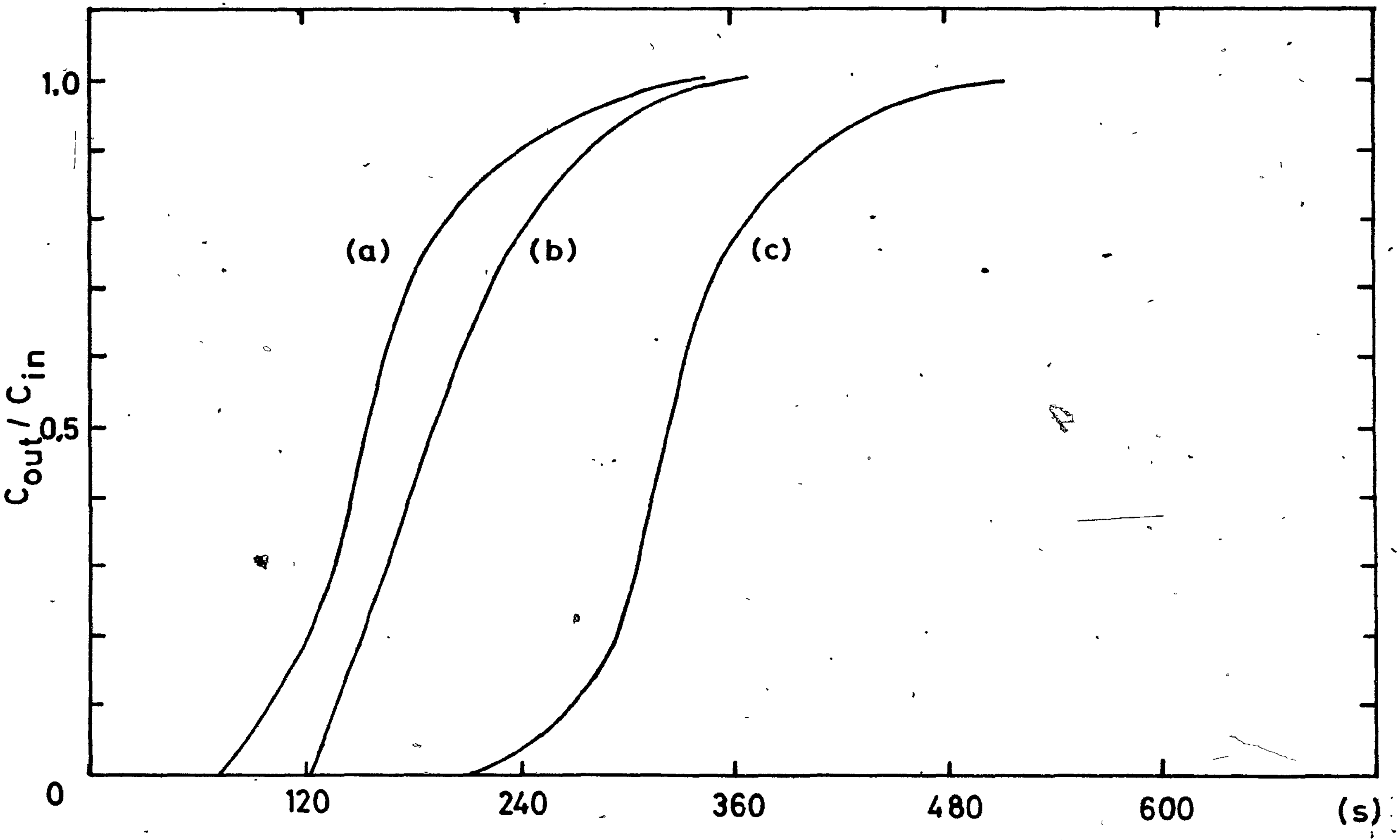

6-4 Effect of viscosity on breakthrough curves of CEZ jarosite, H_a=9.1kOe, U_∞=0.9cm/s. (a) Electrolyte at 25°C. (b) Electrolyte at 75°C (c) H_2O at 25°C.

severely limited in the present study. One principal reason is the low wire Reynolds numbers encountered. A limitation in the model is associated with the development of the boundary layer equations where wire Reynolds numbers are assumed to be much greater than unity. The situation in the present study of low flow rates, high viscosity fluids and fine matrix wires leads to Reynolds numbers <0.5. A second problem is the wide size range of the particles, only a single size is entered in the Nesset model. The limitations in simulating breakthrough curves are illustrated in Fig. (5-36), where comparison is made between the data fitted curve of Collan and the predicted filtration curve of the Nesset model. The small increases in the assumed particle size dramatically affect the position of the predicted curve, resulting in considerable increases in the values of t_e and t_0. In principle it would be possible to divide the feed material into size increments and sum over the distribution. However this would require a major revision of the Nesset model.

The effect of the breakdown of the model is demonstrated in calculating values of N_L when attempting to size magnets for the CEZ circuit. An overestimation of matrix loading γ_m is made, resulting in a considerable underestimation of the matrix volume required, Table (5-19).

The simulation of filter curves using the Collan approach appears to lend itself to the present study by allowing uncertainties in particle parameters to be ignored. Similarily, anomolies in the physics of the capture process in the magnetic filter can also be ignored by employing this "black-box" approach to sizing.

Although simulation of breakthrough curves uses a data fitting technique the model allows considerable flexibility in determining magnet sizes, as evidenced in the sizing of the CEZ circuit. Limitations in the model exist only when considering the accuracy of the data fit. (Appendix 5) This is minimized by considering only the linear portion of the breakthrough curves in the regression. Poor fit occurs when the number of degrees of freedom is small.

A comparison of the actual filter numbers required for various filtering conditions, expected in the CEZ circuit, is presented in Table (5-19) together with estimates using the Nesset model. It is apparent from the Nesset model that when sizing filters, considerable attention should be paid to the behaviour of the model. While it is clear that a fundamental model based on physical parameters and the physics of the capture process would be a more powerful tool in the accurate sizing of magnet systems, the data fitting method of Collan et al is preferable at this time.

6.5 Metallurgical Applicability

The ability to filter precipitates of fine particle size and relatively weak magnetic susceptibility from an electrolyte medium by high gradient magnetic filtration technique appears feasible. The applicability of the technique to a variety of iron precipitates has been demonstrated. It appears however that replacement of conventional filtration systems handling high solids volume slurries is not a viable option as the magnet volume required would be prohibitive.

Magnetic filtration as applied to the zinc industry would best be used to augment the conventional thickening capacity. Any required increase in capacity could be met by hgms polishing of a dirty thickener overflow.

The expansion of iron removal systems appears inevitable as the quality of treated ores deteriorates. A major problem in the zinc industry is increased pyrite contamination of zinc concentrates. This is directly associated with increased ferrite formation during roasting.[127] Pyrite removal by conventional mineral processing techniques is limited by the fine grain structure of many ores now being encountered. This is particularily true of the concentrates from New Brunswick ores which are treated at the CEZ Valleyfield plant. An increase in dissolved iron levels will consequently demand increases in precipitate removal systems. Plant expansion can be minimized by maintaining the present thickening capacity but allowing a higher degree of solids contamination in the overflow. Magnetic filtration can then be applied as a final polishing step, effectively increasing thickener capacity but not at the expense of large increases in required plant area.

An important aspect of the filtration procedure in the zinc industry is the recovery of retained electrolyte from the filter cake. In magnetic filtration systems entrapped solids can probably be readily washed and electrolyte recovered because of the open matrix structure. Some indication of this is given on Table (5-12). However, on a small scale it is difficult to discriminate between liquid held by the filtered solids and that held in the piping. It is also possible that final slurry densities obtained from backflushing the matrix can be considerably increased by using air/water mixtures during solids removal.

In magnet sizing for the CEZ jarosite, maximum solids concentrations in the effluent have been assumed to be relatively low, i.e. 0.3g/L solids, in order to demonstrate the high degree of filterability of this precipitate, while the the treatment of the total electrolyte volume produced by the leaching/precipitation circuit of 300m^3/hr has been assumed. Operating practice at the CEZ Valleyfield Plant Quebec, is such that final jarosite thickener overflow contains 3g/L solids at a production of 100m^3/hour. The magnet sizing curve to treat an expected dirty thickener overflow containing 15g/L solids, as predicted by the Collan model, is shown in Fig. (6-5). Two magnets of diameter 2.6x0.35m depth would be required for the CEZ circuit. The positioning of these magnets is shown in a proposed flow sheet for thickening/filtering system, Fig. (6-6).

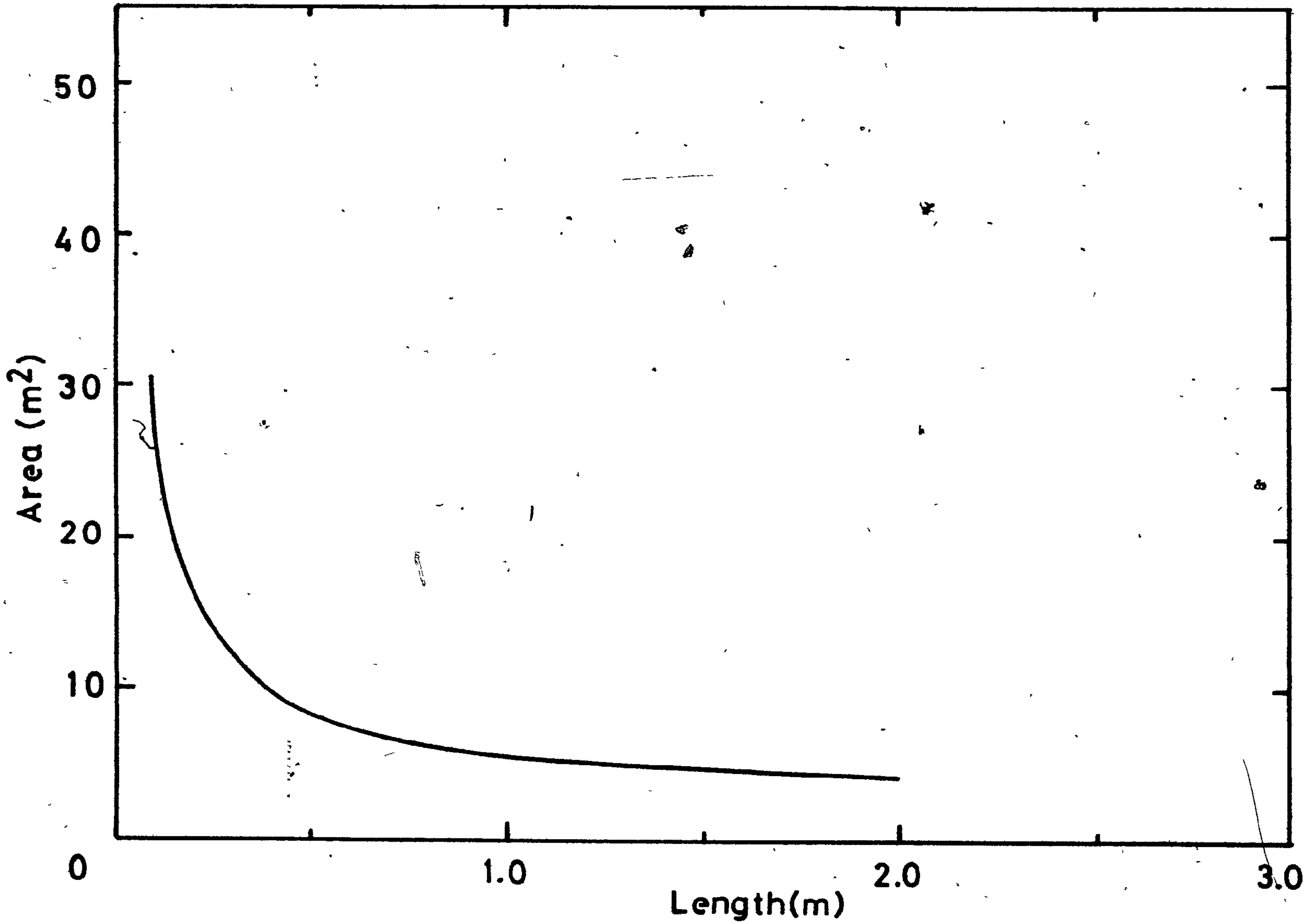

6-5 Magnet sizing for CEZ Valleyfield jarosite overflow, C_{in}=15g/L solids, C_{max}=3g/L solids.

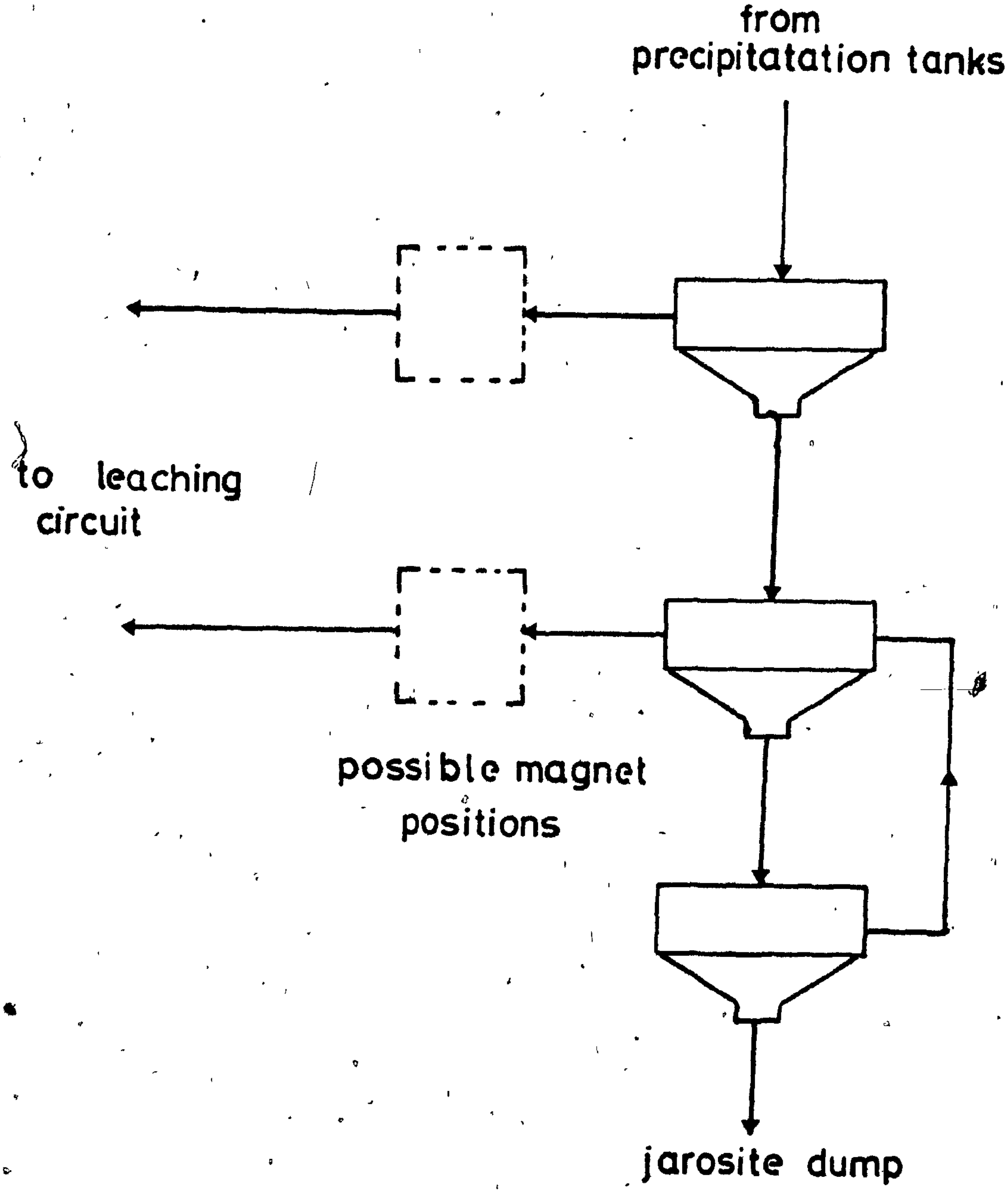

6-6 A proposed flowsheet for the augmentation of a conventional filtering system found in the zinc industry.

VII. Conclusions and Future Work

7.1 Conclusions

1. The magnetic filtration of a variety of synthetically produced iron precipitates from water and zinc electrolyte has been demonstrated. Filtration efficiency is increased at low flow rates (<2cm/s.) and high background fields (>5kOe)

2. α-hematite is probably the most readily filtered precipitate

3. The laboratory precipitated, iron phases are in good agreement with those produced by other workers. In the case of β-FeOOH a more crystalline phase was produced than previously found.

4. The ability of a wet Frantz to measure the magnetic susceptibilities of particles in a background carrier fluid has been demonstrated. CEZ Zn electrolyte was shown to have no magnetic effect. The magnetic susceptibility of CEZ NH_4 jarosite was measured in zinc electrolyte as $\kappa = 6.97 \times 10^{-5}$ emu/cm^3.Oe. Other iron precipitates all had similar susceptibilities ranging from $7.9 \times 10^{-5} \rightarrow 15.5 \times 10^{-5}$ emu/cm^{3}Oe.

5. The simple Collan filtration model adequately reproduces

the experimental breakthrough curves. An indication of physical effects of the filtration process is shown by the lack of correlation of model and experimental curves when matrix saturation is approached.

6. The inability of the Nesset model to predict matrix loading and associated breakthrough curves is a result of (a) the low wire Reynolds numbers encountered in the present system and (b) a very wide particle size range.

7. A preliminary sizing of the magnets for treatment of CEZ jarosite thickener overflow, determined that for a volumetric flowrate of 100m^3/hr solids content 15g/L, 2 magnets of 2.6m diameter and 0.35m bed depth would be required to lower solids content to <3g/L.

8. Recovery of unreacted ferrites associated with industrial zinc precipitation systems is feasible using a magnetic separation technique.

7.2 Claims for Original Research

1. Magnetic susceptibility determinations for synthetically produced NH_4,K,Na jarosite have been attained together with values for an industrially produced NH_4 jarosite in the presence of background electrolyte.

2. The magnetic filtration of iron precipitates has been demonstrated from both water and electrolyte.

3. The magnetic filterability of industrial jarosite precipitates from zinc electrolyte has been demonstrated.

4. Ferrite removal from the CEZ jarosite residue is possible using only low intensity magnetic separators.

7.3 Future Work

1. A further investigation of the reclamation of zinc ferrite phases from discarded jarosite precipitate systems should be made.

2. A refinement of the Nesset model allowing size distribution to be incorporated when calculating matrix loading would be useful.

3. Testing of the Nesset model in predicting filtration breakthrough curves in systems where $Re_W>1$ would better test this physical approach to magnet sizing.

4. Sizing of hgms is still uncertain. In the Collan approach the constancy of the constants l_0 and C_s with filter length should be tested. Relationships between ℓ_0, C_s, matrix packing, V_0 and H_0 are required to interpolate for optimizing design and operating conditions.

5. The feasibility of thickener overflow polishing should be examined using CEZ as a model.

BIBLIOGRAPHY

1. Taggart, A.F., "Handbook of Mineral Dressing", John Wiley and Sons, New York 1954.

2. Oder, R.R., Proc. HGMS Symposium, M.I.T., May 22, 1973, Eds. Oberteuffer, J.A., Kelland, D.R., p.55.

3. Price, C.R., Abercrombie, W.F., Industrial Applications of Magnetic Separation, Liu, Y.A. (Ed.), IEEE Publication No. 78CH1447 - 2MAG, N.Y. (1979) p.14.

4. Trindade, S.C., Procedings of the High Gradient Magnetic Separation Symposium, M.I.T., Cambridge, 1973, p.102.

5. Oberteuffer, J.A., Wechsler, I., Marston, P.G., McNallon, M.J., IEEE Trans. Mag. Vol. Mag-II, No. 5 Sept. 1975, p.1591.

6. Arvidson, B.R., XII Int. Min. Proc. Congr. Sao Paulo, Brazil., 1977.

7. Private Communication, B.R. Arvidson, Sala Magnetics, Cambridge, Mass , 1978.

8. Espinosa-Gomez R., Msc Thesis, McGill University, Montreal., (1982).

9. Melville, D., Paul, F., Roath, S., IEEE Trans. Mag., Vol. MAG-11, 1975, p.1701.

10. Kolm, H., Maxwell, E., Oberteuffer, J., Kelland, D., Marston P., A.I.P. Conference Procedings, Graham, C.D. and Rhyme, J.J. (Eds.) New York, 1971, p.949.

11. de la Tour, C., Phd. Thesis, M.I.T. Cambridge, Mass., 1974.

12. Bitton, G., Mitchell, R., Water Res., 8, 1974, p.549.

13. Okudo, T., Sugano, I., Tsuji, T., IEEE Int. Conf. on Magnetics, London, 1975.

14. Takino, K., Tankaka, T., Shichiri, T., Industrial Applications of Magnetic Separation, ibid. p.137.

15. Yano, J., Eguchi, I., Industrial Applications of Magnetic Separation, ibid, p.134.

16. Clarkson, C.J., Russel, K.C., King, T.B., Iron and Steelmaking, 5, 1979, p.251.

17. Heitmann, G., Industrial Applications of Magnetic Separation, ibid, p.115.

18. Elliott, H.H., Holloway, J.H., Abbot, D.G., Industrial Applications of Magnetic Separation, ibid, p.127.

19. Mitchell, R., Bitton G., Oberteuffer, J.A. Separation and Purification Methods, 4(2), 1975, p.267-303.

20. Miura, M., Williams, T.M., Chem. Eng. Progr., April, 1978, p.66.

21. Turbeville, J.E., Env. Sci. Technol., 7(5), 1973, p.433.

22. Watson, J.H.P., Akinson, G., Potts, R , IEEE Trans. Mag., Vol. Mag-16, No. 5, 1980, p.940.

23. Rassi, D., Watson, J.H.P., Int. Conf. Nucl. Tech. Grado, Italy, Oct. 1981.

24. Todd, I.A., M. Eng. Thesis, McGill University, Montreal, 1979.

25. Kuhn, M.C., C.I.M. Bull., Feb. 1974, p.62.

26. Vitzoli, A., et al, J.O.M., Nov. 1967, p.52.

27. Veltman, H., O'Kane, P., AIME Annual Meeting, New York, Feb. 1968.

28. Prater, J.D. AIME Annual Meeting, San Francisco, Feb. 1972.

29. U.S. Patent No. 3,622,269. (1971).

30. Brooks, P.T., Potter, G.M., U.S.B.M., RI7402, 1970.

31. Thornhill, P.G., J.O.M., July, 1971, p.13.

32. Thorsen, G., Grislingas, A., AIME Annual Meeting, Las Vegas, 1980.

33. Craigen, W.J., CIM Bull., Vol. 68, No. 756, 1975, p.70.

34. Electrolytic Zinc Co., Australia, Aust. Pat. No. 401724, 1965.

35. Der Norske Zink Co., Norwegian Patent No. 108,047, 1965.

36. Société de la Vielle Montagne, Belgium Patent No. 724, 214, 1968.

37. Allen, R.W., Haigh, C.J., Hamdorf, C.J., Aust. Pat. No. 424095, 1970.

38. Tsunoda, S., Maeshira, I., Ewi, M., Sekini, K., AIME TMS Paper No. A73-65, 1973.

39. Dutrizac, J.E., Lead Zinc Tin 80, TMS-AIME World Symposium on Metallurgy and Environmental Control, Las Vegas, AIME, Warrendale Pa. , 1980.

40. Kunda, W., Veltman, H., Metal. Trans., 10B, 1979, p.439.

41. Powers, D.A., Rossman, G.R., Schugar, H.J., Gray, H.B., J. Solid State Chem., 13, 1975, p.1-13.

42. Pastrana, J.M., Hopstock, D.M., Trans Soc. of Min. Eng., AIME, 262, 1977, p.1.

43. Harding, K., Baxter, W., IEEE Trans. Mag., Vol-Mag 17, No.6, 1981.

44. Mathewson, C.H., "Zinc", Hafner, 1959.

45. Garrels, R.M., Christ, C.L., "Solutions, Minerals, Equilibria", Harper and Row, New York, 1965.

46. Posnjac, E., Merwin, H., J. Am. Chem. Soc., 44, 1922, p.1965.

47. McAndrew, R.T., Wang, S.S., Brown, W.R., C.I.M. Bull., Jan, 1975, p.101.

48. McKay, D.R., Halpern, J., Trans AIME, June, 1958, p.301.

49. Haig, C.J., Proc. Aust. Inst. Min. Met., Sept., 1967.

50. Nikolaeva, N.M., Tsvelodub, L.D., Russ. J. Inorg. Chem., 20(1), 1975, p.1677.

51. Lister, M.W., Rivingington, D.E., Can. J. Chem., 33, 1955, p.1591.

52. Bass, C.F., Mesmer, R.E., "Hydrolysis of Cations", Wiley Interscience, New York, 1976.

53. Knight, R.J., Sylva, R.N., J. Inorg. Nucl. Chem., 37, 3., 1975, p.779.

54. Steinveit, G., Advan. Extr. Met. Refin. Proc. Int. Symp., 1972, p.521.

55. Dutrizac, J.E. and Kaiman, S., Can. Mineral., 14, 1976, p.151.

56. Brown, J.B., Mineral Deposita, 6, 1971, p.245.

57. Umetsu, Y., Tojawa, K., Sasaki, K., Can. Met. Quart., 16, 1977, p.111.

58. Margulis, E., Getskin, L.S., Zapuskulova, N., Russ. J. Inorg. Chem., 22, No. 4, 1977, p.558.

59. Getskin, L.S., Margulis, E.V., Beiskeeva, L.I., Yaroslatsev, A.S., Izv. Vzssh. Uchelon. Zaved. Tsvetsn. Metall., No. 223, 1967, p.49.

60. Gordon, A.R., Pickering, R.W., Met. Trans. B., 6B, 1975, p.43.

61. Gordon, A.R. Adv. Ext. Met. IMM., 1977, p.153.

62. Walter-Levy, L., Quemeneur, E., C.R. Acad. Sci. Paris, 258, 1964, p.3028.

63. Davey, P.T., Scott, T.R., Trans. Inst. Min. Metall., 84, 1975, p. C83.

64. Davey, P.T., Scott, T.R., Hydrometallurgy, 2, 1976, p.25.

65. Langmuir, D., Am. J. Sc., 271, 1976, p.25.

66. Murphy, P.J., Posner, A.M., Quirk, J.P., J. Colloid. Interface. Sci., <u>56</u>, no. 2, 1976, p.312.

67. Dousma, J., DeBruyn, P.L., J. Colloid. Interface. Sci., <u>56</u>, no. 3, 1976, p.527.

68. Dousma, J., DeBruyn, P.L., J. Colloid. Interface. Sci., <u>64</u>, no.1, 1978, p. 154.

69. Mackay, A.L., Minerolog. Mag., <u>32</u>, 1959-61, p.547.

70. Kiyana, M., Takada, T., Bull. Chem. Soc. Jap., <u>45</u>, 1972, p.1923.

71. Sylva, R.N., Rev. Pure. Appl. Chem., <u>22</u>, 1972, p.115.

72. E.Z. Co. of Australia, Aust. Pat. No. 255,429, 1960.

73. Sherrit Gordon Mines Ltd, Aust. Pat. No. 429,078, 1970.

74. Katsura, T., Yutaka, T., Water Research, <u>13</u>, 1979, p.21.

75. Akashi, T., Sugamo, I., Kenmoku, V., Shimada, Y., Tsuji, T., Proc. Internat. Conf. Ferrites, Univ. Tokyo Press Japan, 1971, p.183.

76. Mellor, J.W., "Treatise on Inorganic and Theoretical Chemistry", Vol. XII, Longman Green and Co., 1934.

77. Kunda, W., Hitesman, R., Can. Met. Quart., <u>16</u>, 1977, p.118.

78. U.S. Patent No. 3,627,678, 1971.

79. Kelland, D.R., Maxwell, E., IEEE Trans. Mag., Mag-11, 1975.

80. Anon., Mining Journal, <u>298</u>, No. 7656, 1982, p.360.

81. Watson, J.H.P., J. Appl. Phys., <u>9</u>, 44, 1973, p.4209.

82. Luborsky, F.E., Drummond, B.J., IEEE Trans. Mag., Mag-11, 1975, p.1969.

83. Clarkson, C.J., Kelland, D.R., King, T.B., IEEE Trans. Mag., Mag-12, 1976, p.901.

84. Clarkson, C.J., Kelland, D.R., IEEE Trans. Mag., Mag-14, 1978, p.97.

85. Simons, W.H., Lawson, W.F., Treat, R.P., J. Appl. Phys., 4-8, 1977, p.3213.

86. Stekly, Z.J.J., Minervini, J.V., IEEE Trans. Mag., Mag-12, 1976, p.463.

87. Cummings, D.L., Himmelblau, D.A. Oberteuffeur, J.A., Powers, G.J., AlChe Journal, 22, no. 3, 1976, p.569.

88. Birss, R.R., Dennis, B.J., Gerber, R., IEEE Trans. Mag., Mag-15, 1979, p. 1362.

89. Hayaski, K., Uchiyama, S., IEEE Trans. Mag., Mag-16, 1980, p.827.

90. Watson, J.H.P., IEEE Trans. Mag., Mag-15, 1979, p. 1538.

91. Hollingworth, M., M. Eng. Thesis, McGill University, Montreal, 1982.

92. Friedlander F.J., Cowan, C., Jaluvia, R., IEEE Trans. Mag., Mag-11, 1977, p1600.

93. Luborsky, F.E., Drummond, B.J., IEEE Trans. Mag., Mag-12, 1976, p.463.

94. Watson, J.H.P., Filtration and Separation, May/June, 1977, p.242.

95. Watson, J.H.P., presented at "A Symposium on Deposition and Filtration of Particles from Gas and Liquids", Loughborough University, England, Sept., 1978.

96. Friedlander, F.J., Cowen, C., Jaluvia, R., IEEE Trans Mag, Mag-12, 1976, p.898.

97. Liu, Y.A., Oak, M.J., Lin, C.I., presented at "Novel Separation Techniques", Seventh Annual AIChE Meeting, Nov. 13-17, 1977.

98. Nesset, J.E., Finch, J.A., "Industrial Applications of Magnetic Separation". IEEE Publications No. 78CHI447-2Mag, N.Y., 1979.

99. Schlichting, H., "Boundary-Layer Theory", McGraw-Hill, 6th edition, New York, 1968.

100. Nesset, J.E., Todd, I.A., Hollingworth, M., Finch, J.A., IEEE Trans. Mag., Mag-16, 1980, p.833.

101. Nesset, J.E., M.Eng. Thesis, McGill University, 1980.

102. Akoto, J.Y., IEEE Trans. Mag., Mag-13, 1977, p.1986.

103. Collan, H.K., Kokkala, M., Ritvos, A., IEEE Trans. Mag., Mag-13, 1977, p.1480.

104. Collan, H.K., Jantunen, J., Kokkala, M., Ritvos, A., Industrial Applications of Magnetic Separation, ibid., p.175.

105. Collan, H.k., Kokkala, M.A., Toikka, O.E., Helsinki University Technical Report No. TKK-F-A453, 1981.

106. Uchiyama, S., Kurinoba, "Industrial Applications of Magnetic Separation, ibid., p.166.

107. Kolthoff, I.M., "Treatise on Chemical Analysis", New York, Wiley, 1978.

108. The Powder Diffraction File, Joint Committee on Powder Diffraction Standards, Pennsylvania, U.S.A., 1973.

109. MacKay, A.L., Minerolog. Mag., 32, 1959-1961, p.545.

110. MacKenzie, R.C., "The Differential Thermal Investigation of Clays", London:Minerological Society, 1957, p.299.

111. "Physics and Chemistry Handbook", R. Weast, ed., CRC Press, Boca Ratan, Florida, 1980.

112. Nesset, J.E., Finch, J.A., Trans. Inst. Min. Metall, 89, 1980.

113. Hess, H.H., Notes on operation of Frantz Isodynamic Magnetic Separator, S.G. Frantz Co.

114. MacAndrew, J.A., Proc. Aust. I.M.M., No. 181, 1957, p.59.

115. Lewis, D., Ji-Nong Jun, J., U.S. Pat. No. 4,102,780, 1978.

116. Lewis, D., presented at Symposium on the Theory and Applications of Magnetic Separation, Auburn University, Alabama, March 23-25, 1976.

117. Gottschalk, V.H., Wartman, F.S., U.S. Bureau of Mines R.I. 3268, 1935.

118. Clarkson, C.J., PhD. Thesis, M.I.T., 1977.

119. Cullity, B.D., "Introduction to Magnetic Materials", Addison-Wesley, 1972.

120. Cannon, M.R., Manning, R.E., Bell, J.D., Anal. Chem., 32, 1960, p.365.

121. Bird, R.B., Stewart, W.E., Lightfoot, E.N., "Transport Phenomena", Wiley, 1960, p.59.

122. Powers, D.A., Rossman, G.R., Schugar, H.J., Gray, H.B., J. of Solid State Chemistry, 13, 1975, p.1.

123. Von Fleck, J.H., J. of Phys. Radium, Paris, 12, 1951, p.262.

124. Hofer, L.J.E., Peebles, W.C., Dieter, W.E., J. of Amer. Chem. Soc., 68, 1946, p.1953.

125. Dutrizac, J.E., private communication, 1981.

126. Finch, J.A., Leroux, M., Int.

127. Dutrizac, J.E., Discussion, Complex Sulphides Symposium, CANMET, Ottawa, June 21-22, 1982.

128. Eriez Magnetics, Ore Treatment Conference, Oct. 5-6, 1981.

APPENDIX I. S.I. UNIT CONVERSION

General Units

1g → 1 x 10^{-3} k

1cm → 1 x 10^{-2}m

1g/L → 1 x 10^{-6} k /m^3

1cm/s → 1 x 10^{-2}m/sec

1g/cm^3 → 1 x 10 k /m^3

1μm → 1 x 10^{-6}m

1p.s.i. → 6.894 x 10^3 newtons/m^2 = Pascal (Pa)

1atmos. → 1.013 x 10^5 newtons/m^2

1centistoke → 1 x 10^{-6} m^2/sec

1 stoke → 1 x 10^{-4} m^2/sec

^{o}C → +273 K

Magnetisation Units

flux density: 1 gauss → 10^{-4} tesla

field intensity: 1 oersted → 79.6 ampere/meter

magnetisation: 1 emu/cm^3 → 10^3 ampere/meter

susceptibility: 1 emu/cm^3Oe → 12.56 (dimensionless S.I.)

permeability: μ_0(vacuum) = 1 → 4π x 10^{-7} webers/ampere meter

(1) In the S.I. system the loading number N_L (eqn. 3-9)

$$N_L = \frac{2bH_a^2\kappa A}{\rho_f U_\infty^{3/2}\nu^{\frac{1}{2}}a^{\frac{1}{2}}} \quad \text{(dimensionless)}$$

becomes

$$N_L = \frac{b\kappa\mu_0 H_a M_w}{V_0^{3/2}(\rho_f \eta a)^{\frac{1}{2}}} \quad \text{(dimensionless)}$$

where $\mu_0 H_a$ is the flux density generated in empty solenoid and μ_0 is the permeability of free space.

(2) The susceptibility estimated from the wet Frantz (eqn. 4-9)

$$\kappa = \frac{(\rho_p - \rho_\ell) \times \sin\theta \times 20.5 \times 10^{-6}}{I_{50}^2} \quad (\text{emu/cm}^3\text{Oe})$$

becomes

$$\kappa = \frac{(\rho_p - \rho_\ell)\ 25 \times 10^{-7}}{I_{50}^2} \quad \text{(dimensionless)}$$

(3) Wire magnetisation M_w (eqn. 4-13)

$$M_w = M_s \exp\left(-\frac{K}{H_a - 2\pi M_w}\right) \quad (\text{emu/cm}^3)$$

becomes

$$M_w = M_s \exp\left(-\frac{K}{H_a - \frac{1}{2}M_w}\right) \qquad (A/m)$$

APPENDIX II. PROCEDURE FOR COLLAN DATA FITTING

Taking run 29 as an example, C_{in} = 3g/L solids (≈ 1g/L Fe)

(1) Taking experimental values of C_{out} over the "straight" portion of the breakthrough curve, t is plotted against $\log_e \left(\frac{C_{in}}{C_{out}} - 1 \right)$ (from eqn. 3-21)

time. s	$\log_e \left(\frac{C_{in}}{C_{out}} - 1 \right)$
150	2.944
180	0.000
240	-1.945
360	-4.595

From the regression,

intercept = K = 6.99

Regression Coeff. = y = -2.059

Correlation Coeff. = -.952

std. error = 1.193

Thus,

$\ell_0 = \frac{L}{K} = 5.4$

$t_0 = -\frac{k}{y} = 203$secs. *

$C_s = \frac{t_0 v_0 C_{in}}{L} = 33.95$g/L Fe cm.

(2) The breakthrough curve is now data fitted overs its entire length from $C_{out} = \frac{C_{in}}{e^{-K(t/t_0-1)}+1}$ (eqn. 3-21)

	Experimental	Data Fit
t(s)	C_{out}/C_{in}	C_{out}/C_{in}
30	0.0	0.002
60	0.0	0.003
120	0.0	0.050
150	0.05	0.135
180	0.50	0.305
240	0.87	0.774
360	1.00	0.992
480	1.00	0.992

APPENDIX III. WET FRANTZ MEASUREMENTS

(1) MnO_2 in water. $\Theta = 30^o$ $I_{50} = .595$amps

I (amps)	% Mags
.550	16.3
.565	28.3
.575	26.9
.587	35.5
.602	63.6
.610	75.5
.625	98.3

(2) K Jarosite in water. $\Theta = 30^o$ $I_{50} = .483$amps

I (amps)	% Mags
.465	8.1
.475	25.2
.485	65.1
.495	83.2
.505	92.8
.515	97.2
.525	98.0

(3) Na Jarosite $\Theta = 30^o$ $I_{50} = .488$ amps

I (amps)	% Mags
.465	3.0
.475	8.1
.485	31.2
.495	75.1
.505	87.2
.515	92.0

(4) NH_4 Jarosite in water. $\Theta = 30^o$ $I_{50} = .472$ amps.

I (amps)	% Mags
.455	7.1
.465	15.8
.475	55.7
.485	80.2
.495	80.8
.505	95.0

(5) α-FeOOH in water. $\Theta = 30^o$ $I_{50} = .444$amps

I (amps)	% Mags
.425	10.1
.435	35.8
.445	50.1
.455	78.4
.465	82.0
.475	90.1

(6) β-FeOOH in water. $\Theta = 30^{o}$ I_{50} = .431 amps

I (amps)	% Mags
.405	13.1
.415	15.2
.425	35.8
.435	57.1
.445	85.9
.455	88.0
.465	95.1

(7) CEZ Jarosite in water. $\Theta = 30^{o}$ I_{50} = .480 amps

I (amps)	% Mags
.455	6.2
.465	18.8
.475	40.9
.485	65.6
.495	83.1
.505	89.1
.515	98.3

(8) CEZ Jarosite in Electrolyte. $\Theta = 30^{o}$ I_{50} = .437 amps

I (amps)	% Mags
.415	5.3
.425	15.1
.435	48.2
.445	72.3
.455	78.9
.465	93.3

8

(9) Hematite in water.

θ^0	25	30	35	40
sin Θ	.422	0.5	0.573	0.642
I_{50}(amps)	.395	.435	.475	.510

APPENDIX IV. EXPERIMENTAL FILTRATION DATA

Run (1) C_{in} = 0.23% Fe - 100% capture

Run (2) C_{in} = 0.23% Fe - 100% capture

Run (3) C_{in} = 0.23% Fe

t(s)	C_{out} (%Fe)	C_{out}/C_{in}
75	.02	.087
90	.105	.456
105	.155	.673
120	.167	.726

Run (4) C_{in} = 0.23% Fe

t(s)	C_{out} (%Fe)	C_{out}/C_{in}
210	.011	.05
225	.011	.05
240	.022	.09
270	.065	.28
300	.120	.52
330	.162	.69
360	.17	.73
420	.15	.65
480	.16	.69
600	.135	.58
660	.165	.71

Run (5) C_{in} = 0.24% Fe

t(s)	C_{out} (%Fe)	C_{out}/C_{in}
180	.01	.04
210	.02	.08
240	.057	.24
270	.11	.46
300	.14	.59
330	.14	.57

Run (6) C_{in} = 0.24% Fe

t(s)	C_{out} (%Fe)	C_{out}/C_{in}
180	.002	.008
195	.002	.008
210	.005	.02
240	.035	.145
270	.075	.312
300	.127	.529
330	.170	.700

Run (7) C_{in} = 0.24% Fe

t(s)	C_{out} (%Fe)	C_{out}/C_{in}
30	.007	.029
45	.012	.052
60	.067	.279
90	.192	.800
105	.200	.833

Run (8) C_{in} = 0.24% Fe

t(s)	C_{out}(%Fe)	C_{out}/C_{in}
120	.007	.037
135	.015	.062
150	.042	.175
165	.075	.312
180	.143	.595
210	.162	.675
240	.207	.862
270	.220	.910
300	.225	.930

Run (9) C_{in} = 0.24% Fe

t(s)	C_{out}(%Fe)	C_{out}/C_{in}
120	.005	.02
150	.027	.112
180	.047	.195
210	.112	.466
240	.142	.591
270	.175	.779 * =?
300	.187	.779

Run (10) C_{in} = 0.24 Fe

t(s)	C_{out}(%Fe)	C_{out}/C_{in}
240	.020	.083
255	.052	.216
270	.072	.300
300	.122	.510
330	.122	.510

Run (11) C_{in} = 0.29% Fe

t(s)	C_{out}(%Fe)	C_{out}/C_{in}
255	.02	.068
270	.067	.228
285	.102	.348
300	.122	.416
315	.152	.518
330	.152	.518

Run (12) C_{in} = 0.29% Fe

t(s)	C_{out}(%Fe)	C_{out}/C_{in}
165	.005	.017
180	.025	.058
195	.050	.170
210	.092	.317
240	.155	.529
270	.187	.638
300	.210	.716

Run (13) C_{in} = 0.29% Fe

t(s)	C_{out} (%Fe)	C_{out}/C_{in}
150	.032	.109
180	.080	.273
210	.125	.426
240	.167	.570
300	.200	.682
360	.230	.785
420	.237	.808
480	.260	.887
540	.260	.887
600	.260	.887
660	.250	.853
720	.275	.938

Run (14) C_{in} = 0.445% Fe

t(s)	C_{out} (%Fe)	C_{out}/C_{in}
30	.002	.005
45	.01	.022
60	.015	.033
90	.105	.236
120	.200	.444
150	.272	.611
180	.340	.764
240	.380	.853
300	.400	.890

Run (15) C_{in} = 0.445% Fe

t(s)	C_{out}(%Fe)	C_{out}/C_{in}
30	.002	.004
60	.025	.056
90	.115	.258
120	.220	.488
180	.325	.730
300	.410	.920
420	.440	.988
540	.440	.988

Run (16) C_{in} = 0.445% Fe

t(s)	C_{out}(%Fe)	C_{out}/C_{in}
45	.002	.005
60	.002	.005
75	.002	.005
90	.007	.015
120	.037	.083
150	.117	.262
180	.200	.449
240	.300	.674
300	.382	.858

Run (17) C_{in} = 0.57% Fe

t(s)	C_{out}(%Fe)	C_{out}/C_{in}
210	.002	.043
240	.035	.061
255	.07	.122
270	.137	.240
300	.137	.240
360	.300	.520
420	.395	.690
540	.445	.780
660	.482	.840
780	.482	.840

Run (18) Matrix plugging

Run (19) Matrix plugging

Run (20) C_{in} = 0.2% Fe

t(s)	C_{out}(%Fe)	C_{out}/C_{in}
180	.002	.010
210	.002	.010
240	.006	.030
270	.0125	.062
300	.0265	.132
330	.110	.550
420	.180	.900
540	.196	.980

Run (21) C_{in} = .087% Fe

t(s)	C_{out}(%Fe)	C_{out}/C_{in}
30	.020	.228
60	.042	.485
120	.047	.542
180	.065	.742
240	.075	.857
360	.077	.885
480	.082	.942
600	.087	1.000

Run (22) C_{in} = 0.29% Fe

t(s)	C_{out}(%Fe)	C_{out}/C_{in}
150	.007	.025
180	.049	.168
240	.175	.597
270	.225	.767
300	.225	.767
330	.288	.982
360	.263	.892
420	.290	1.00
480	.290	1.00
540	.290	1.00

Run (23) C_{in} = 0.55% Fe

t(s)	C_{out}(%Fe)	C_{out}/C_{in}
90	.04	.072
120	.13	.236
180	.29	.527
240	.36	.654
360	.36	.654
480	.29	.527
600	.15	.272

Run (24) C_{in} = 0.6% Fe

t(s)	C_{out}(%Fe)	C_{out}/C_{in}
120	.037	.062
135	.024	.040
150	.037	.062
180	.049	.082
240	.162	.270
300	.417	.695
360	.367	.611
420	.537	.595
480	.600	1.000

Run (25) C_{in} = 0.26% Fe

t(s)	C_{out}(%Fe)	C_{out}/C_{in}
90	.05	.192
120	.125	.480
150	.138	.530
180	.150	.576
210	.188	.723
240	.188	.723
360	.205	.788
420	.205	.788
540	.250	.960

Run (26) $C_{in} = 0.26\%$ Fe

t(s)	C_{out} (%Fe)	C_{out}/C_{in}
90	.025	.096
120	.025	.096
150	.113	.434
180	.250	.434
210	.213	.960
240	.260	.819
300	.260	1.00
360	.238	~~1.00~~
420	.250	.910
480	.230	.960

Run (27) $C_{in} = 0.2\%$ Fe

t(s)	C_{out} (%Fe)	C_{out}/C_{in}
120	.002	.012
180	.110	.550
240	.150	.750
300	.190	.950
360	.180	.90
420	.180	.90
480		

Run (28) C_{in} = 0.1% Fe

t(s)	C_{out}(%Fe)	C_{out}/C_{in}
120	.025	.25
180	.050	.50
240	.050	.50
360	.062	.62
420	.099	.99
480	.01	1.00
600	.01	1.00

Run (29) C_{in} = 0.1% Fe

t(s)	C_{out}(%Fe)	C_{out}/C_{in}
30	0.0	-
60	0.0	-
120	0.0	-
150	0.005	.05
180	0.050	.50
240	0.087	.87
360	0.100	1.00
480	0.100	1.00

Run (30) C_{in} = 0.24% Fe

t(s)	C_{out}	C_{in}/C_{out}
30	.0625	0.260
45	.0950	0.390
60	.1125	.468
90	.1375	.572
120	.1450	.604
135	.0125	.052
150	.0025	.010
165	.0075	.031
180	.0075	.031
210	.0075	.031
240	.0275	.114
270	.1150	.479
300	.1375	.572
330	.1400	.583
360	.1750	.729
420	.1750	.729
480	.1600	.666
540	.1900	.790
600	.2175	.906

Run (31) 100% capture

Run (32) 100% capture

APPENDIX V. FILTRATION REGRESSION ANALYSIS

Run	Corr. Coeff.	Std. Error Est.	K value	ℓ_0 value
3	-0.93	.667	7.32 ± 1.4	.737 ± .14
4	-0.97	.420	9.59 ± .47	.563 ± .02
5	-0.98	.242	8.47 ± .56	.617 ± .04
6	-0.97	.461	11.29 ± .65	.478 ± .03
7	-0.97	.615	5.88 ± 1.32	.917 ± .20
8,9	-0.89	.869	6.16 ± .53	.876 ± .08
10	-0.98	.222	12.38 ± .47	.436 ± .016
11	-0.94	.390	12.82 ± .55	.420 ± .018
12,13	-0.86	.820	5.58 ± .50	.967 ± .08
14,15	-0.95	.688	5.68 ± .44	.951 ± .07
16	-0.97	.404	3.47 ± .57	1.18 ± .15
17	-0.96	.390	6.56 ± .44	.82 ± .05
20	-0.98	.345	12.18 ± .74	.44 ± .026
21	-0.96	.325	1.27 ± .46	4.23 ± 1.5
22	-0.95	.770	7.67 ± 1.6	.70 ± .15
23	-0.95	.516	3.96 ± 1.1	1.36 ± .37
24	-0.95	.615	5.27 ± .87	1.02 ± .16
25	-0.93	.37	2.61 ± .52	2.06 ± .41
26	-0.87	1.16	5.58 ± 1.3	.96 ± .22
27	-0.94	1.20	8.02 ± 2.0	.672 ± .20
28	-0.78	—	—	—
29	-0.95	1.19	6.99 ± 2.5	.772 ± .28
30	-0.92	0.78	5.71 ± .11	0.944 ± .02